Depth-resolved assessment of tissue oxygen saturation using time-domain near infrared spectroscopy

Aleh Sudakou

Supervisor: Prof. dr hab. inż. Adam Liebert

Doctoral thesis

Warsaw, February 2024

Abstract in Polish

Rozwój metod obrazowania ludzkiego ciała ma duże znaczenie w badaniach medycznych i naukowych, oferując wgląd w strukturę i funkcję tkanek i prowadząc do wielu odkryć i zastosowań praktycznych. Niniejsza praca skupia się na użyciu światła do obrazowania tkanek. W szczególności na spektroskopii w bliskiej podczerwieni (NIRS), która jest ugruntowaną techniką monitorowania in vivo hemodynamiki tkanek, tj. lokalnych stężeń hemoglobiny utlenowanej i zredukowanej, a co za tym idzie, nasycenia tkanek tlenem (StO$_2$). Informację o utlenowaniu tkanek, równowadze pomiędzy tlenem dostarczanym a zużywanym, można zastosować do diagnozowania patologii mózgu lub monitorowania aktywności mózgowej.

W technice NIRS identyfikuje się dwa wyzwania, które utrudniają jej wprowadzenie do powszechnego użytku klinicznego. Niniejsza praca skupia się na ocenie utlenowania (StO2) kory mózgowej, ale opracowane koncepcje mogą być stosowane w innych obszarach, takich jak badania mięśni czy nerek. Pierwszym wyzwaniem jest rozdzielenie informacji z sygnałów optycznych pochodzących z różnych warstw głowy, dla bardziej dokładnej i niezawodnej oceny utlenowania mózgu. Światło mierzone na powierzchni głowy niesie informacje o tkankach mózgu oraz pozamózgowych (skóra i czaszka). Problem ten jest istotny, ponieważ mierzone światło jest zazwyczaj bardziej wrażliwe na hemodynamikę tkanek pozamózgowych, co może znacznie zakłócać wyznaczaną aktywność mózgu. Drugim wyzwaniem jest brak metod oceny wydajności oksymetrii NIRS. Brakuje wzorcowego pomiaru odniesienia dla rzeczywistych wartości parametrów ustalanych in vivo, takich jak StO2. Ważność tego wyzwania podkreślają trwające międzynarodowe starania w kierunku standaryzacji i testów wydajności systemów NIRS.

W ramach tej pracy doktorskiej wykorzystałem zaawansowany kod Monte Carlo (MC), który został opracowany w IBIB PAN do modelowania propagacji światła w tkankach. Do pomiarów na fantomach i zdrowych ochotnikach użyłem unikatowego w skali światowej systemu zbudowanego w IBIB PAN do czasowo-rozdzielczych, spektralnych pomiarów NIRS, które stanowią najbardziej zaawansowaną odmianę tej techniki.

Łącząc symulacje MC i metodę propagacji błędu, oceniłem niepewności ustalanych zmian stężeń hemoglobiny, co pozwoliło na wybór odpowiednich długości fali świetlnej w systemach NIRS [Publikacja I]. We współpracy z Physikalisch-Technische Bundesanstalt (PTB) opracowałem metodę ilościowego porównywania i klasyfikacji wydajności różnych mierzonych wielkości, co można również zastosować w analizie sygnałów NIRS z dyskryminacją głębokości [Publikacja II]. Następnie, we współpracy z University College London (UCL), University Hospital Zurich (UHZ) i Politecnico di Milano (Polimi), przetestowałem możliwości i dokładnie zweryfikowałem system zbudowany w IBIB PAN do pomiarów utlenowania

tkanek. Obejmowało to również porównanie z komercyjnym systemem NIRS i analizatorem stężenia gazów we krwi [Publikacja III].

Aby zbadać postawione hipotezy i osiągnąć główne cele badawcze, tj. zniwelować wpływ zidentyfikowanych dwóch wyzwań stawianych przed techniką NIRS, zaproponowałem metody analizy danych zapewniające wysoką dokładność i niezawodność w ustalaniu zmian absorpcji w wielu warstwach tkanek i tym samym utlenowania (StO2) w tych warstwach. Metoda wykorzystuje zmierzone zmiany momentów statystycznych rozkładów czasu przelotu fotonów (DTOFs) oraz algorytm Levenberga-Marquardta (LMA) do ustalenia zmian właściwościach optycznych w wielu warstwach. Opracowałem dwuwarstwowy fantom z krwi i tłuszczu, umożliwiający symulację kontrolowanych zmian utlenowania (StO2), niezależnie w dwóch warstwach, imitując pomiar w mózgu i warstwach zewnątrzmózgowych. Po raz pierwszy fantom ten umożliwił eksperymentalną weryfikację wyznaczania wartości StO2 w medium o dwóch warstwach [Publikacja IV].

Podsumowując, osiągnąłem główny cel prowadzonych badań proponując nową metodę wyznaczania utlenowania tkanek (StO$_2$) z dyskryminacją głębokości oraz testując ją na najbardziej zaawansowanym systemie NIRS. Zmierzyłem dane na fantomach oraz zdrowych ochotnikach, opracowałem metody analizy danych w postaci skryptów MATLABA i zamieściłem je w publicznej domenie dla wolnego dostępu w przyszłych badaniach, umożliwiając innym kontynuowanie postępów w wielowarstwowych pomiarach utlenowania głowy. Rozprawa ta czyni postępy w technice NIRS poprzez dostarczenie rozwiązań w obszarze jej kluczowych wyzwań, przybliżając ją do zastosowań klinicznych. Ocena utlenowania tkanek (StO$_2$) z dyskryminacją głębokości jest opracowana by dostarczać informację z warstwy mózgowej, i tylko tej warstwy.

Abstract

The development of methods for imaging the human body has profound implications for medical and scientific research, offering insights into biological tissues and leading to countless discoveries and applications. This thesis focuses on the use of light, in particular the Near-Infrared Spectroscopy (NIRS), which is an established technique for *in vivo* monitoring of hemodynamics, i.e. local concentrations of oxy- and deoxyhemoglobin and hence tissue oxygen saturation (StO_2). This information reports on the balance between the oxygen supply and consumption, which can be applied for the diagnosis of brain pathologies or monitoring brain activity.

The NIRS technique has two intrinsic challenges, which hinder its advancement to regular clinical use. This thesis focuses on the assessment of the brain cortex StO_2, but the developed concepts can be applied for other applications of NIRS such as for studying muscles or kidney. The light measured on the surface of the head carries information about the cerebral (brain) and the extracerebral (scalp and skull) tissues and the first challenge is to disentangle the signals of the different layers for a more accurate and reliable assessment of the brain. It is a major problem, as the measured light is typically more sensitive to the extracerebral tissue hemodynamics, which can mask the actual brain activity. The second challenge is the lack of performance assessment methods for NIRS oximetry, since there is no adequate reference measure for the true values of the *in vivo* determined parameters, such as StO_2. The importance of this challenge is highlighted by an ongoing international effort towards standardization of system performance tests in the field of NIRS.

For this thesis, I used the advanced Monte Carlo (MC) code that was developed at IBIB PAN for modelling the propagation of light through tissues. For measurements on phantoms and volunteers, I used the state-of-the-art system that was built at IBIB PAN for the multi-wavelength time-domain NIRS technique, which is the most advanced of the NIRS modalities.

Combining MC simulations and the error propagation method, I evaluated the uncertainties of the determined changes in hemoglobin's concentrations, which allowed to guide the selection of emission wavelengths for the system [Publication I]. In collaboration with Physikalisch-Technische Bundesanstalt (PTB), I developed a method for quantitatively comparing and ranking the performance of different measurands, which can be used for depth-resolved analysis [Publication II]. Then, in collaboration with University College London (UCL), University Hospital Zurich (UHZ), and Politecnico di Milano (Polimi), I tested the capabilities and thoroughly validated our system for tissue oxygenation measurements, which included a comparison against a commercial NIRS system and a blood gas analyzer [Publication III].

To address the main aims of the research, i.e. the two intrinsic challenges explained earlier, I improved the data analysis method, providing high accuracy and robustness in determining the changes in absorption

in multiple layers and hence StO_2. The method uses the measured changes in statistical moments of the distributions of times of flight of photons (DTOFs) and the Levenberg–Marquardt algorithm (LMA) for determining changes in any optical properties in multiple layers. I developed a two-layered blood-lipid phantom, allowing for the simulation of controlled dynamic changes in StO_2 independently in two layers, mimicking the scalp and brain. For the first time, this phantom allowed experimental validation of the determination of StO_2 in multiple layers. [Publication IV].

In conclusion, I achieved the main aim and presented a new methodology for depth-resolved assessment of StO_2, which I tested with the state-of-the-art system. I made the measured data and MATLAB scripts publicly available for further research, allowing others to readily use and advance the developed data analysis concepts. This thesis advances the NIRS technique by providing solutions to its intrinsic challenges, bringing it closer to regular clinical use. Depth-resolved assessment of StO_2 is expected to provide vital insights into the state of the brain.

Acknowledgements

I would like to express my deep gratitude to my supervisor, Prof. dr hab. inż. Adam Liebert, for his inspirational guidance, invaluable critical feedback, and consistent support throughout the years of my doctoral journey.

I am grateful to Dr. Heidrun Wabnitz for her insightful suggestions and for demonstrating the highest standards in research and experimental methodology through her exemplary approach during our collaborations.

My research was made possible by the experts at IBIB PAN who developed the cutting-edge tools that form the basis of this thesis. I am grateful to Dr inż. Stanislaw Wojtkiewicz for sharing and continuing to explain his most advanced and newest codes for simulating light propagation. I am equally grateful to Dr. Anna Gerega for supervising my use of her unique NIRS system and for her guidance in conducting various NIRS measurements.

My sincere appreciation extends to the colleagues mentioned above and other great scientists in our department for their collaboration, enlightening discussions, and valuable advice — Prof. dr hab. inż. Roman Maniewski, Dr hab. inż. Piotr Sawosz, and Dr inż. Michal Kacprzak, and my fellow PhD comrades, Dr. Saeed Samaei and Karolina Bejm, who shared the entire journey toward earning a PhD in our department.

Special thanks to Marcin Wozniak and his colleagues in the HR and financial departments at IBIB PAN for their important, effective management of all administrative matters within and outside the institute.

I am thankful to Prof. Ilias Tachtsidis for introducing me to the field of NIRS and for our enduring collaboration. Together with Dr. Gemma Bale, they supportively supervised my Master's thesis, giving me a positive outlook on a scientific career and leading me to participate in the BitMap project.

I would like to acknowledge the BitMap consortium for providing the opportunity to meet and collaborate with a diverse group of researchers, including pioneers and leading scientists in the NIRS community, senior researchers within the industry, and other PhD students involved in the project.

Lastly, but most importantly, I want to thank my parents for their love and support, aiding me in all aspects of my life. My achievements are a result of their dedicated efforts. I am also grateful to my family and friends, whose presence in my life makes each moment more meaningful.

Table of Contents

     I   Depth-resolved assessment of changes in concentration of chromophores using time-resolved near-infrared spectroscopy: estimation of cytochrome-c-oxidase uncertainty by Monte Carlo simulations

     II   Performance of measurands in time-domain optical brain imaging: depth selectivity versus contrast-to-noise ratio

     III   Time-domain NIRS system based on supercontinuum light source and multi-wavelength detection: validation for tissue oxygenation studies

     IV   Two-layered blood-lipid phantom and method to determine absorption and oxygenation employing changes in moments of DTOFs

List of Publications

This dissertation is constituted by four monothematic publications, which are referenced by the Roman numerals I to IV. These publications are reprinted at the end of this dissertation with the journal's consent.

Co-authored publications and conference proceedings, published during my doctoral journey, are listed in the section Scientific Activities.

I   "Depth-resolved assessment of changes in concentration of chromophores using time-resolved near-infrared spectroscopy: estimation of cytochrome-c-oxidase uncertainty by Monte Carlo simulations"
        Aleh Sudakou, Stanislaw Wojtkiewicz, Frédéric Lange, Anna Gerega, Piotr Sawosz, Ilias Tachtsidis, and Adam Liebert
        Biomedical Optics Express, 10, 4621-4635 (2019)

II   "Performance of measurands in time-domain optical brain imaging: depth selectivity versus contrast-to-noise ratio"
        Aleh Sudakou, Lin Yang, Heidrun Wabnitz, Stanislaw Wojtkiewicz, and Adam Liebert
        Biomedical Optics Express, 11, 4348-4365 (2020)

III   "Time-domain NIRS system based on supercontinuum light source and multi-wavelength detection: validation for tissue oxygenation studies"
        Aleh Sudakou, Frédéric Lange, Helene Isler, Pranav Lanka, Stanislaw Wojtkiewicz, Piotr Sawosz, Daniel Ostojic, Martin Wolf, Antonio Pifferi, Ilias Tachtsidis, Adam Liebert, and Anna Gerega
        Biomedical Optics Express 12, 6629-6650 (2021)

IV   "Two-layered blood-lipid phantom and method to determine absorption and oxygenation employing changes in moments of DTOFs"
        Aleh Sudakou, Heidrun Wabnitz, André Liemert, Martin Wolf, and Adam Liebert
        Biomedical Optics Express 14, 3506-3531 (2023)

For information on the impact of the publications, please see:
        https://scholar.google.com/citations?user=W8Qc-1wAAAAJ
        https://www.researchgate.net/profile/Aleh-Sudakou

Data and MATLAB codes used in publication IV were made available:
        https://github.com/ASudakou

1. Introduction

Imaging the body has long been a pursuit of paramount importance in medical and scientific research. The applications range from advancing our understanding of the inner workings of the human body, such as the workings of the brain, to practical applications of helping clinicians to enhance patient care. In the last decades, diverse imaging techniques have been developed, each offering a unique window into biological tissues. The main techniques rely on utilizing magnetic fields (Magnetic Resonance Imaging (MRI), functional MRI (fMRI), and Magnetic Resonance Spectroscopy (MRS)), X-ray technology (Computed Tomography (CT)), radioactive tracers (Positron Emission Tomography (PET)), sound waves (UltraSonoGraphy (USG)), electrical activity (ElectroEncephaloGram (EEG)), and light. Each technique has allowed countless discoveries in tissue studies and other areas. This thesis is devoted to the use of light for determining the oxygen saturation of tissues. Thanks to unique features of light that govern the light-tissue interactions and as a result of rapid advancements in instrumentation (lasers and detectors), many techniques that use light for imaging tissues are rapidly developing, including optical coherence tomography (OCT), photoacoustic imaging, confocal microscopy, Diffuse Correlation Spectroscopy (DCS), and Near-InfraRed Spectroscopy (NIRS). NIRS and DCS are both rapidly developing methods that use light in NIR range. DCS utilizes a coherent light source and measures the loss of coherence as light propagates through tissues, a phenomenon directly proportional to the movement of scatterers, mainly the red blood cells. This process offers a quantifiable measure of blood flow, which can be used for monitoring and imaging tissue perfusion. NIRS studies the loss of intensity of light instead of the loss of coherence of light. NIRS provides valuable information that is complementary to other imaging techniques, as demonstrated by a multimodal study that combined broadband NIRS, DCS, PET, and MRS for a full description of the hemodynamic, oxygenation, and metabolism status of the brain [1].

In 1977, Franz Jobsis described an optical window into living tissues in the near-infrared (NIR) spectrum. Light in this wavelength region can travel relatively deep (several centimeters) into tissues, providing a method for imaging the body. In particular, in the region between 650 and 1000 nm, the absorption of water is around its minimum and one of the strongest absorbers is hemoglobin. The absorption spectrum of hemoglobin is different for the oxygenated (HbO_2) and deoxygenated (Hb) forms [2], with an isosbestic point at around 805 nm. Measurements at the isosbestic point are independent of oxygen saturation, while measurements at other two or more wavelengths allow to determine the concentrations of HbO_2 and Hb and hence the oxygen saturation of blood. Measurements at more wavelengths allow for the determination of additional concentrations of other chromophores, such as lipids, collagen, or water [3]. NIRS has emerged as a powerful tool, offering a real-time, non-invasive and safe method to monitor brain

activity and tissue oxygenation at the patient's bedside. NIRS uses non-ionizing light, which does not pose a risk even for repeated long measurements in pediatric and neonatal applications. The maximum light intensity must comply with the ANSI standards limits for safe skin exposure (ANSI Z136.1) to be categorized as a nonsignificant risk device. NIRS has been validated against other techniques, in particular fMRI, which also provides a measure of the increase in regional blood flow and blood volume associated with the increase in regional neuronal activity [4]. A thorough comparison of fNIRS and fMRI is provided in a review [5]. Functional NIRS (fNIRS) measures hemodynamic changes related to neuronal activity due to functional activation, whereas NIRS focuses on measuring absolute values and does not emphasize the detection of minor fluctuations.

Oxygenation in brain tissues is a critical parameter, as it is closely linked to brain function and can provide vital insights into conditions like stroke, traumatic brain injury, and neurodegenerative diseases [6, 7]. NIRS has become an established clinical tool, following many recent clinical trials with positive results that demonstrated the usefulness of NIRS for a wide range of clinical applications [8-10]. However, it has not yet advanced to a regular clinical use, in part due to two intrinsic challenges, which are discussed below.

Modelling and simulating the propagation of light through tissues, such as the brain, is an essential tool in the field of biomedical optics. The applications range from understanding the measured signals and studying their dependence on tissue physiological parameters, to testing data analysis methods, to analyzing measured data, to designing and optimizing systems for diagnosis and treatment. The main approaches include the numerical solutions of the radiative transport equation, which are limited to simple geometries and rely on approximations [11], the finite element method (e.g. NIRFAST [12]), which extends the numeral solutions to arbitrary geometries, and the Monte Carlo (MC) method [13, 14], which is considered the gold-standard approach for simulating light propagation due to its accuracy and flexibility. I performed simulations of light propagation for all publications I to IV using the recently developed massive-parallel, multi-purpose MC program, which was recently developed by Stanislaw Wojtkiewicz and Adam Liebert [13]. The previous version of the MC code was presented by Adam Liebert et al. [14]. The new program makes use of multiple graphical processing units (GPUs) utilizing Nvidia CUDA technology. Parallel computing on even a single low-cost GPU was proven to increase the computational time by a factor of 1000 compared to simulations on a single standard central processing unit (CPU) [15]. In addition to simulation of light propagation, the program allows simulation of fluorescence light propagation and simulation of fluorescence lifetime wide field imaging. Any information about each detected photon can be accumulated inside each voxel that the photon passed, providing high-resolution 3D spatial distributions of photon (or fluorescence) interaction (or generation) probabilities. The code uses new equations that were derived for computing 3D distributions of sensitivity factors for the first three statistical moments of the distribution of times of flight of photons (DTOFs); the sensitivity factors were originally defined in [16].

Complicated geometries, e.g. MRI-based head models with multiple tissue types, and all information about light sources and detectors can be defined. An open database of human head models for MC simulations was recently published [17], which should be suitable any MC code that uses a voxelized model after a simple change of format.

This thesis utilizes the most advanced of the NIRS monitoring modalities, the multi-wavelength time-domain NIRS [18], which measures the arrival time of single photons and their wavelength, providing the most information about the propagation of light through tissue. Short pulses of light are emitted into a tissue (typically tens of million times per second) and if a photon reaches a detector, its arrival time gets recorded together with the wavelength information (typically a fraction of millions of photons per second per wavelength get detected). The distribution of times of flight of photons (DTOFs), i.e. the histogram of the recorded arrival times, contains information about the absorption and scattering of the medium. Such systems and their capabilities were reviewed in [18, 19]. For this thesis, I used the multi-wavelength time-domain NIRS system that was developed by Anna Gerega at IBIB PAN [20]. The system allows the detection of light in a 200 nm wavelength range, which can be selected. I introduced the method based on the error propagation analysis, which allows for minimizing the uncertainty of recovery of tissue hemoglobin concentrations [**Publication I**]. This method allowed to find the wavelength range for the system that corresponds to the smallest uncertainty in the determined changes in concentrations of oxyhemoglobin and deoxyhemoglobin, as well as cytochrome-c-oxidase (CCO) enzyme. Measurements of CCO have a potential to yield crucial information about cerebral metabolism, as explained in a clinical review [21].

As NIRS is a relatively new technique, it has some fundamental challenges that have not been fully resolved and this thesis addresses two of them. Most NIRS measurements are performed in reflectance geometry, where the laser and the detector are placed on the same surface a few (usually 3) centimeters apart. Since it is a non-invasive technique, the optical signals measured on the surface of the tissue are always highly contaminated by signals from the superficial layers, as light must pass through the superficial layer on its way to the deep tissue and then again on its way to the detector. Therefore, the analysis of NIRS measurements carried out on a layered tissue structure, such as the head, requires a multi-layered model as the homogeneous model is inadequate [22]. Various methods of data analysis have been developed for determining the absorption coefficient of tissue (μ_a) or its changes ($\Delta\mu_a$) at multiple depths using time-domain NIRS. These methods rely on different measurands [23, 24], which are parameters of the measured signal and which have different sensitivity depth profiles allowing for depth-resolved data analysis methods. I developed a method for quantitatively comparing and ranking the performance of different measurands in terms of their depth selectivity (a ratio of the sensitivity to deeper and superficial tissues) and noise, which is often a limiting factor in NIRS measurements [**Publication II**]. Monitoring changes in tissue

hemodynamics can be done by monitoring the changes in these measurands. However, it is much more informative to provide absolute values of the concentrations of hemoglobins (units micro Molar) or the tissue oxygen saturation (StO_2), defined as the ratio of oxyhemoglobin and total hemoglobin (units percentage). In this approach, the values of the measurands can be used to calculate the absolute μ_a using a model describing the propagation of light in the medium. Then, these μ_a values can be used to calculate the absolute concentrations of chromophores (e.g. oxy- and deoxyhemoglobin, and possibly also CCO) using the previously measured absorption spectra of the chromophores as presented above. I improved the method of data analysis, providing a more accurate and robust method of determining μ_a and hence StO_2 in multiple layers using time-domain NIRS [**Publication IV**].

The second challenge faced by the NIRS technique is associated with standardizing performance tests for NIRS systems and data analysis methods. For *in vivo* measurements of StO_2, there is a lack of established methodology for providing a reference of the true values of this parameter. Therefore, there is an international ongoing effort towards standardization of system performance tests in the field of NIRS [25, 26]. Using the established tests for assessing the performance of time-domain NIRS instruments, I thoroughly characterized and validated our system for tissue oxygenation studies [**Publication III**]. Then, I developed a new, more advanced phantom that has two layers filled with light scattering medium and whole human blood, allowing for measurements of StO_2 in multiple layers [**Publication IV**]. The phantom is a tool that allows quantitatively studying the contamination from the superficial layer when determining StO_2 in a two-layered medium. Similarly, measurements on a head are affected by the StO_2 in two layers, the scalp and the brain. The new method and the new phantom provide a methodology for depth-resolved assessment of StO_2 in multiple layers using time-domain NIRS, which was demonstrated in **Publication IV**.

The following chapters describe the carried-out work and the main results. For full details, please refer to Publications I to IV, reprinted at the end of this dissertation.

2. Research Aim and Objectives

The main aim of the carried-out research was to establish a methodology for determining StO_2 in multiple layers using time-domain NIRS.

The objectives were the following and the results were presented in Publications I to IV.

1. *Wavelength selection.* Develop a method involving the error propagation analysis for the purpose of minimizing the uncertainty of recovery of tissue chromophores concentrations changes for a time- and wavelength-resolved NIRS system (Publication I)

2. *Performance metrics.* Develop and implement a method that allows analysis, quantitative comparison, and performance ranking of different measurands for time domain NIRS that can be used for determining absorption changes at different depths in the medium (Publication II)

3. *System characterization.* Describe, characterize, and quantitatively test a multi-wavelength TD-NIRS system, using the relevant state-of-the-art performance assessment methods (Publication III)

4. *New phantom.* Develop a two-layered blood-lipid phantom that allows simulation of dynamic changes in oxygen saturation of blood (StO_2) independently in two layers (Publication IV)

5. *New method.* Develop and validate a new method for analyzing TD-NIRS measurements, in particular for determining StO_2 in two layers. Make use of the new phantom to demonstrate and assess the system's and the method's capabilities of determining StO_2 in two layers (Publication IV)

3. Wavelength Selection (Objective 1)

In my experimental investigations I used the multi-wavelength time-domain NIRS system that utilizes a supercontinuum light source and the emission spectral range is selected using a longpass filter and a shortpass filter [20, 27]. Therefore, there is flexibility in the choice of the spectral range of the light emitted into the tissue. The studies on the optimization of the number and range of wavelengths for different models and for different number of chromophores are summarized in a review [28]. I introduced the method of applying the error propagation analysis to calculate uncertainty of recovery of oxy- and deoxyhemoglobin concentration changes for different choices of wavelengths [**Publication I**]. An advantageous property of the statistical moments of DTOFs is that their uncertainties due to photon noise, which is assumed to follow Poisson statistics, can be calculated from the higher-order moments [29]. This allowed to find the wavelength range for our measurement system that corresponds to the smallest uncertainty in the determined changes in concentrations of oxyhemoglobin and deoxyhemoglobin, as well as cytochrome-c-oxidase (CCO) enzyme, taking into account the detector's spectral responsivity.

Using the Monte Carlo method, I simulated time-domain NIRS signals, i.e. DTOFs, for 25 different wavelengths (from 650 to 950 nm in steps of 12.5 nm) for a three-layered model mimicking the scalp, skull, and brain tissues. The spectral optical properties and the thickness of each layer were determined using information from various literature sources for each tissue, as detailed in Publication I. For *in vivo* measurements, e.g. on the head, the true values of optical properties of different layers and their thicknesses are unknown, as they vary from person to person. Therefore, MC simulations are essential for studying the influence of different parameters, such as the choice of wavelengths (in consequence the optical properties of the medium) or the source-detector distance, on the signals measured in diffuse reflectance geometry. I used the MC simulations to simulate DTOFs and the sensitivity factors for 25 wavelengths. I carried out an error propagation analysis to propagate the uncertainties in the statistical moments of the simulated DTOFs to the uncertainties of the determined changes in two chromophores (oxy- and deoxyhemoglobin) or three (adding cytochrome-c-oxidase). I used the equations presented by Liebert et al. [29], which allow calculating the uncertainty of changes in μ_a in two layers ($\sigma\Delta\mu_a$), and extended them to calculating the uncertainties of changes in chromophores' concentrations ($\sigma\Delta C$). The uncertainties are related to the noise associated with the stochastic nature of photons detection, which can be modelled by the Poisson statistics. This noise is inversely proportional to the number of detected photons.

I applied the error propagation to find the 16 consecutive wavelengths (from the 25 simulated wavelengths) that produce the lowest $\sigma\Delta C$, since the detection system of the used NIRS system allows acquisition of DTOFs for 16 spectral channels. For a realistic detector model, I used the responsivity

parameter to scale the signals for different wavelengths. It was previously shown that the system's detection efficiency deteriorates at higher wavelengths [30]. Responsivity is a ratio of the measured intensity to the input intensity [30] and it incorporates the quantum efficiency of a single-photon detector, the efficiency of recording pulses generated by a single-photon detector, the area of the detection fiber, the numerical aperture NA of the detection fiber. A theoretical calculation of spectral responsivity would result in a significant uncertainty, hence it is important to measure it for a system, which was previously done and the values were reported in [30].

The results showed the choice of wavelengths that lead to the lowest $\sigma\Delta C$ for the specific system. I demonstrated that this choice varies significantly depending on whether the responsivity is included in the calculations and depending on which chromophores' concentrations are being determined. Therefore, the choice of wavelengths should be determined based on the absorption spectra of considered chromophores and the spectral responsivity of the system.

4. Performance of Measurands in Time-Domain NIRS (Objective 2)

There are several established approaches for analyzing measured DTOFs to obtain depth-resolved changes in μ_a. Instead of using the full DTOF profile, it is arguably beneficial to start the analysis from calculating measurands, which are quantitates that characterize the DTOF profile. These include photon counts in time windows, their ratios, statistical moments, Mellin-Laplace moments, and Fourier components, which are explained in [24] and in **Publication II**. Furthermore, these measurands can be calculated in numerous ways, e.g. by using different width and position of time windows or the order of moments. A quantitative comparison of different measurands in terms of their ability to assess μ_a changes appearing deep in the medium was lacking. This topic was explored in two related studies, by Heidrun Wabnitz et al. [24] and **Publication II**, which reference each other.

Heidrun Wabnitz et al. [24] presented a theoretical study (based on perturbation simulations for small localized μ_a changes), which compared the spatial sensitivity profiles and depth selectivity for the first three statistical moments of the DTOF (i.e. the total number of photons, the mean time of flight, and the variance), photon counts in time windows, and the ratios of photon counts in different time windows. Also, the study explained the theoretical background. I extended the analysis by including noise, which is often a limiting factor in functional-NIRS measurements [**Publication II**]. The analysis included three objective metrics: relative contrast, contrast-to-noise ratio (CNR), and depth selectivity (a measure of susceptibility to extracerebral contamination). I examined the product of CNR and depth selectivity for quantitatively

ranking measurands' overall performance in the context of determining μ_a changes at greater depths. I repeated all calculations using DTOFs measured on two-layered liquid phantoms and DTOFs obtained with MC simulations for varying baseline parameters. The results for measured and simulated data were consistent. Furthermore, MC simulations allowed to analyze the effect of baseline parameters on the performance of measurands.

Publication II allows a better understanding of the advantages and drawbacks of the different measurands. The highest depth selectivity can be achieved with the ratios of photon counts in different time windows, but their CNR is low. The highest CNR can be achieved with the total number of photons (zeroth moment), but its depth selectivity is low. Therefore, if the optical properties of the superficial layer are known to be constant, it can be beneficial to use the total number of photons for data analysis, ignoring the high susceptibility to changes in the superficial layer. On the contrary, when changes occur in the superficial layer, the ratios of photon counts can better reflect the changes in the deeper layer, although these signals have low CNR. The product of CNR and depth selectivity yielded a valid overall performance measure and it can be utilized for performance characterization and comparison of NIRS measurands calculated from measured or simulated data in time-domain NIRS or other domains (continuous-wave or frequency-domain). For all considered measurands, the variance of the DTOF had the highest overall performance compared to other measurands.

5. Validation of NIRS System (Objective 3)

A multi-wavelength time-domain NIRS system records spectral and depth information, thus it is suitable for attempting to determine depth-resolved concentrations of oxy- and deoxyhemoglobin and hence depth-resolved oxygen saturation (StO_2). In **Publication III**, I thoroughly characterized the multi-wavelength time-domain NIRS system that was developed by Anna Gerega at IBIB PAN [31]. A unique feature of the system is measuring DTOFs simultaneously for a whole range of wavelengths, which are split into equally spaced 16 spectral channels. Other systems with similar capabilities (multi-wavelength and time-resolved) require switching wavelengths, as explained in a review [18]. The results of this system-validation study allow a quantitative assessment of future enhancements to the system, as well as comparisons with other systems reporting similar tests.

I evaluated the system with all of the most relevant state-of-the-art performance assessment methods. I measured for the wavelengths that were selected according to the optimization described in **Publication I** and used some of the performance assessment methods in **Publication II**. I performed tests based on the protocols BIP, nEUROPt, and MEDPHOT, which are explained in **Publication III**. Measurements on the well-characterized 32 homogeneous solid phantoms and the dynamic inhomogeneous solid phantom were

carried out as part of the BitMap campaign [32], which was a multi-laboratory effort to standardize the performance assessment of time-domain instruments for diffuse optics. In particular, the systems that use pulsed laser sources, single-photon detectors, and time-correlated single-photon counting electronics. I measured on two inhomogeneous phantoms, one liquid (low μ_a) and one solid (high μ_a), for comparison. Additionally, I performed Monte Carlo simulations to obtain 3D spatial distributions of the sensitivity factors for the same optical properties and measurement geometries as measured on the two inhomogeneous phantoms. The presented 3D distributions confirmed and visually explained the observed sensitivity depth profiles of the changes in the three statistical moments calculated from the measured DTOFs.

The ability to determine absolute concentrations of oxy- and deoxyhemoglobin (and hence StO$_2$) was assessed using a series of blood-lipid phantom measurements conducted in Zurich (Biomedical Optics Research Laboratory, Department of Neonatology, University Hospital Zurich, University of Zurich), using their established phantom [33]. I compared the results that I obtained with our system to the results obtained by a commercially available frequency-domain NIRS system (OxiplexTS) and by a blood gas analyzer (ABL90 FLEX). Lastly, I presented also results for *in vivo* measurements by conducting experiments on a forearm during arterial (250 mmHg) and venous (60 mmHg) cuff occlusions on three healthy volunteers.

The results demonstrated the system's exemplary performance. I presented a comprehensive analysis of each measurement and also included the results of performed Monte Carlo simulations that explain some of the findings. The characteristics of the system support its clinical use.

6. New Phantom (Objective 4)

In recent years, various tissue-mimicking phantoms have been developed for assessing and calibrating NIRS systems and validation of data analysis methods [25, 34, 35]. Phantom measurements are a necessary test before conducting *in vivo* studies, as phantoms allow to study the influence of the instrumental factors and uncertainties for well-defined geometries and optical properties. I designed and built a new phantom that may assist in the ongoing effort towards more realistic standardized performance tests in NIRS tissue oximetry [19, 36].

An established concept for a phantom is using whole human blood, mixed in a turbid suspension, for mimicking repeatable controlled dynamic StO$_2$ levels from 0 to 100%. I obtained experience performing such measurements in London (Biomedical Optics Research Laboratory, Department of Medical Physics and Biomedical Engineering, University College London) on their established phantom and using their multi-wavelength time-domain NIRS system [37]. Later, I performed similar measurements on the phantom in Zurich [33], measuring with our system in parallel with their system, as explained in the previous section for Objective 3 [Publication III]. To date, all presented phantoms that used this concept had a single

homogeneous liquid compartment. It is well-known that NIRS measurements on the head are greatly complicated by the influence of the superficial layer, thus the medium measured in diffuse reflectance geometry cannot be simulated with a homogeneous phantom [22]. I obtained experience measuring on the two-layered phantom with ink in Berlin (Department of Biomedical Optics, Physikalisch-Technische Bundesanstalt (PTB)). This phantom was developed previously for the nEUROPt protocol [38] and these measurements were explained previously for Objective 2 [Publication II]. This phantom is made up of two thin containers (~ 1 cm thick for the superficial layer and ~ 4 cm thick for the deep layer), which do not allow adequate stirring and heating for measurements with blood.

I built a new phantom for NIRS measurements that allows changing hemoglobin concentrations and StO_2 in two layers separately, mimicking the scalp (from ~ 0 to 4 cm thick) and brain (15 cm thick) [**Publication IV**]. The phantom is composed of three containers: the deep compartment, the superficial compartment, and a movable container for changing the thickness of the superficial layer. To our knowledge, no previously presented phantom has two blood-based optically turbid compartments, which can be used for mimicking extra- and intracerebral compartments of the head, where the StO_2 in each compartment can be changed independently. As a reference measure for the results obtained in a two-layered geometry, the StO_2 of the blood contained in each layer can be obtained by measuring in a homogeneous medium geometry on each layer separately. These reference measurements utilize a similar system and NIRS technique. It was reported that different NIRS tissue oximeters can produce different StO_2 values [33]. Consequently, it remains a challenge to find an independent accurate reference measurement of StO_2.

In the current version of the phantom, all windows (the ones on the surface and the one separating the two compartments) were covered with a Mylar foil (0.050 mm thick), which was shown to have a negligible effect on time-domain NIRS measurements in a reflectance geometry [39]. The scattering and absorption can be precisely controlled using Intralipid or SMOFlipid and India ink [40]. Instead of ink as an absorber, blood from a transfusion bag can be added and then controllably deoxygenated using yeast and oxygenated by bubbling oxygen from a tank. The full description of the phantom is presented in **Publication IV**.

The phantom was intended for assessing different NIRS systems and data analysis methods. Five NIRS systems can measure simultaneously on the phantom: one on the two-layered medium, one on the superficial layer in a homogeneous semi-infinite geometry, and three on the deep layer in a homogeneous semi-infinite geometry. The phantom might help in the standardization effort for the performance assessment of NIRS devices, as well as overcoming the contamination from the superficial layer.

7. New Method (Objective 5)

NIRS systems typically measure light on tissue surface in diffuse reflectance geometry and an inverse procedure is needed to determine the optical properties of the medium. Various algorithms have been developed for determining the changes in absorption ($\Delta\mu_a$) at multiple depths of a multi-layered medium using TD-NIRS measurements, which are explained in the recent book about the advances in modelling the light propagation in tissue [11]. One of the established approaches relies on the changes in statistical moments of DTOFs associated with $\Delta\mu_a$ at different depths. The method was explained by Adam Liebert et al. [16] and it was used in multiple studies [41-43]. One of the main limitations has been the assumption of very small $\Delta\mu_a$, such that changes in moments are linearly proportional to $\Delta\mu_a$, and the method's accuracy worsens for larger $\Delta\mu_a$. To improve the method, I removed this linearity assumption by implementing an analytical solution of the diffusion equation for an N-layered medium and the Levenberg–Marquardt algorithm (LMA), which is an established algorithm for solving nonlinear iterative least squares minimization problems. The algorithm searches for $\Delta\mu_a$ in each layer that result in the smallest error norm (χ^2), which is the difference between the measured and the theoretically calculated changes in statistical moments of DTOFs. For a guess of $\Delta\mu_a$ in each layer, the corresponding DTOFs are simulated and the changes in moments are calculated, which are compared to the changes in moments of measured DTOFs.

The light propagation in turbid media, e.g. in tissue, is accurately modelled using the radiative transport equation (RTE), which uses the conservation law under the principles of the Boltzmann transport equation for accounting gains and losses of photons in a small volume [44]. Multiple analytical solutions of RTE for simple geometries (e.g. homogeneous or layered) were presented, which rely on different approximations [11]. The most commonly used solution is the diffusion equation (DE), which relies on the diffusion approximation, which makes a simplifying assumption that the source and the scattering are isotropic [44]. This is not valid in the following extreme scenarios: for short source-detector distances, at early arrival times of photons, in the presence of void regions where the scattering is very small, or if the scattering is not much greater than absorption [45]. In such cases, Monte Carlo simulations can accurately model the propagation of light [13]. For typical tissues, μ'_s is two orders of magnitude higher than μ_a [2] and the diffusion approximation is suitable.

I implemented the analytical solution for an N-layered medium presented by André Liemert et al. [46]. It is common to first obtain the solution (analytical or numerical) of DE in the frequency domain and then apply the Fourier transform (FT) to obtain the solution in the time domain. The solution I used relies on the Laplace transform, which has important advantages over the commonly used FT, such as accuracy, efficiency (speed-up of up to several orders of magnitude), and numerical stability [47].

After assessing the phantom for stirring and stability, I used it to evaluate the new method by conducting experiments that involved changing ink concentration in two layers. I added a diluted ink in either the superficial or the deep compartment in 20 steps, changing the μ_a in one compartment at a time. The determined μ_a values, measured in a two-layered geometry, were consistent with the expected μ_a values, which I calculated based on the added concentrations of ink and SMOFlipid, which I had characterized in terms of their absorption and scattering. Furthermore, these values were also consistent with the μ_a values obtained separately for each layer in a homogeneous medium geometry.

Next, I evaluated the proposed method for determining StO_2 in two layers by conducting three experiments involving blood. I developed a protocol for mimicking controllable dynamic StO_2 changes separately in two compartments. The protocol remained consistent and I varied the thickness (*L*) of the superficial layer in each experiment. The measurements on the deep container, which do not depend on *L*, demonstrated the repeatability of the experiment. The measurements on the two-layered medium demonstrated the expected contamination from the superficial layer. The new method proved its capability in accurately determining StO_2 in both layers, providing values that were consistent with the results obtained from the measurements on the deep compartment. The phantom demonstrated robustness, ease of use, and yielded repeatable results.

One limitation of the method is the requirement to know the baseline optical parameters of the medium, which should be addressed for *in vivo* measurements. Also, all parameters apart from μ_a were assumed constant, whereas in *in vivo* measurements, scattering may vary due to hemodynamic changes.

I made publicly available all data and MATLAB scripts that were used in **Publication IV**. The data is suitable for testing new data analysis methods for tissue oximeters. The codes include the analytical solution of DE for an N-layered medium and the new LMA-based method for determining changes in optical properties. As LMA is a search-based algorithm, the implemented code can determine changes in any optical properties and in any layers since any of the optical properties can be searched for or set as known. In a similar way, I implemented the LMA-based fitting of the DTOF for determining absolute optical properties in multiple layers.

8. Conclusions and Prospects

The carried-out and published research, which constitutes this dissertation, successfully achieved the 5 objectives of this thesis and accomplished the main aim of establishing a methodology for determining StO_2 in multiple layers using time-domain NIRS. The developed concepts can also be applied for other applications that use time-domain NIRS.

1. I developed a method for choosing the emission spectra region that corresponds to the smallest uncertainty in the determined concentrations of chromophores, considering the characteristics of the NIRS system. Also, the method provides an estimate for the expected uncertainties in the determined parameters due to photon noise. (Objective 1, Publication I)

o   In the future, MC simulations could be extended to model all aspects of a real NIRS system. Such simulations would better fit the measured data, as well as allow to investigate all parameters of a system and how they affect the performance, providing guidance for the development of NIRS systems.

2. I developed a method for quantitatively comparing different measurands, providing different tests for evaluating the performance and an overall ranking. (Objective 2, Publication II)

o   These tests can assist in the development and assessment of new methods of data analysis, as well as in the standardization efforts in the NIRS community.

3. I provided a detailed description and validation of the multi-wavelength time-domain NIRS system using the state-of-the-art performance assessment methods (Objective 3, Publication III). I chose the emission spectra according to the results for Objective 1 and I used some of the concepts developed for Objective 2.

o   The detailed descriptions and the quantitative results can assist in developing and characterizing new systems, or for assessing improvements in the systems, or for a comparison with other systems.

4. I developed a new phantom that allowed for the first time to simulate dynamic changes in StO_2 in two layers independently. (Objective 4, Publication IV)

o   The built phantom might help in the international ongoing effort towards standardization of the performance assessment of NIRS devices, as well as overcoming the contamination from the superficial layer. One of the main remaining challenges is a reference measure that would provide the true values of StO_2. In this thesis, I compared the results obtained with measurements on the two-layered medium (two-layered model) with the results obtained with measurements on a single compartment (homogeneous model). However, it was shown that the recovered parameters, e.g. StO_2, can strongly depend on the NIRS system used [33].

5. The new method improved the accuracy in the determined optical properties and hence in the determined StO_2 in two layers. (Objective 5, Publication IV). For measurements on the new phantom, the method accurately determined StO_2 of two layers using measurements on top of the superficial layer, for a dynamic StO_2 from 100% to 0%, validating for the first time the depth-resolved StO_2 measurements.

o Following the phantom study, the next studies will aim to apply the method to clinical data. For *in vivo* measurements, it remains to find a way of determining the thickness of the superficial layer and the background optical properties during baseline, as guessing these parameters introduces a significant uncertainty in the determined parameters. After these new challenges are resolved, which are related to *in vivo* measurements, the developed phantom can be used for quantitative testing and validation prior to analyzing *in vivo* measurements. A recent study provided an open database of MRI-based human head models for 16 subjects and optode locations for realistic Monte Carlo photon simulations [17]. These can help advance data analysis methods to *in vivo* applications.

9. References

1. G. Bale, A. Rajaram, M. Kewin, L. Morrison, A. Bainbridge, L. Liu, U. Anazodo, M. Diop, K. St Lawrence, and I. Tachtsidis, "Multimodal Measurements of Brain Tissue Metabolism and Perfusion in a Neonatal Model of Hypoxic-Ischaemic Injury," **1269** (2021).
2. S. L. Jacques, "Optical properties of biological tissues: a review," Physics in Medicine & Biology **58**, R37 (2013).
3. S. K. V. Sekar, A. D. Mora, I. Bargigia, E. Martinenghi, C. Lindner, P. Farzam, M. Pagliazzi, T. Durduran, P. Taroni, A. Pifferi, and A. Farina, "Broadband (600–1350 nm) Time-Resolved Diffuse Optical Spectrometer for Clinical Use," IEEE Journal of Selected Topics in Quantum Electronics **22**, 406-414 (2016).
4. X. Cui, S. Bray, D. M. Bryant, G. H. Glover, and A. L. Reiss, "A quantitative comparison of NIRS and fMRI across multiple cognitive tasks," NeuroImage **54**, 2808-2821 (2011).
5. V. Scarapicchia, C. Brown, C. Mayo, and J. R. Gawryluk, "Functional Magnetic Resonance Imaging and Functional Near-Infrared Spectroscopy: Insights from Combined Recording Studies," Front Hum Neurosci **11**, 419 (2017).
6. M. S. Green, S. Sehgal, and R. Tariq, "Near-Infrared Spectroscopy: The New Must Have Tool in the Intensive Care Unit?," Seminars in cardiothoracic and vascular anesthesia **20**, 213-224 (2016).
7. D. Viderman, and Y. G. Abdildin, "Near-Infrared Spectroscopy in Neurocritical Care: A Review of Recent Updates," World Neurosurgery **151**, 23-28 (2021).
8. Z. Z. Wong, X. H. Chiong, S. H. Chaw, N. H. B. M. Hashim, M. F. B. Z. Abidin, S. N. B. Yunus, T. Subramaniam, and K. T. Ng, "The Use of Cerebral Oximetry in Surgery: A Systematic Review and Meta-analysis of Randomized Controlled Trials," Journal of Cardiothoracic and Vascular Anesthesia **36**, 2002-2011 (2022).
9. F. Lange, and I. Tachtsidis, "Clinical Brain Monitoring with Time Domain NIRS: A Review and Future Perspectives," Applied Sciences **9**, 1612 (2019).
10. K. Harvey-Jones, F. Lange, I. Tachtsidis, N. J. Robertson, and S. Mitra, "Role of Optical Neuromonitoring in Neonatal Encephalopathy—Current State and Recent Advances," Frontiers in Pediatrics **9** (2021).
11. T. B. Fabrizio Martelli, Samuele Del Bianco, André Liemert, Alwin Kienle, *Light Propagation through Biological Tissue and Other Diffusive Media: Theory, Solutions, and Validations, Second Edition* (SPIE, 2022).
12. H. Dehghani, M. E. Eames, P. K. Yalavarthy, S. C. Davis, S. Srinivasan, C. M. Carpenter, B. W. Pogue, and K. D. Paulsen, "Near infrared optical tomography using NIRFAST: Algorithm for numerical model and image reconstruction," Commun Numer Methods Eng **25**, 711-732 (2008).
13. S. Wojtkiewicz, and A. Liebert, "Parallel, multi-purpose Monte Carlo code for simulation of light propagation in segmented tissues," Biocybernetics and Biomedical Engineering (2021).
14. A. Liebert, H. Wabnitz, N. Zolek, and R. Macdonald, "Monte Carlo algorithm for efficient simulation of time-resolved fluorescence in layered turbid media," Optics express **16**, 13188-13202 (2008).
15. E. Alerstam, T. Svensson, and S. Andersson-Engels, "Parallel computing with graphics processing units for high-speed Monte Carlo simulation of photon migration," Journal of biomedical optics **13**, 060504 (2008).
16. A. Liebert, H. Wabnitz, J. Steinbrink, H. Obrig, M. Möller, R. Macdonald, A. Villringer, and H. Rinneberg, "Time-Resolved Multidistance Near-Infrared Spectroscopy of the Adult Head: Intracerebral and Extracerebral Absorption Changes from Moments of Distribution of Times of Flight of Photons," Appl. Opt. **43**, 3037-3047 (2004).
17. M. Wu, R. Horstmeyer, and S. Carp, "scatterBrains: an open database of human head models and companion optode locations for realistic Monte Carlo photon simulations," Journal of biomedical optics **28**, 100501 (2023).
18. F. Lange, L. Giannoni, and I. Tachtsidis, "The Use of Supercontinuum Laser Sources in Biomedical Diffuse Optics: Unlocking the Power of Multispectral Imaging," Applied Sciences **11**, 4616 (2021).
19. S. Konugolu Venkata Sekar, P. Lanka, A. Farina, A. Dalla Mora, S. Andersson-Engels, P. Taroni, and A. Pifferi, "Broadband Time Domain Diffuse Optical Reflectance Spectroscopy: A Review of Systems, Methods, and Applications," Applied Sciences **9**, 5465 (2019).
20. A. Gerega, D. Milej, W. Weigl, M. Botwicz, N. Zolek, M. Kacprzak, W. Wierzejski, B. Toczylowska, E. Mayzner-Zawadzka, R. Maniewski, and A. Liebert, "Multiwavelength time-resolved detection of fluorescence during the inflow of indocyanine green into the adult's brain," Journal of biomedical optics **17**, 087001 (2012).
21. G. Bale, C. Elwell, and I. Tachtsidis, "From Jöbsis to the present day: a review of clinical near-infrared spectroscopy measurements of cerebral cytochrome-c-oxidase," Journal of biomedical optics **21**, 091307 (2016).
22. I. Tachtsidis, and F. Scholkmann, "False positives and false negatives in functional near-infrared spectroscopy: issues, challenges, and the way forward," Neurophotonics **3**, 031405 (2016).
23. A. Sudakou, L. Yang, H. Wabnitz, S. Wojtkiewicz, and A. Liebert, "Performance of measurands in time-domain optical brain imaging: depth selectivity versus contrast-to-noise ratio," Biomed. Opt. Express **11**, 4348-4365 (2020).
24. H. Wabnitz, D. Contini, L. Spinelli, A. Torricelli, and A. Liebert, "Depth-selective analysis in time-domain optical brain imaging: moments vs time windows," Biomed. Opt. Express (2020).
25. L. Hacker, H. Wabnitz, A. Pifferi, T. J. Pfefer, B. W. Pogue, and S. E. Bohndiek, "Criteria for the design of tissue-mimicking phantoms for the standardization of biophotonic instrumentation."
26. M. A. Yücel, A. V. Lühmann, F. Scholkmann, J. Gervain, I. Dan, H. Ayaz, D. Boas, R. J. Cooper, J. Culver, C. E. Elwell, A. Eggebrecht, M. A. Franceschini, C. Grova, F. Homae, F. Lesage, H. Obrig, I. Tachtsidis, S. Tak, Y. Tong, A. Torricelli, H. Wabnitz, and M. Wolf, "Best practices for fNIRS publications," Neurophotonics **8**, 012101 (2021).
27. A. Sudakou, F. Lange, H. Isler, P. Lanka, S. Wojtkiewicz, P. Sawosz, D. Ostojic, M. Wolf, A. Pifferi, I. Tachtsidis, A. Liebert, and A. Gerega, "Time-domain NIRS system based on supercontinuum light source and multi-wavelength detection: validation for tissue oxygenation studies," Biomed. Opt. Express **12**, 6629-6650 (2021).
28. F. Scholkmann, S. Kleiser, A. J. Metz, R. Zimmermann, J. Mata Pavia, U. Wolf, and M. Wolf, "A review on continuous wave functional near-infrared spectroscopy and imaging instrumentation and methodology," NeuroImage **85 Pt 1**, 6-27 (2014).

29. A. Liebert, H. Wabnitz, and C. Elster, "Determination of absorption changes from moments of distributions of times of flight of photons: optimization of measurement conditions for a two-layered tissue model," Journal of biomedical optics **17**, 057005 (2012).

30. H. Wabnitz, D. Taubert, M. Mazurenka, O. Steinkellner, A. Jelzow, R. Macdonald, D. Milej, P. Sawosz, M. Kacprzak, A. Liebert, R. Cooper, J. Hebden, A. Pifferi, A. Farina, I. Bargigia, D. Contini, M. Caffini, L. Zucchelli, L. Spinelli, R. Cubeddu, and A. Torricelli, "Performance assessment of time-domain optical brain imagers, part 1: basic instrumental performance protocol," Journal of biomedical optics **19**, 086010 (2014).

31. A. Gerega, D. Milej, W. Weigl, N. Zolek, P. Sawosz, R. Maniewski, and A. Liebert, "Multi-wavelength time-resolved measurements of diffuse reflectance: phantom study with dynamic inflow of ICG," in *Biomedical Optics and 3-D Imaging*(Optical Society of America, Miami, Florida, 2012), p. JM3A.31.

32. P. Lanka, L. Yang, D. Orive-Miguel, J. Deepak, S. Tagliabue, A. Sudakou, S. Samaei, M. Forcione, Z. Kovacsova, A. Behera, T. Gladytz, D. Grosenick, L. Hervé, T. Durduran, K. Bejm, M. Morawiec, M. Kacprzak, P. Sawosz, A. Gerega, A. Liebert, A. Belli, I. Tachtsidis, F. Lange, G. Bale, L. Baratelli, S. Gioux, A. Kalyanov, M. Wolf, S. K. V. Sekar, M. Zanoletti, I. Pirovano, M. Lacerenza, L. Qiu, E. Ferocino, G. Maffeis, C. Amendola, L. Colombo, L. Frabasile, P. Levoni, M. Buttafava, M. Renna, L. D. Sieno, R. Re, A. Farina, L. Spinelli, A. D. Mora, D. Contini, P. Taroni, A. Tosi, A. Torricelli, H. Dehghani, H. Wabnitz, and A. Pifferi, "Multi-laboratory performance assessment of diffuse optics instruments: the BitMap exercise," Journal of biomedical optics **27**, 074716 (2022).

33. S. Kleiser, N. Nasseri, B. Andresen, G. Greisen, and M. Wolf, "Comparison of tissue oximeters on a liquid phantom with adjustable optical properties," Biomed. Opt. Express **7**, 2973-2992 (2016).

34. A. Sudakou, H. Wabnitz, A. Liemert, M. Wolf, and A. Liebert, "Two-layered blood-lipid phantom and method to determine absorption and oxygenation employing changes in moments of DTOFs," Biomed. Opt. Express **14**, 3506-3531 (2023).

35. P. Lanka, L. Yang, D. Orive-Miguel, J. Deepak Veesa, S. Tagliabue, A. Sudakou, S. Samaei, M. Forcione, Z. Kovacsova, A. Behera, T. Gladytz, D. Grosenick, L. Hervé, G. Lo Presti, L. Cortese, T. Durduran, K. Bejm, M. Morawiec, P. Sawosz, M. Kacprzak, A. Gerega, A. Liebert, A. Belli, I. Tachtsidis, F. Lange, G. Bale, L. Baratelli, S. Gioux, A. Kalyanov, M. Wolf, S. Konugolu Venkata Sekar, M. Zanoletti, I. Pirovano, M. Lacerenza, L. Qiu, E. Ferocino, G. Maffeis, C. Amendola, L. Colombo, M. Buttafava, M. Renna, L. Di Sieno, R. Re, A. Farina, L. Spinelli, A. Dalla Mora, D. Contini, A. Torricelli, A. Tosi, P. Taroni, H. Dehghani, H. Wabnitz, and A. Pifferi, *A multi-laboratory comparison of photon migration instruments and their performances: the BitMap exercise* (SPIE, 2021).

36. C. Hornberger, and H. Wabnitz, "Approaches for calibration and validation of near-infrared optical methods for oxygenation monitoring," Biomedical Engineering / Biomedizinische Technik **63** (2018).

37. F. Lange, L. Dunne, L. Hale, and I. Tachtsidis, "MAESTROS: A Multiwavelength Time-Domain NIRS System to Monitor Changes in Oxygenation and Oxidation State of Cytochrome-C-Oxidase," IEEE Journal of Selected Topics in Quantum Electronics **25**, 1-12 (2019).

38. H. Wabnitz, A. Jelzow, M. Mazurenka, O. Steinkellner, R. Macdonald, D. Milej, N. Zolek, M. Kacprzak, P. Sawosz, R. Maniewski, A. Liebert, S. Magazov, J. Hebden, F. Martelli, P. Di Ninni, G. Zaccanti, A. Torricelli, R. Re, L. Zucchelli, L. Spinelli, R. Cubeddu, and A. Pifferi, "Performance assessment of time-domain optical brain imagers, part 2: nEUROPt protocol," Journal of biomedical optics **19**, 086012 (2014).

39. S. D. Bianco, F. Martelli, F. Cignini, G. Zaccanti, A. Pifferi, A. Torricelli, A. Bassi, P. Taroni, and R. Cubeddu, "Liquid phantom for investigating light propagation through layered diffusive media," Optics express **12**, 2102-2111 (2004).

40. L. Spinelli, M. Botwicz, N. Zolek, M. Kacprzak, D. Milej, P. Sawosz, A. Liebert, U. Weigel, T. Durduran, F. Foschum, A. Kienle, F. Baribeau, S. Leclair, J. P. Bouchard, I. Noiseux, P. Gallant, O. Mermut, A. Farina, A. Pifferi, A. Torricelli, R. Cubeddu, H. C. Ho, M. Mazurenka, H. Wabnitz, K. Klauenberg, O. Bodnar, C. Elster, M. Benazech-Lavoue, Y. Berube-Lauziere, F. Lesage, D. Khoptyar, A. A. Subash, S. Andersson-Engels, P. Di Ninni, F. Martelli, and G. Zaccanti, "Determination of reference values for optical properties of liquid phantoms based on Intralipid and India ink," Biomed Opt Express **5**, 2037-2053 (2014).

41. A. Gerega, D. Milej, W. Weigl, M. Kacprzak, and A. Liebert, "Multiwavelength time-resolved near-infrared spectroscopy of the adult head: Assessment of intracerebral and extracerebral absorption changes," Biomed. Opt. Express **9**, 2974 (2018).

42. A. Jelzow, H. Wabnitz, I. Tachtsidis, E. Kirilina, R. Brühl, and R. Macdonald, "Separation of superficial and cerebral hemodynamics using a single distance time-domain NIRS measurement," Biomed Opt Express **5**, 1465-1482 (2014).

43. A. Jelzow, "In vivo quantification of absorption changes in the human brain by time-domain diffuse near-infrared spectroscopy. PhD Thesis," (2013).

44. M. S. Patterson, B. Chance, and B. C. Wilson, "Time resolved reflectance and transmittance for the noninvasive measurement of tissue optical properties," Appl. Opt. **28**, 2331-2336 (1989).

45. H. Dehghani, S. R. Arridge, M. Schweiger, and D. T. Delpy, "Optical tomography in the presence of void regions," Journal of the Optical Society of America A: Optics and Image Science, and Vision **17**, 1659-1670 (2000).

46. A. Liemert, and A. Kienle, "Light diffusion in N-layered turbid media: frequency and time domains," Journal of biomedical optics **15**, 025002 (2010).

47. A. Liemert, and A. Kienle, "Application of the Laplace transform in time-domain optical spectroscopy and imaging," Journal of biomedical optics **20**, 110502 (2015).

Statements of co-authorship

While Aleh Sudakou was the lead author in Publications I to IV, these works encompass a collaborative research involving a number of different scientists.

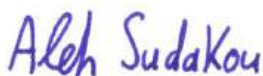# Declaration for Publication I

"Depth-resolved assessment of changes in concentration of chromophores using time-resolved near-infrared spectroscopy: estimation of cytochrome-c-oxidase uncertainty by Monte Carlo simulations"
Aleh Sudakou, Stanislaw Wojtkiewicz, Frédéric Lange, Anna Gerega, Piotr Sawosz, Ilias Tachtsidis, and Adam Liebert

Biomedical Optics Express 10, 4621-4635 (2019)

I declare that the contribution of Aleh Sudakou to the above publication was the following:

- Participated in developing and finalizing the concept of the study

- Conducted Monte Carlo simulations

- Wrote custom MATLAB scripts for data analyses and carried out data analyses

- Leading role in writing the manuscript and submitting it to a journal as a corresponding author

Aleh Sudakou

Prof. Adam Liebert

Declaration for Publication II

"Performance of measurands in time-domain optical brain imaging: depth selectivity versus contrast-to-noise ratio"

Aleh Sudakou, Lin Yang, Heidrun Wabnitz, Stanislaw Wojtkiewicz, and Adam Liebert

Biomedical Optics Express 11, 4348-4365 (2020)

I declare that the contribution of Aleh Sudakou to the above publication was the following:

- Participated in developing and finalizing the concept of the study

- Conducted phantom experiments with Lin Yang and under the supervision of Heidrun Wabnitz at PtB

- Conducted Monte Carlo simulations

- Wrote custom MATLAB scripts for data analyses and carried out data analyses

- Leading role in writing the manuscript and submitting it to a journal as a corresponding author

Aleh Sudakou

Prof. Adam Liebert

Declaration for Publication III

"Time-domain NIRS system based on supercontinuum light source and multi-wavelength detection: validation for tissue oxygenation studies"

Aleh Sudakou, Frédéric Lange, Helene Isler, Pranav Lanka, Stanislaw Wojtkiewicz, Piotr Sawosz, Daniel Ostojic, Martin Wolf, Antonio Pifferi, Ilias Tachtsidis, Adam Liebert, and Anna Gerega

Biomedical Optics Express 12, 6629-6650 (2021)

I declare that the contribution of Aleh Sudakou to the above publication was the following:

- Participated in developing and finalizing the concept of the study

- Participated in conducting phantom experiments in Zurich with Anna Gerega, Helene Isler, and Daniel Ostojic, under the supervision of Martin Wolf

- Conducted phantom experiments in London with Frédéric Lange, under the supervision of Ilias Tachtsidis

- Conducted phantom experiments in Warsaw alone, and with Pranav Lanka under the guidance from Antonio Pifferi

- Conducted Monte Carlo simulations

- Wrote custom MATLAB scripts for data analyses and carried out data analyses

- Leading role in writing the manuscript and submitting it to a journal as a corresponding author

Aleh Sudakou

Aleh Sudakou
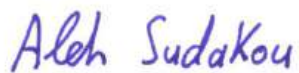
Prof. Adam Liebert

Declaration for Publication IV

"Two-layered blood-lipid phantom and method to determine absorption and oxygenation employing changes in moments of DTOFs"

Aleh Sudakou, Heidrun Wabnitz, André Liemert, Martin Wolf, and Adam Liebert

Biomedical Optics Express 14, 3506-3531 (2023)

I declare that the contribution of Aleh Sudakou to the above publication was the following:

- Participated in developing and finalizing the concept of the study

- Designed the phantom and collaborated with the workshop technician who built it (Mr. Walenty Rosak)

- Conducted phantom experiments

- Conducted Monte Carlo simulations

- Developed, implemented, and tested an improved method for data analysis

- Wrote custom MATLAB scripts for data analyses and carried out data analyses

- Leading role in writing the manuscript and submitting it to a journal as a corresponding author

Aleh Sudakou

Prof. Adam Liebert

Scientific Activities

Research projects

08 / 2016 to 08 / 2019	Marie Curie Trainee in the European Union's Horizon 2020 Marie Skłodowska-Curie Innovative Training Networks programme (ITN-ETN), under grant agreement no. 675332 "BitMap: Brain injury and trauma monitoring using advanced photonics" https://app.dimensions.ai/details/grant/grant.4274159 https://cordis.europa.eu/project/id/675332
01 / 2020 to 01 / 2023	The National Science Centre (NCN), Poland. PRELUDIUM project, under grant agreement no. UMO-2019/33/N/ST7/02918 "Depth-resolved assessment of tissue oxygen saturation for brain oxygenation studies" https://app.dimensions.ai/details/grant/grant.9334625 https://projekty.ncn.gov.pl/index.php?projekt_id=448217
2021 and 2022	Nalecz Institute of Biocybernetics and Biomedical Engineering PAS "The internal projects ST213 and ST223"

Co-authored publications

1. "Self-calibrating time-resolved near infrared spectroscopy"

   Stanislaw Wojtkiewicz, Anna Gerega, Marta Zanoletti, **Aleh Sudakou**, Davide Contini, Adam Liebert, Turgut Durduran, and Hamid Dehghani

   Biomedical Optics Express, 10, 2657-2669 (2019)

2. "Influence of contrast-reversing frequency on the amplitude and spatial distribution of visual cortex hemodynamic responses"

   Karolina Bejm, Stanislaw Wojtkiewicz, Piotr Sawosz, Maciej Perdziak, Zanna Pastuszak, **Aleh Sudakou**, Petro Guchek, and Adam Liebert

   Biomedical Optics Express, 10, 6296-6312 (2019)

3. "Space-enhanced time-domain diffuse optics for determination of tissue optical properties in two-layered structures"

   Lin Yang, Heidrun Wabnitz, Thomas Gladytz, **Aleh Sudakou**, Rainer Macdonald, and Dirk Grosenick

   Biomedical Optics Express, 11, 6570-6589 (2020)

4. "Multi-laboratory performance assessment of diffuse optics instruments: the BitMap exercise"

   Pranav Lanka, Lin Yang, David Orive-Miguel, Joshua Deepak Veesa, Susanna Tagliabue, **Aleh Sudakou**, Saeed Samaei, Mario Forcione, Zuzana Kovacsova, Anurag Behera, Thomas Gladytz, Dirk Grosenick, Lionel Hervé, Turgut Durduran, Karolina Bejm, Magdalena Morawiec, Michał Kacprzak, Piotr Sawosz, Anna Gerega, Adam Liebert, Antonio Belli, Ilias Tachtsidis, Frédéric Lange, Gemma Bale, Luca Baratelli, Sylvain Gioux, Alexander L. Kalyanov, Martin Wolf, Sanathana Konugolu-Venkata-Sekar, Marta Zanoletti, Ileana Pirovano, Michele Lacerenza, Lina Qiu, Edoardo Ferocino, Giulia Maffeis, Caterina Amendola, Lorenzo Colombo, Lorenzo Frabasile, Pietro Levoni, Mauro Buttafava, Marco Renna, Laura Di Sieno, Rebecca Re, Andrea Farina, Lorenzo Spinelli, Alberto Dalla Mora, Davide Contini, Paola Taroni, Alberto Tosi, Alessandro Torricelli, Hamid Dehghani, Heidrun Wabnitz, and Antonio Pifferi

   Journal of Biomedical Optics 27, 074716 (2022)

5. "Depth-selective method for time-domain diffuse reflectance measurements: validation study of the dual subtraction technique"

   Elham Fazliazar, **Aleh Sudakou**, Piotr Sawosz, Anna Gerega, Michal Kacprzak, and Adam Liebert

   Biomedical Optics Express 14, 6233-6249 (2023)

Conference proceedings

1. "Multi-wavelength time-resolved NIRS measurements for estimation of absolute concentration of chromophores: blood phantom study"

   Aleh Sudakou, Frederic Lange, Helene Isler, Anna Gerega, Daniel Ostojic, Piotr Sawosz, Ilias Tachtsidis, Martin Wolf, and Adam Liebert

   European Conferences on Biomedical Optics (Proc. SPIE/OSA, 2019)

2. "Depth selectivity in time-domain fNIRS by analyzing moments and time windows"

   Aleh Sudakou, Heidrun Wabnitz, Lin Yang, Davide Contini, Lorenzo Spinelli, Alessandro Torricelli, and Adam Liebert

   SPIE Photonics West BiOS (Proc. SPIE BiOS 2021)

3. "Hemoglobin spectra and employed wavelengths affect estimation of concentration and oxygen saturation: blood-lipid phantom study"

   Aleh Sudakou, Anna Gerega, Helene Isler, Piotr Sawosz, Daniel Ostojic, Martin Wolf, and Adam Liebert

   European Conferences on Biomedical Optics (Proc. SPIE/OSA, 2021)

Co-authored conference proceedings

1. "The BITMAP exercise – a multi-laboratory performance assessment campaign of diffuse optical instrumentation"

   Pranav Lanka, Lin Yang, David Orive-Miguel, Joshua Deepak Veesa, Susanna Tagliabue, **Aleh Sudakou**, Saeed Samaei, Mario Forcione, Zuzana Kovacsova, Anurag Behera, Lionel Hervé, Turgut Durduran, Adam Liebert, Piotr Sawosz, Antonio Belli, Ilias Tachtsidis, Alberto Dalla Mora, Hamid Dehghani, Heidrun Wabnitz, and Antonio Pifferi

   European Conferences on Biomedical Optics (Proc. SPIE/OSA, 2019)

2. "The BitMap dataset: an open dataset on performance assessment of diffuse optics instruments"

   David Orive-Miguel, Pranav Lanka, Lin Yang, Susanna Tagliabue, **Aleh Sudakou**, Saeed Samaei, Joshua Deepak Veesa, Mario Forcione, Zuzana Kovacsova, Anurag Behera, Lionel Hervé, Turgut Durduran, Adam Liebert, Piotr Sawosz, Antonio Belli, Ilias Tachtsidis, Alberto Dalla Mora, Jérôme Mars, Laurent Condat, Alessandro Torricelli, Hamid Dehghani, Heidrun Wabnitz, and Antonio Pifferi

   European Conferences on Biomedical Optics (Proc. SPIE/OSA, 2019)

3. "Multi-laboratory efforts for the standardization of performance assessment of diffuse optics instruments – the BitMap Exercise"

   Pranav Lanka, Lin Yang, David Orive-Miguel, Joshua Deepak Veesa, Susanna Tagliabue, **Aleh Sudakou**, Saeed Samaei, Mario Forcione, Zuzana Kovacsova, Anurag Behera, Thomas Gladytz, Dirk Grosenick, Lionel Hervé, Giuseppe LoPresti, Lorenzo Cortese, Turgut Durduran, Karolina Bejm, Magdalena Morawiec, Michał Kacprzak, Piotr Sawosz, Anna Grega, Adam Liebert, Antonio Belli, Ilias Tachtsidis, Frederic Lange, Gemma Bale, Luca Baratelli, Sylvain Gioux, Kalyanov Alexander, Martin Wolf,, Sanathana Konugolu-Venkata-Sekar, Marta Zanoletti, Ileana Pirovano, Michele Lacerenza, Lina Qiu, Edoardo Ferocino, Giulia Maffeis, Caterina Amendola, Lorenzo Colombo, Mauro Buttafava, Marco Renna, Laura Di Sieno, Rebecca Re, Andrea Farina, Lorenzo Spinelli, Alberto Dalla Mora, Davide Contini, Paola Taroni, Alberto Tosi, Alessandro Torricelli, Hamid Dehghani, Heidrun Wabnitz, and Antonio Pifferi

   Biophotonics Congress: Biomedical Optics (Proc. SPIE/OSA, 2020)

4. "A multi-laboratory comparison of photon migration instruments and their performances: the BitMap exercise"

   Pranav Lanka, Lin Yang, David Orive-Miguel, Joshua Deepak Veesa, Susanna Tagliabue, **Aleh Sudakou**, Saeed Samaei, Mario Forcione, Zuzana Kovacsova, Anurag Behera, Thomas Gladytz, Dirk Grosenick, Lionel Hervé, Giuseppe Lo Presti, Lorenzo Cortese, Turgut Durduran, Karolina Bejm, Magdalena Morawiec, Piotr Sawosz, Michal Kacprzak, Anna Gerega, Adam Liebert, Antonio Belli, Ilias Tachtsidis, Frédéric Lange, Gemma Bale, Luca Baratelli, Sylvain Gioux, Alexander Kalyanov, Martin Wolf, Sanathana Konugolu Venkata Sekar, Marta Zanoletti, Ileana Pirovano, Michele Lacerenza, Lina Qiu, Edoardo Ferocino, Giulia Maffeis, Caterina Amendola, Lorenzo Colombo, Mauro Buttafava, Marco Renna, Laura Di Sieno, Rebecca Re, Andrea Farina, Lorenzo Spinelli, Alberto Dalla Mora, Davide Contini, Alessandro Torricelli, Alberto Tosi, Paola Taroni, Hamid Dehghani, Heidrun Wabnitz, and Antonio Pifferi

   SPIE Photonics West BiOS (Proc. SPIE/OSA 2021)

Conferences

09 / 2016 Paris	fNIRS2016
03 / 2017 Berlin	Berlin BRAIN & BRAIN PET 2017: 28th International Symposium on Cerebral Blood Flow, Metabolism and Function and the 13th International Conference on Quantification of Brain Function with PET
06 / 2017 Munich	European Conferences on Biomedical Optics (ECBO2017) **Oral Presentation** "Optimization of number of wavelengths necessary for estimation of oxy, deoxy- hemoglobin, and cytochrome-c-oxidase"
09 / 2017 London	fNIRS UK2017
09 / 2017 Krakow	Polish Conference on Biocybernetic and Biomedical Engineering (20th PCBBE) **Oral Presentation** "Optimal selection of wavelengths for estimation of oxy-, deoxy-hemoglobin and cytochrome-c-oxidase from time-resolved NIRS measurements"
05 / 2018 Warsaw	154th ICB Seminar (International Centre of Biocybernetics): Statistics and clinical practice **Poster Presentation** "Technical validation of the 16-channel multiwavelength time-resolved NIRS system employing the moments method"
06 / 2018 Prague	World Congress on Medical Physics and Biomedical Engineering (IUPESM) **Poster Presentation** "Assessment of changes in CCO concentration in the brain cortex using NIRS: wavelength optimization study"
10 / 2018 Brussels	Performance Assessment and Standardization in Biophotonics
11 / 2018 Barcelona	Symposium of Neuromonitoring and Treatment of the Neurocritical Patient (PIC) **Poster Presentation** "Multi-wavelength time-resolved NIRS measurements for estimation of absolute concentration of chromophores: blood phantom study"
06 / 2019 Warsaw	164th ICB Seminar (International Centre of Biocybernetics): Quantitative diffuse optical methods for neuromonitoring
06 / 2019 Munich	European Conferences on Biomedical Optics (ECBO2019) **Poster Presentation** "Multi-wavelength time-resolved NIRS measurements for estimation of absolute concentration of chromophores: blood phantom study"
09 / 2019 Birmingham	fNIRS UK2019 **Poster Presentation** "Multi-wavelength time-resolved NIRS for estimation of changes in oxy, deoxyhaemoglobin and cytochrome-c-oxidase"
03 / 2021 Online	SPIE Photonics West BiOS **Oral Presentation** "Depth selectivity in time-domain fNIRS by analyzing moments and time windows"

06 / 2021   European Conferences on Biomedical Optics (ECBO2021)
Online   **Oral Presentation** "Hemoglobin spectra and employed wavelengths affect estimation of concentration and oxygen saturation: blood-lipid phantom study"

09 / 2021   Polish Conference on Biocybernetic and Biomedical Engineering (22nd PCBBE)
Online   **Poster Presentation** "Hemoglobin spectra affect estimation of concentration and oxygen saturation: blood-lipid phantom study"

09 / 2022   ISOTT2022
Ascona   **Oral Presentation** "Two-layered blood-lipid phantom for simulating dynamic oxygen saturation changes in both layers"

10 / 2022   fNIRS2022 (Boston, United States, attended remotely)
Online   **Virtual Poster Presentation** "Towards an optical simulator for time-domain cerebral tissue oximetry"
Poster Presentation (presented in-person by H. Wabnitz) "Phantom with two blood-lipid layers that simulate dynamic oxygen saturation changes and improvement to data analysis"

09 / 2023   Polish Conference on Biocybernetic and Biomedical Engineering (23rd PCBBE)
Lodz   **Poster Presentation** "Determination of oxygen saturation in two layers with TD-NIRS using a single DTOF versus changes in moments of DTOFs"

Trainings, workshops, and summer schools

1 week. 2017   Biophotonics'17 Summer school
Island of Ven, Sweden   **Poster Presentation** "TR multi-wavelength near-infrared measurement for estimation of depth-resolved changes in CCO"

1 week. 2018   10th European Short Course on: Time-resolved Microscopy and Correlation Spectroscopy, hosted by PicoQuant
Berlin

1 week. 2020   Biophotonics and Imaging Graduate Summer School
Online   **Poster Presentation** "Validation of 16-channel multi-wavelength time-resolved NIRS system: blood phantom study"

The BitMap project consortium meetings:
09 / 2016   Paris, France
06 / 2017   Birmingham, United Kingdom, at University of Birmingham
11 / 2017   Milan, Italy, at Politecnico di Milano
01 / 2018   Brussels, Belgium
05 / 2018   Warsaw, Poland, at IBIB PAN
09 / 2018   Barcelona, Spain, at HemoPhotonics

Secondments and internships

4 weeks. 2017	University College London (UCL)
London	Topic: Time-resolved near-infrared spectroscopy and blood-lipid phantoms
	Supervisors: Frédéric Lange and Ilias Tachtsidis

4 weeks. 2018	University of Birmingham (UoB)
Birmingham	Topic: NIRFAST technique and optical brain signals
	Supervisors: Stanislaw Wojkiewicz and Hamid Dehghani

1 week. 2018	University Hospital Zurich (UHZ)
Zurich	Topic: Blood-lipid phantoms for near-infrared spectroscopy measurements
	Supervisors: Isler Helene and Martin Wolf

	Physikalisch-Technische Bundesanstalt (PtB)
4 weeks. 2019	Topic: Time-resolved near-infrared spectroscopy measurements and data analysis
4 weeks. 2022	Topic: Towards an optical simulator for time-domain cerebral tissue oximetry
Berlin	Supervisor: Heidrun Wabnitz

Reviewing activities

Aleh Sudakou has served as an anonymous reviewer for manuscripts submitted to Biomedical Optics Express (5 reviews), Optics Express (3 reviews), Applied Optics (2 reviews), Biocybernetics and Biomedical Engineering (1 review), Journal of the Optical Society of America A (1 review), and Optics Letters (1 review).

Aleh Sudakou is a Review Editor for Physical Neuroergonomics for Frontiers in Neuroergonomics journal.

Awards

Award of the Director of IBIB PAN for Young Scientists for the best research achievements in 2019.

Award of the Director of IBIB PAN for Young Scientists for the best research achievements in 2020.

Best talk at PCBBE conference during a session.

Publications Constituting Dissertation

The journal (Optica Publishing Group Copyright department) provided consent for reprinting the four publications, noting that if the entire article is being included, it is permissible to use the version of record.

Depth-resolved assessment of changes in concentration of chromophores using time-resolved near-infrared spectroscopy: estimation of cytochrome-c-oxidase uncertainty by Monte Carlo simulations

ALEH SUDAKOU,[1,*] STANISLAW WOJTKIEWICZ,[1,3] FRÉDÉRIC LANGE,[2] ANNA GEREGA,[1] PIOTR SAWOSZ,[1] ILIAS TACHTSIDIS,[2] AND ADAM LIEBERT[1]

[1]*Nalecz Institute of Biocybernetics and Biomedical Engineering Polish Academy of Sciences, Trojdena 4, 02-109 Warsaw, Poland*
[2]*Department of Medical Physics and Biomedical Engineering, University College London, London WC1E 6BT, United Kingdom*
[3]*School of Computer Science, University of Birmingham, Edgbaston, Birmingham, B15 2TT, United Kingdom*
*asudakou@ibib.waw.pl

Abstract: Time-resolved near-infrared spectroscopy (TR-NIRS) measurements can be used to recover changes in concentrations of tissue constituents (ΔC) by applying the moments method and the Beer-Lambert law. In this work we carried out the error propagation analysis allowing to calculate the standard deviations of uncertainty in estimation of the ΔC. Here, we show the process of choosing wavelengths for the evaluation of hemodynamic (oxy-, deoxyhemoglobin) and metabolic (cytochrome-c-oxidase (CCO)) responses within the brain tissue as measured with an in-house developed TR-NIRS multi-wavelength system, which measures at 16 consecutive wavelengths separated by 12.5 nm and placed between 650 and 950 nm. Data generated with Monte Carlo simulations on three-layered model (scalp, skull, brain) for wavelengths range from 650 to 950 nm were used to carry out the error propagation analysis for varying choices of wavelengths. For a detector with a spectrally uniform responsivity, the minimal standard deviation of the estimated changes in CCO within the brain layer, $\sigma \Delta C_{CCO}^{brain} = 0.40$ μM, was observed for the 16 consecutive wavelengths from 725 to 912.5 nm. For realistic a detector model, i.e. the spectral responsivity characteristic is considered, the minimum, $\sigma \Delta C_{CCO}^{brain} = 0.47$ μM, was observed at the 16 consecutive wavelengths from 688 to 875 nm. We introduce the method of applying the error propagation analysis to data as measured with spectral TR-NIRS systems to calculate uncertainty of recovery of tissue constituents concentrations.

1. Introduction

Functional near-infrared spectroscopy (fNIRS) has showed capability to estimate changes in concentrations of chromophores contained in the brain: oxy-, deoxyhemoglobin and the oxidation state of cytochrome-c-oxidase (CCO) enzyme [1]. Fields of application of near-infrared spectroscopy (NIRS) method have been recently reviewed [1–5] and a common interest on using NIRS to monitor CCO emerges. CCO is present in all mitochondria and is involved in more than 95% of oxygen consumption [6]. Clinical NIRS measurements of cerebral cytochrome-c-oxidase can yield information about energy metabolism on cellular level [7] and have potential to be a

metabolic marker of brain injuries [8]. The estimation of CCO is challenging and requires high accuracy in measurements as the CCO has broad spectral absorption peak in NIR region and low cerebral concentration [1]. Hence, the optical signals resulting from changes in cerebral concentration of CCO are much smaller than the signals corresponding to e.g. hemoglobins.

fNIRS relies on changes in the optical properties of tissue to evaluate physiological responses. Optical signals are measured typically in reflectance geometry, where source and detector optodes are positioned on the head surface at a distance of several centimeters (typically 3-4 cm). The changes in the optical signals can originate in the brain, in the overlying scalp or in both tissues. A reliable method to separate signals originating at different depths is required to discriminate between cerebral and systemic physiological changes [9–14] and hence avoid false-positive results in functional studies [15,16]. Number of methods have been suggested and applied to address the problem of contamination by the perfusion of extracerebral tissues when trying to recover brain oxygenation, including with the use of continuous wave sources [17] or the time-resolved NIRS (TR-NIRS) technique [18]. In TR-NIRS, short pulses of light, typically on the order of picoseconds in width, are emitted into the tissue and the arrival times of remitted photons are measured using time-correlated single photon counting electronics. The histogram of the arrival times represents the distribution of time of flight of photons (DTOF). TR data analysis methods calculate the broadening of DTOFs to recover absorption and scattering properties of tissue penetrated by the light pulses. In this study, we analyze DTOFs with the moments method [19], which utilizes statistical moments of the time-resolved distributions and allows to recover changes in the absorption coefficient with depth discrimination [20–22]. The moments method has been validated using Monte Carlo simulations [19], in experiments on phantoms [23] and during functional stimulation experiments [20,21]. The method has been applied during carotid surgery [22], to communicate with patients who are in a functionally locked-in state [24], and for assessment of cerebral perfusion by monitoring the inflow and the washout of an injected optical contrast agent indocyanine green with discrimination between the extra- and intracerebral tissue compartments [25,26]. The estimated depth-resolved changes in absorption coefficient at multiple wavelengths can be converted to depth-resolved changes in concentrations of chromophores using the Beer-Lambert law [20,22]. Literature shows lack of reported uncertainties [22] or the uncertainty is calculated as the standard deviation of block-averaged measurements [20]. Here, we extend the error propagation for the moments method [27] in order to calculate the standard deviations in the estimated changes in concentrations of chromophores within multiple layers applied for TR-NIRS data analyzed using the moments method and the Beer-Lambert law. The error propagation as used in this study accounts for the noise associated with the stochastic nature of the scattered photons, which are assumed to follow the Poisson statistics.

Here we introduce the method of applying the error propagation analysis to data as measured with spectral TR-NIRS systems to minimize uncertainty of recovery of tissue constituents' concentrations. A recent review [3] summarizes the past studies that found the optimal number and range of wavelengths for different models, number of chromophores and number of wavelengths. The past studies aimed to minimize certain criteria, i.e. the condition number [28] and the residual norms [29] of the absorption extinction coefficients matrix, the levels of separability and cross-talk [30], the signal-to-noise ratio assuming a fixed amount of power [31], sensitivity and resolution [32], sensitivity overlap for different wavelengths [33], and a heuristic search for wavelengths that produce the closest result to the result of using 121 wavelengths [34]. Monte Carlo (MC) simulations are the gold standard for generating TR-NIRS data [35]. As such, we used MC simulated spectral TR-NIRS data for wavelengths from 650 to 950 nm for a three-layered model (scalp, skull and brain). Further, we calculated the standard deviation in estimation of concentration changes ($\sigma \Delta C$) of oxy-, deoxyhemoglobin and CCO in two compartments (scalp, brain) for different choices of wavelengths. The wavelength optimization criteria is to minimize $\sigma \Delta C$ of CCO in the brain layer. The multi-wavelength TR-NIRS system,

developed in the author's group and successfully tested in brain hemodynamic studies [23,25], can measure DTOFs simultaneously at 16 consecutive wavelengths separated by 12.5 nm and placed between 650 nm and 950 nm. We carried out analysis within the instrument wavelength range considering two case studies: 16 consecutive wavelengths separated by 12.5 nm and varying number of evenly spread wavelengths. We included the spectral responsivity [36] of photosensitive element in the analysis. The multialkaline cathode, as used in the TR-NIRS system investigated in this paper, has much higher sensitivity at shorter wavelengths and as such the detector performance can be the dominant factor that affects the optimal wavelengths range.

2. Methodology

2.1. Error propagation in the moments method

The analysis of TR-NIRS measurements based on changes in statistical moments of DTOFs has been presented in [19,20,37]. The DTOF is a histogram of photon counts (N_i) at time channels indexed by i. A time channel in DTOF corresponds to the time of flight of a detected photon. The multi-wavelength TR-NIRS system, as shown in [23,25], records DTOFs typically with 1024 time channels of width $t = 13.68$ picoseconds. The first three statistical moments of DTOF can be defined as: $m_0 = N_{tot} = \Sigma N_i$ (zeroth), $m_1 = <t> = \Sigma t_i N_i / m_0$ (first) and $m_2^c = V = \Sigma (t_i - m_1)^2 N_i / m_0$ (second central). These statistical moments of DTOF are known as: total number of photons (N_{tot}), mean time of flight ($<t>$) and variance (V). The sensitivity factors relate changes in statistical moments measured for a given source-detector pair to changes in absorption coefficient $\Delta \mu_a$ within sub-volumes (e.g. layers indexed by j): $\Delta A = -\ln(N_{tot}*/N_{tot}) = \Sigma[MPP(j)\Delta\mu_a(j)]$, $\Delta T = <t>* - <t> = \Sigma[MTSF(j)\Delta\mu_a(j)]$, $\Delta V = V^* - V = \Sigma[VSF(j)\Delta\mu_a(j)]$. The star (*) denotes a statistical moment after a change in absorption, *MPP* is the mean partial pathlength, *MTSF* is the mean time of flight sensitivity factor and *VSF* is the variance sensitivity factor. The sensitivity factors can be obtained with a Monte Carlo simulation, or using analytical solutions of the diffusion approximation of light transport for simple geometries, or using the finite element method for heterogeneous models. The recovery method that uses the sensitivity factors relies on the assumptions that changes in statistical moments are linear within corresponding changes in absorption coefficient $\mu_a \pm \Delta\mu_a$ which is true for $\Delta\mu_a \rightarrow 0$. Additionally, the scattering properties should remain constant ($\Delta\mu'_s = 0$, where μ'_s is the reduced scattering coefficient). The error propagation analysis proposed in [27] allows to calculate the standard deviation in recovered absorption change ($\sigma\Delta\mu_a$) within j–th layer for assumed heterogeneous background optical properties. $\sigma\Delta\mu_a$ is calculated from the standard deviations of the three statistical moments, which may be statistically dependent as they are derived from the same DTOF curve. The existing covariances between ΔA, ΔT and ΔV are used in the error propagation model to account for a mutual statistical dependence. Assuming the dominant photon noise follows a Poisson distribution, the covariance matrix **Z** of the first three statistical moments of the DTOF takes the following expression [27]:

$$\mathbf{Z} = \begin{pmatrix} \text{cov}(\Delta A, \Delta A) & \text{cov}(\Delta A, \Delta T) & \text{cov}(\Delta A, \Delta V) \\ \text{cov}(\Delta T, \Delta A) & \text{cov}(\Delta T, \Delta T) & \text{cov}(\Delta T, \Delta V) \\ \text{cov}(\Delta V, \Delta A) & \text{cov}(\Delta V, \Delta T) & \text{cov}(\Delta V, \Delta V) \end{pmatrix} = \begin{pmatrix} 2\frac{1}{N_{tot}} & 0 & 0 \\ 0 & 2\frac{V}{N_{tot}} & 2\frac{m_3^c}{N_{tot}} \\ 0 & 2\frac{m_3^c}{N_{tot}} & 2\frac{m_4^c - V^2}{N_{tot}} \end{pmatrix} \quad (1)$$

m_3^c, and m_4^c represent the third and the fourth centralized moments of DTOF curve. The zeros in the covariance matrix indicate statistically independent measurands and non-zero terms indicate a statistical dependence. We used Monte Carlo simulations to generate data (DTOFs and sensitivity factors) for a three-layered adult human head model (scalp, skull, brain). We assume that a change in chromophores concentration can occur in two layers only: scalp and brain. The matrix

X represents the sensitivity factors for the two layers:

$$\mathbf{X} = \begin{pmatrix} MPP_{\text{scalp}} & MPP_{\text{brain}} \\ MTSF_{\text{scalp}} & MTSF_{\text{brain}} \\ VSF_{\text{scalp}} & VSF_{\text{brain}} \end{pmatrix} \tag{2}$$

Square roots of the diagonal elements of the following covariance matrix represent the standard deviations of the estimated absorption changes in the scalp and brain layers ($\sigma\Delta\mu_a$) [27]:

$$\sigma\Delta\mu_a = \sqrt{\text{diag}(\text{cov}(\Delta\mu_a, \Delta\mu_a))} = \sqrt{\text{diag}((\mathbf{X}^T\mathbf{Z}^{-1}\mathbf{X})^{-1})} \tag{3}$$

The square root operation is carried out element-wise for the diagonal matrix.

2.2. Error propagation for the Beer-Lambert law

We determined the standard deviations in estimation of the chromophores' concentrations: oxy- ($\sigma\Delta C_{HbO_2}$), deoxyhemoglobin ($\sigma\Delta C_{Hb}$) and cytochrome-c-oxidase ($\sigma\Delta C_{CCO}$). The implemented error propagation is similar to the method presented in [28] where authors derived the uncertainties of ΔC_{HbO_2} and ΔC_{Hb} for different choices of two wavelengths. The proposed method relies on the known absorption spectra of chromophores (Fig. 1), the calculated $\sigma\Delta\mu_a$ in Eq. (3), and the error propagation for the Beer-Lambert law. It was previously shown that CCO occurs in high concentration predominantly in the brain and that it is reasonable to neglect changes in CCO in the scalp for fNIRS studies [6,38,39]. Therefore, in our analysis we included twthe following mannero chromophores (oxy- and deoxyhemoglobin) in the scalp and three chromophores (including CCO) in the brain. Figure 1(a) shows 4, 8, 12, 16, 20, 25 and 32 wavelengths that evenly span the spectral range from 650 to 950 nm. Figure 1(b) shows different choices of 16 consecutive wavelengths separated by 12.5 nm.
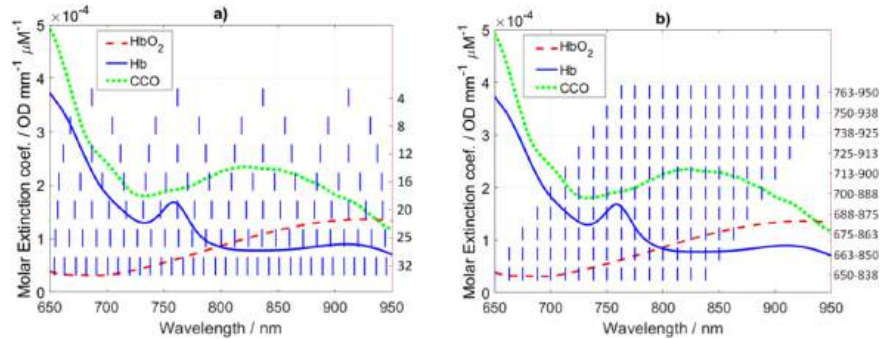

Fig. 1. Specific extinction coefficients of oxy- (HbO$_2$), deoxyhemoglobin (Hb) and cytochrome-c-oxidase (CCO) [1]. The vertical blue lines show the choices of wavelengths for the analysis of the standard deviations in the estimation of changes in chromophores concentrations for different number of wavelengths (a) and 16 consecutive wavelengths separated by 12.5 nm (b).

2.3. Monte Carlo simulations

Twenty-five sets of DTOFs and sensitivity factor matrices (**X**) were generated using Monte Carlo simulations for wavelengths from 650 to 950 nm in steps of 12.5 nm. The Monte Carlo code was presented and explained elsewhere [37].

There were simulated $5 \cdot 10^8$ photon packets to generate each DTOF and 10^8 to generate each set of sensitivity factors. The DTOFs were sampled at $i_{max} = 128$ time channels 19.5 picoseconds each. Usually, the signal to noise ratio of a DTOF is set within the limit of 1% of the DTOF maximum and the $\geq 1\%$ region is used for the statistical moments calculation [25]. The source-detector separation was set to 3 cm and the detector radius was set to 3 mm. The symmetry of the slab-based layered model (12×12×8 cm) allows positioning many detectors around a centrally-positioned source to significantly increase number of detected photons, hence decreasing the simulations time. Therefore, the detector was modeled as a ring of inner radius of 2.85 cm and outer radius of 3.15 cm with the center positioned at the centrally-located source. The simulations were carried out in reflectance geometry.

We assumed a three-layered model consisting of: scalp (4 mm), skull (7 mm) and brain ('semi-infinite'). The Monte Carlo simulations generate the sensitivity factors for every layer of the modeled medium [37]. We assumed the optical properties of the skull layer remain constant as in [20,40].

2.4. Spectra of absorption, reduced scattering and extinction coefficients

The absorption coefficients for the scalp and the brain layers were estimated assuming tissue constituents concentrations as in [33] and using their known absorption spectra. The constituents that contribute to the absorption spectra are summarized in Table 1. We added a fixed background value of $0.005 \, \text{mm}^{-1}$ to the absorption of scalp making the average absorption around $0.015 \, \text{mm}^{-1}$, which is closer to values reported in [41,42]. The values of absorption assumed for the brain are around $0.013 \, \text{mm}^{-1}$, which is close to the values reported in [43–47]. The absorption of skull depends less on wavelength [48–50] and the reported values of optical properties from different studies cover a wide range [48–54]. Only minor ripples [48] can be observed in the absorption spectra of skull in the range up to 900 nm and it is suggested that these can be neglected when analyzing light penetration [55]. Thus, it was assumed that the absorption coefficient of skull is constant across all wavelengths. Moreover, the extinction coefficients of water and lipids are much smaller than of oxy-, deoxyhemoglobin and CCO in the NIR region [1]. The resulting absorption coefficients, shown in Fig. 2(a), are between 0.01 and $0.02 \, \text{mm}^{-1}$ for wavelengths up to 913 nm and follow values as in [56–62].
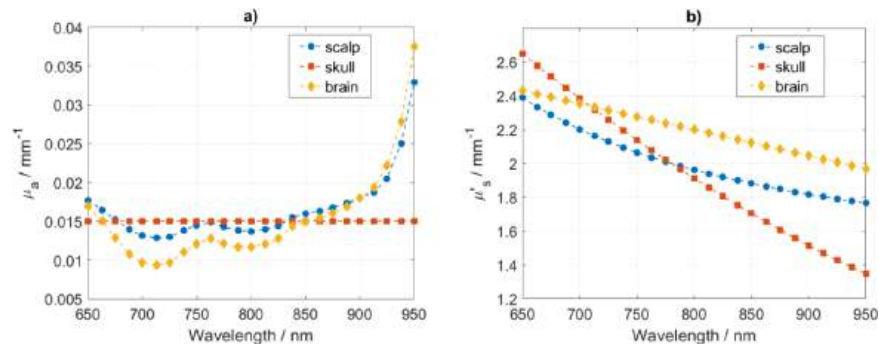

Fig. 2. Absorption coefficient μ_a (a) and reduced scattering coefficient μ'_s (b) for scalp, skull and brain layers.

A dominant Mie regime scattering within tissues shows a decrease in the reduced scattering coefficient with wavelength (λ) [41–43,45,46,48,50,63]. Mie scattering can be parameterized with scattering amplitude (a) and power (b) in the following manner: $\mu'_s = a\lambda^{-b}$. Values of the reduced scattering coefficient in near-infrared (NIR) region are around $2 \, \text{mm}^{-1}$ for scalp [41,48], $1.8 \, \text{mm}^{-1}$ for skull [50,63] and $2.2 \, \text{mm}^{-1}$ for brain [43,47,48,64]. As such, we assumed scatter

Table 1. Tissue constituents assumed for the three layers head model [33].

Layer	Thickness (mm)	C_{HbO_2} (µM)	C_{Hb} (µM)	StO_2 (%)	Lipid (%)	Water (%)	3 types of Cytochrome (µM)			Constant background (mm^{-1})	μ_a (mm^{-1})	
							Cytochrome c oxidase	Cytochrome b	Cytochrome c		690 nm	830 nm
Scalp	4	46	19	71	13	60	0	0	0	0.005	0.014	0.015
Skull	7	-	-	-	-	-	-	-	-	0.015	0.015	0.015
Brain	87	56	24	70	11.6	80	8	2.37	1.36	0	0.011	0.014

values as in [33] and in Fig. 2(b). The refractive index was set 1.4 for the media and 1 for the surrounding air.

2.5. Detection system: spectral responsivity (spectral efficiency)

It is necessary to define number of detected photons (N_{tot}) for the calculation of the standard deviation ($\sigma \Delta \mu_a$ in Eq. 3). To convert the simulated photon fluence rate expressed in photons per square millimeter per second into number of photons as detected by a measurement system, simulated DTOFs are scaled to set the integral across time and wavelength to 1.5 million detected photons. The simulated DTOFs and the calculated N_{tot} are shown in Fig. 3(a,b,d). The increase in the number of detected photons at longer wavelengths is in agreement with other studies [65]. A real detector's sensitivity is wavelength dependent and affects the measurements as shown in [66]. We consider the spectral responsivity based on a multialkali cathode detector, which is commonly used in TR-NIRS systems [23,66]. The responsivity characteristic was interpolated from values reported in [66] and shown in Fig. 3(c). The integrals of simulated DTOFs were scaled to match the spectral responsivity characteristic and, as previously, normalized across time and wavelength to set the total detected photons to 1.5 million (Fig. 3(d)).
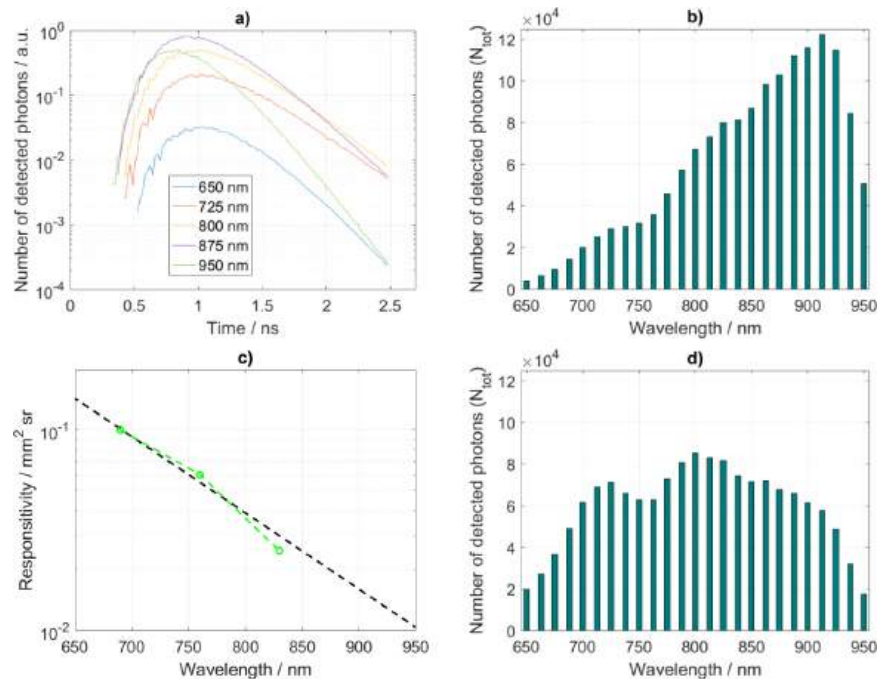

Fig. 3. (a) Examples of the DTOFs generated for the background optical properties that are shown in Fig. 2. Number of detected photons for the case when responsivity is not used (b). The responsivity of a detector based on a multialkali cathode (c) as interpolated using data (green points) reported in [66]. Number of detected photons when the detector's spectral responsivity is considered (d).

2.6. Wavelength selection analysis

The workflow of the analysis performed in this study and the steps involved are illustrated in Fig. 4.
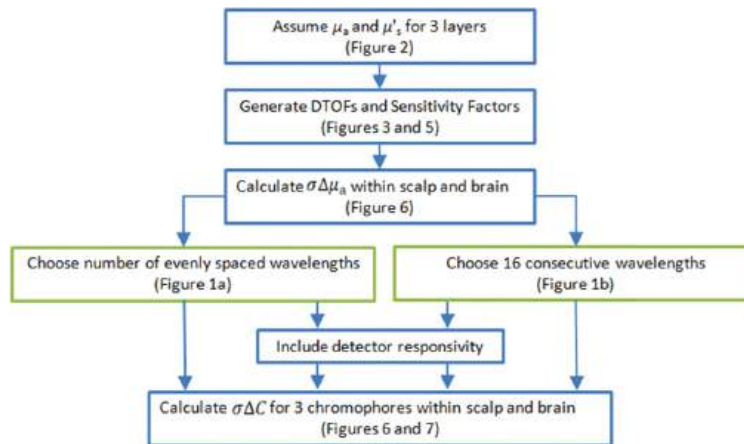
Fig. 4. Workflow of the procedure for the calculation of standard deviations of the estimated changes in concentrations of chromophores ($\sigma \Delta C$) using the error propagation for the moments method [27] and the Beer-Lambert law aiming to optimize wavelength choice.

3. Results

3.1. Sensitivity Factors and the standard deviation of changes in absorption: $\sigma \Delta \mu_a$

DTOFs generated with the Monte Carlo simulations are shown in Fig. 3(a). MPP is expressed in units of length and represents mean distance travelled by photons passing a layer (volume). The MPP is highest within the skull layer and reduces by about a factor of two going to the scalp layer and by a further factor of two going to the brain layer (Fig. 5(a)). On average, photons travel two times longer distance within scalp than brain. The average travel distance within brain is more than four times shorter as compared to the skull. The MTSF however is the distance travelled (MPP) weighted by the time of travel. Therefore, the maximum of MTSF is shifted to deeper layers as compared to the MPP. The MTSF is low within the scalp as the corresponding time of flight is short and increases significantly within the skull and brain (Fig. 5(b)). The VSF expresses the travelled distance (MPP) weighted by the time of travel squared, where weighting by the square of travel time pushes the maximum sensitivity even deeper. As a result, the sensitivity is further increased within the brain layer (Fig. 5(c)). Therefore, measurements of mean time of flight and variance are better suited for brain activity recovery. Furthermore, differences in the depth profiles of the MPP, MTSF and VSF support depth discrimination in parameters recovery using the moments method.
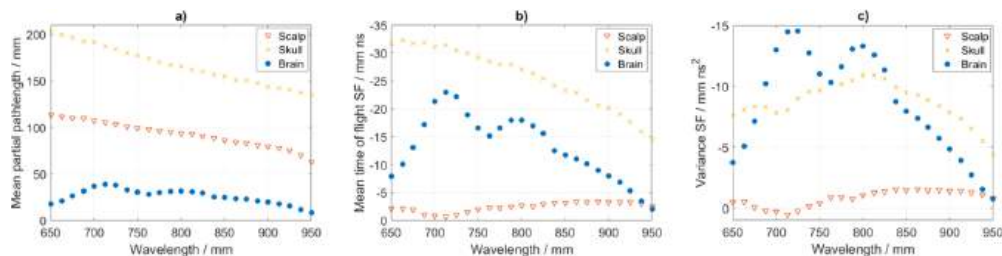

Fig. 5. Sensitivity factors for the background optical properties as in Table 1. *MPP* (a), *MTSF* (b) and *VSF* (c) are shown within following layers: scalp, skull and brain.

The MPP, MTSF and VSF as calculated within the scalp, skull and brain layers are shown in Fig. 5(a-c). We find that the MPP decreases with wavelength following the decrease in the values of the reduced scattering coefficient (Fig. 2(b)). The MTSF and VSF for the brain layer reveal stronger relation with the absorption than scatter as they follow the absorption spectra shape. The MPP, MTSF and VSF for the brain layer have peak values in the range between 720 and 800 nm, which follows the regions of lowest absorption coefficient as shown in Fig. 2(a).

The DTOFs and the sensitivity factors were used to calculate the standard deviations of changes in the absorption coefficients within the two layers (scalp and brain) using the method as introduced in section 2.1. Analyses follow methodology as in Fig. 4 and the detector spectral responsivity is considered accordingly. The calculated standard deviations at each wavelength are shown in Fig. 6. The detector responsivity (Fig. 3(c)) introduces increase in standard deviations with wavelength, which strictly follows the detector performance. The standard deviation is always higher in the brain. Photons travel path through the scalp and skull layers is much longer than through the brain (Fig. 5(a)), hence DTOFs are dominated by information originating in the scalp and/or skull layers.
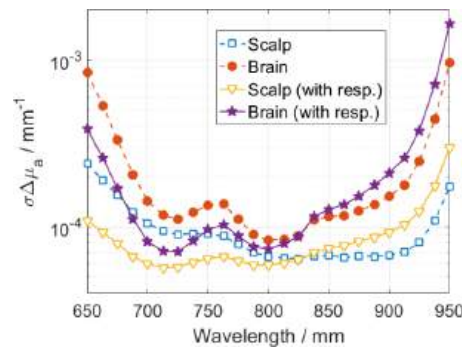

Fig. 6. Standard deviation of changes in the absorption coefficients within two layers: scalp and brain, considering the detector responsivity (with resp.) accordingly.

3.2.　Varying number of wavelengths

The standard deviations of the estimation of changes in concentrations ($\sigma\Delta C$) of three chromophores in two layers were calculated using: standard deviations of changes in absorption coefficient ($\sigma\Delta\mu_a$) as shown in Fig. 6, extinction coefficients as in Fig. 1 and the Beer-Lambert law. For the varying number of wavelengths analysis, we used MATLAB built-in function (spline) to interpolate $\sigma\Delta\mu_a$ in Fig. 6 for missing wavelengths. Results are presented in Fig. 7. The standard deviation of the estimation of CCO in the brain layer ($\sigma\Delta C_{CCO}^{brain}$) shows peak at 8 wavelengths which follows from the high values of extinction coefficients (Fig. 1(a)) and low values of $\sigma\Delta\mu_a$ (Fig. 6). Responsivity of the detector amplifies the standard deviation in all considered tissue constituents.

3.3.　Varying range of 16 consecutive wavelengths

The standard deviations of the estimated changes in concentrations ($\sigma\Delta C$) of three chromophores in two layers using different range of 16 consecutive wavelengths separated by 12.5 nm are presented in Fig. 8(a-b). Choice of wavelengths region influences the $\sigma\Delta C$ within scalp and brain layers differently following difference in $\sigma\Delta\mu_a$ within the scalp and brain (Fig. 6) and presence of two and three chromophores in the scalp and brain respectively. The $\sigma\Delta C$ in the brain is always higher as photons travel shorter distances within the brain. Therefore, $\sigma\Delta C$ in the brain is more sensitive to the choice of wavelengths. We aim to find the wavelengths band that
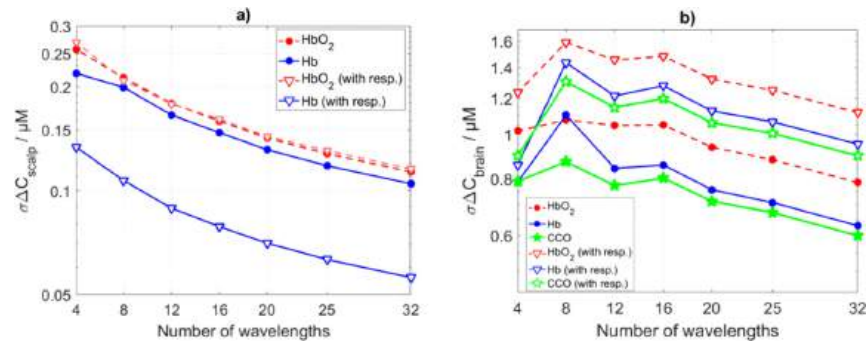
Fig. 7. Standard deviations of estimation of changes in concentrations ($\sigma \Delta C$) of chromophores within (a) scalp and (b) brain layers using varying number of wavelengths (as shown in Fig. 1(a)).

corresponds to minimal $\sigma \Delta C_{CCO}$ in the brain layer. In case the detector spectral responsivity is not included in the analysis, the minimal $\sigma \Delta C_{CCO}^{brain}$ of 0.40 µM is observed in the range from 725 to 913 nm (Fig. 8(b)). This region covers the absorption peak of CCO. When the detector responsivity is considered, the minimal $\sigma \Delta C_{CCO}^{brain}$ of 0.47 µM is observed in the range from 688 to 875 nm. Shorter wavelengths benefit more from the high detector responsivity than from the CCO absorption spectra. We repeated the analysis considering varying number of all detected photons N_{tot}. This way we can predict what is the detectable change of CCO concentration for a given number of collected photons. This analysis for the wavelength range of 700 to 888 nm is shown in Fig. 8(c). The maximum expected change in the concentration of CCO during functional brain activation is 4.5-5.5 µM [1]. The typical count rate for a spectral TR-NIRS system [25] is about 10^6 photons per second.
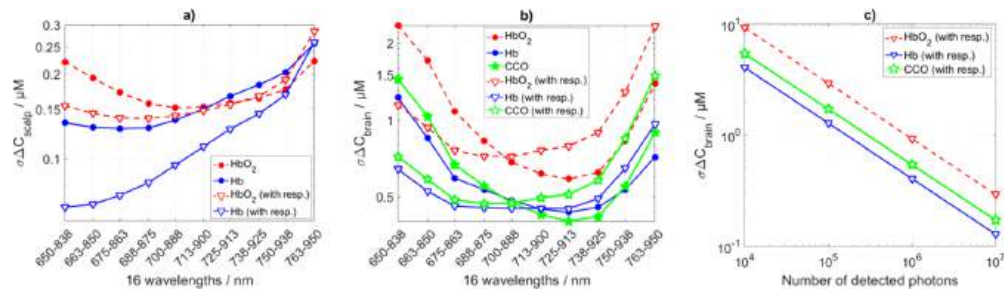

Fig. 8. Standard deviations of estimation of changes in concentrations ($\sigma \Delta C$) of chromophores within scalp (a) and brain (b) layers using varying range of 16 consecutive wavelengths (as shown in Fig. 2(b)). The standard deviation in change of CCO concentration in the brain at a given number of collected photons (c) for the 16 wavelengths between 700 and 888 nm. 'with resp.' indicates analysis considering the detector spectral responsivity.

4. Discussion

The error propagation analysis for the moments method was used in [27] to study how absorption coefficient recovery within two layers is influenced by the following: varying combination of statistical moments used, combinations of source-detector pairs, thickness of the top layer and source-detector distance. In this study we introduce the error propagation method to calculate the standard deviations in recovery of changes in concentrations of tissue constituents ($\sigma \Delta C$) within

head layers. We generated spectral TR-NIRS data and applied the error propagation method to optimize the choice of 16 consecutive wavelengths for the developed TR-NIRS system [25]. The optimization criteria was to minimize the uncertainty of recovery CCO concentration ($\sigma\Delta C_{\mathrm{CCO}}$) within the brain layer. We observed comparable $\sigma\Delta C$ for the three chromophores (HbO$_2$, Hb, CCO) analyzed. However, monitoring of the CCO is challenging as its low concentration requires high signal to noise ratio in raw data to detect changes in its oxidation state [1]. A recent study shows that monitoring CCO is possible with TR-NIRS [67]. Spectral responsivities vary between systems [34,67,68] and should be included in analyses. Here, we show system-specific methodology of wavelength selection as based on spectrally-resolved TR-NIRS shown in [25]. When the system responsivity was not used, the minimal $\sigma\Delta C_{\mathrm{CCO}}$ of 0.40 μM in the brain was observed for 16 consecutive wavelengths from 725 to 913 nm and separated by 12.5 nm. This region corresponds to the broad absorption peak of CCO in the NIR region. This choice of wavelengths corresponds to systems with flat responsivity spectra, e.g. [66,67]. Inclusion of detection responsivity spectrum shifts the optimal region towards shorter wavelengths from 688 to 875 nm (minimal $\sigma\Delta C_{\mathrm{CCO}}$ of 0.47 μM). This shift follows the detector's spectral performance that drops with wavelength. It was recently presented that the optimal number of 3, 4, 5 and 8 wavelengths are positioned almost evenly around the peak of the absorption spectra of CCO [34]. Similarly, a broadband NIRS system presented in [69] aiming to monitor changes in CCO was set to utilize the wavelengths range between 770 and 906 nm covering the absorption peak of CCO. Almost identical range (780 to 900 nm) was used in a previous broadband NIRS system for monitoring CCO changes as presented in [14]. The recently presented TR-NIRS system used wavelengths between 780 and 870 nm when demonstrating the system's ability to estimate changes in oxygenation and oxidate state of CCO [67]. These wavelengths correspond to the region where the performance of our detector is worse and the results of this study suggest that these wavelengths are not optimal for our system.

When changes in concentrations of multiple chromophores are of interest, a cross-talk between recovered chromophores concentrations can be expected [70]. As shown in [30,70], considering the CCO might introduce a noticeable cross-talk. However, as shown in [70] analyzing higher moments of the DTOF (e.g. the time of flight) reduces the cross-talk significantly.

The moments method [19] assumes that the probability of photons being absorbed within a layer is small, i.e. the layer absorption coefficient weighted by the mean pathlength is much smaller than 1: $MPP \cdot \Delta\mu_{\mathrm{a}} \ll 1$. The *MPP* is derived from diffusion theory with the perturbation approach that linearize the light propagation inverse problem around some base μ_{a} [71] assuming the $\Delta\mu_{\mathrm{a}} \to 0$. As such, if the $\Delta\mu_{\mathrm{a}}$ is expected to be high as related to the base value, an iterative approach can be utilized where the sensitivity factors are iteratively recalculated using previous step recovery as the new base. This approach follows other optical tomography recovery methods [72,73]. It is the suggested next research step.

5. Conclusions

We proposed a method based on the error propagation allowing to calculate uncertainty of estimation of changes in concentrations of chromophores in two layers for a multi-wavelength time-resolved near-infrared spectroscopy system.

The minimal standard deviation of estimated changes in concentration of CCO within the brain layer ($\sigma\Delta C_{\mathrm{CCO}}^{\mathrm{brain}} = 0.40$ μM) covered by scalp and skull was found for a set of wavelengths that cover the absorption peak of CCO: 725 to 913 nm.

For a realistic responsivity spectrum of a system the found optimal choice of wavelengths was shifted to direction of better performance: $\sigma\Delta C_{\mathrm{CCO}}^{\mathrm{brain}} = 0.47$ μM at 688 to 875 nm. The results suggest that the optimal choice of wavelengths is dependent on the specifications of a system.

Disclosures

The authors declare that there are no conflicts of interest related to this article.

References

1. G. Bale, C. E. Elwell, and I. Tachtsidis, "From Jobsis to the present day: a review of clinical near-infrared spectroscopy measurements of cerebral cytochrome-c-oxidase," J. Biomed. Opt. **21**(9), 091307 (2016).
2. M. Ferrari and V. Quaresima, "A brief review on the history of human functional near-infrared spectroscopy (fNIRS) development and fields of application," NeuroImage **63**(2), 921–935 (2012).
3. F. Scholkmann, S. Kleiser, A. J. Metz, R. Zimmermann, J. Mata Pavia, U. Wolf, and M. Wolf, "A review on continuous wave functional near-infrared spectroscopy and imaging instrumentation and methodology," NeuroImage **85**, 6–27 (2014).
4. H. N. Modi, H. Singh, G. Z. Yang, A. Darzi, and D. R. Leff, "A decade of imaging surgeons' brain function (part I): Terminology, techniques, and clinical translation," Surgery **162**(5), 1121–1130 (2017).
5. P. Pinti, I. Tachtsidis, A. Hamilton, J. Hirsch, C. Aichelburg, S. Gilbert, and P. W. Burgess, "The present and future use of functional near-infrared spectroscopy (fNIRS) for cognitive neuroscience," *Ann. N. Y. Acad. Sci.*, (2018).
6. C. Kolyva, A. Ghosh, I. Tachtsidis, D. Highton, M. Smith, and C. E. Elwell, "Dependence on NIRS Source-Detector Spacing of Cytochrome c Oxidase Response to Hypoxia and Hypercapnia in the Adult Brain," Adv. Exp. Med. Biol. **789**, 353–359 (2013).
7. M. F. Siddiqui, S. Lloyd-Fox, P. Kaynezhad, I. Tachtsidis, M. H. Johnson, and C. E. Elwell, "Non-invasive measurement of a metabolic marker of infant brain function," Sci. Rep. **7**(1), 1330 (2017).
8. G. Bale, S. Mitra, I. de Roever, M. Sokolska, D. Price, A. Bainbridge, R. Gunny, C. Uria-Avellanal, G. S. Kendall, J. Meek, N. J. Robertson, and I. Tachtsidis, "Oxygen dependency of mitochondrial metabolism indicates outcome of newborn brain injury," *J. Cereb. Blood Flow Metab.* (2018).
9. M. Caldwell, F. Scholkmann, U. Wolf, M. Wolf, C. Elwell, and I. Tachtsidis, "Modelling confounding effects from extracerebral contamination and systemic factors on functional near-infrared spectroscopy," NeuroImage **143**, 91–105 (2016).
10. F. Scholkmann, T. Hafner, A. J. Metz, M. Wolf, and U. Wolf, "Effect of short-term colored-light exposure on cerebral hemodynamics and oxygenation, and systemic physiological activity," Neurophotonics **4**(04), 1 (2017).
11. T. Takahashi, Y. Takikawa, R. Kawagoe, S. Shibuya, T. Iwano, and S. Kitazawa, "Influence of skin blood flow on near-infrared spectroscopy signals measured on the forehead during a verbal fluency task," NeuroImage **57**(3), 991–1002 (2011).
12. E. Kirilina, A. Jelzow, A. Heine, M. Niessing, H. Wabnitz, R. Bruhl, B. Ittermann, A. M. Jacobs, and I. Tachtsidis, "The physiological origin of task-evoked systemic artefacts in functional near infrared spectroscopy," NeuroImage **61**(1), 70–81 (2012).
13. N. M. Gregg, B. R. White, B. W. Zeff, A. J. Berger, and J. P. Culver, "Brain specificity of diffuse optical imaging: improvements from superficial signal regression and tomography," Front. Neuroenerg. **2**, 14 (2010).
14. C. Kolyva, I. Tachtsidis, A. Ghosh, T. Moroz, C. E. Cooper, M. Smith, and C. E. Elwell, "Systematic investigation of changes in oxidized cerebral cytochrome c oxidase concentration during frontal lobe activation in healthy adults," Biomed. Opt. Express **3**(10), 2550–2566 (2012).
15. I. Tachtsidis, T. S. Leung, A. Chopra, P. H. Koh, C. B. Reid, and C. E. Elwell, "False positives in functional near-infrared topography," Adv. Exp. Med. Biol. **645**, 307–314 (2009).
16. I. Tachtsidis and F. Scholkmann, "False positives and false negatives in functional near-infrared spectroscopy: issues, challenges, and the way forward," Neurophotonics **3**(3), 031405 (2016).
17. A. T. Eggebrecht, S. L. Ferradal, A. Robichaux-Viehoever, M. S. Hassanpour, H. Dehghani, A. Z. Snyder, T. Hershey, and J. P. Culver, "Mapping distributed brain function and networks with diffuse optical tomography," Nat. Photonics **8**(6), 448–454 (2014).
18. A. Torricelli, D. Contini, A. Pifferi, M. Caffini, R. Re, L. Zucchelli, and L. Spinelli, "Time domain functional NIRS imaging for human brain mapping," NeuroImage **85**(Pt 1), 28–50 (2014).
19. A. Liebert, H. Wabnitz, J. Steinbrink, H. Obrig, M. Moller, R. Macdonald, A. Villringer, and H. Rinneberg, "Time-resolved multidistance near-infrared spectroscopy of the adult head: intracerebral and extracerebral absorption changes from moments of distribution of times of flight of photons," Appl. Opt. **43**(15), 3037–3047 (2004).

20. A. Jelzow, H. Wabnitz, I. Tachtsidis, E. Kirilina, R. Bruhl, and R. Macdonald, "Separation of superficial and cerebral hemodynamics using a single distance time-domain NIRS measurement," Biomed. Opt. Express **5**(5), 1465–1482 (2014).

21. H. Wabnitz, M. Moeller, A. Liebert, H. Obrig, J. Steinbrink, and R. Macdonald, "Time-resolved near-infrared spectroscopy and imaging of the adult human brain," Adv. Exp. Med. Biol. **662**, 143–148 (2010).

22. M. Kacprzak, A. Liebert, W. Staszkiewicz, A. Gabrusiewicz, P. Sawosz, G. Madycki, and R. Maniewski, "Application of a time-resolved optical brain imager for monitoring cerebral oxygenation during carotid surgery," J. Biomed. Opt. **17**(1), 016002 (2012).

23. A. Gerega, D. Milej, W. Weigl, M. Botwicz, N. Zolek, M. Kacprzak, W. Wierzejski, B. Toczylowska, E. Mayzner-Zawadzka, R. Maniewski, and A. Liebert, "Multiwavelength time-resolved detection of fluorescence during the inflow of indocyanine green into the adult's brain," J. Biomed. Opt. **17**(8), 087001 (2012).

24. A. Abdalmalak, D. Milej, L. Norton, D. B. Debicki, T. Gofton, M. Diop, A. M. Owen, and K. St Lawrence, "Single-session communication with a locked-in patient by functional near-infrared spectroscopy," Neurophotonics **4**(04), 1 (2017).

25. A. Gerega, D. Milej, W. Weigl, M. Kacprzak, and A. Liebert, "Multiwavelength time-resolved near-infrared spectroscopy of the adult head: assessment of intracerebral and extracerebral absorption changes," Biomed. Opt. Express **9**(7), 2974–2993 (2018).

26. W. Weigl, D. Milej, A. Gerega, B. Toczylowska, M. Kacprzak, P. Sawosz, M. Botwicz, R. Maniewski, E. Mayzner-Zawadzka, and A. Liebert, "Assessment of cerebral perfusion in post-traumatic brain injury patients with the use of ICG-bolus tracking method," NeuroImage **85**(Pt 1), 555–565 (2014).

27. A. Liebert, H. Wabnitz, and C. Elster, "Determination of absorption changes from moments of distributions of times of flight of photons: optimization of measurement conditions for a two-layered tissue model," J. Biomed. Opt. **17**(5), 057005 (2012).

28. Y. Yamashita, A. Maki, and H. Koizumi, "Wavelength dependence of the precision of noninvasive optical measurement of oxy-, deoxy-, and total-hemoglobin concentration," Med. Phys. **28**(6), 1108–1114 (2001).

29. A. Corlu, R. Choe, T. Durduran, K. Lee, M. Schweiger, S. R. Arridge, E. M. C. Hillman, and A. G. Yodh, "Diffuse optical tomography with spectral constraints and wavelength optimization," Appl. Opt. **44**(11), 2082 (2005).

30. K. Uludağ, J. Steinbrink, A. Villringer, and H. Obrig, "Separability and cross talk: Optimizing dual wavelength combinations for near-infrared spectroscopy of the adult head," NeuroImage **22**(2), 583–589 (2004).

31. T. Funane, H. Atsumori, H. Sato, M. Kiguchi, and A. Maki, "Relationship between wavelength combination and signal-to-noise ratio in measuring hemoglobin concentrations using visible or near-infrared light," Opt. Rev. **16**(4), 442–448 (2009).

32. D. A. Boas, A. M. Dale, and M. A. Franceschini, "Diffuse optical imaging of brain activation: Approaches to optimizing image sensitivity, resolution, and accuracy," NeuroImage **23**, S275–S288 (2004).

33. T. Correia, A. Gibson, and J. Hebden, "Identification of the optimal wavelengths for optical topography: a photon measurement density function analysis," J. Biomed. Opt. **15**(5), 056002 (2010).

34. D. Arifler, T. Zhu, S. Madaan, and I. Tachtsidis, "Optimal wavelength combinations for near-infrared spectroscopic monitoring of changes in brain tissue hemoglobin and cytochrome c oxidase concentrations," Biomed. Opt. Express **6**(3), 933 (2015).

35. R. Re, D. Contini, L. Zucchelli, A. Torricelli, and L. Spinelli, "Effect of a thin superficial layer on the estimate of hemodynamic changes in a two-layer medium by time domain NIRS," Biomed. Opt. Express **7**(2), 264–278 (2016).

36. W. Becker and Hickl, *16 Channel TCSPC / FLIM Detectors* (User Handbook, January 2016).

37. A. Liebert, H. Wabnitz, N. Żołek, and R. Macdonald, "Monte Carlo algorithm for efficient simulation of time-resolved fluorescence in layered turbid media," Opt. Express **16**(17), 13188–13202 (2008).

38. C. Kolyva, A. Ghosh, I. Tachtsidis, D. Highton, C. E. Cooper, M. Smith, and C. E. Elwell, "Cytochrome c oxidase response to changes in cerebral oxygen delivery in the adult brain shows higher brain-specificity than haemoglobin," NeuroImage **85**(Pt 1), 234–244 (2014).

39. I. de Roever, G. Bale, R. J. Cooper, and I. Tachtsidis, "Functional NIRS Measurement of Cytochrome-C-Oxidase Demonstrates a More Brain-Specific Marker of Frontal Lobe Activation Compared to the Haemoglobins," Adv. Exp. Med. Biol. **977**, 141–147 (2017).

40. M. Kacprzak, A. Liebert, P. Sawosz, N. Zolek, and R. Maniewski, "Time-resolved optical imager for assessment of cerebral oxygenation," J. Biomed. Opt. **12**(3), 034019 (2007).

41. C. R. Simpson, M. Kohl, M. Essenpreis, and M. Cope, "Near-infrared optical properties of ex vivo human skin and subcutaneous tissues measured using the Monte Carlo inversion technique," Phys. Med. Biol. **43**(9), 2465–2478 (1998).

42. A. N. Bashkatov, E. A. Genina, V. I. Kochubey, and V. V. Tuchin, "Optical properties of human skin, subcutaneous and mucous tissues in the wavelength range from 400 to 2000 nm," J. Phys. D: Appl. Phys. **38**(15), 2543–2555 (2005).

43. P. van der Zee, "Measurement and modelling of the optical properties of human tissue in the near-infrared," Ph.D. thesis, University College London (University of London), (1992).

44. F. Bevilacqua, D. Piguet, P. Marquet, J. D. Gross, D. Jakubowski, V. Venugopalan, B. J. Tromberg, and C. Depeursinge, "Superficial tissue optical property determination using spatially resolved measurements close to the source: Comparison with Frequency Domain Photon Migration measurements," Proc. SPIE **3597**, 540–547 (1999).

45. F. Bevilacqua, D. Piguet, P. Marquet, J. D. Gross, B. J. Tromberg, and C. Depeursinge, "In vivo local determination of tissue optical properties: applications to human brain," Appl. Opt. **38**(22), 4939 (1999).

46. A. N. Yaroslavsky, P. C. Schulze, I. V. Yaroslavsky, R. Schober, F. Ulrich, and H. J. Schwarzmaier, "Optical properties of selected native and coagulated human brain tissues in vitro in the visible and near infrared spectral range," Phys. Med. Biol. **47**(12), 2059–2073 (2002).

47. P. V. D. Zee and M. Essenpreis, "Optical properties of brain tissue," Proc. SPIE **1888**, 454–465 (1993).

48. M. Firbank, M. Hiraoka, M. Essenpreis, and D. T. Delpy, "Measurement of the optical properties of the skull in the wavelength range 650-950 nm," Phys. Med. Biol. **38**(4), 503–510 (1993).

49. N. Ugryumova, S. J. Matcher, and D. P. Attenburrow, "Measurement of bone mineral density via light scattering," Phys. Med. Biol. **49**(3), 469–483 (2004).

50. A. N. Bashkatov, E. A. Genina, V. I. Kochubey, and V. V. Tuchin, "Optical properties of human cranial bone in the spectral range from 800 to 2000nm," in *Saratov Fall Meeting 2005* (SPIE 2006), p. 11.

51. P. Farzam, C. Lindner, U. Weigel, M. Suarez, A. Urbano-Ispizua, and T. Durduran, "Noninvasive characterization of the healthy human manubrium using diffuse optical spectroscopies," Physiol. Meas. **35**(7), 1469–1491 (2014).

52. P. Farzam, P. Zirak, T. Binzoni, and T. Durduran, "Pulsatile and steady-state hemodynamics of the human patella bone by diffuse optical spectroscopy," Physiol. Meas. **34**(8), 839–857 (2013).

53. A. Pifferi, A. Torricelli, P. Taroni, A. L. Bassi, E. Chikoidze, E. Giambattistelli, and R. Cubeddu, "Optical biopsy of bone tissue: a step toward the diagnosis of bone pathologies," J. Biomed. Opt. **9**(3), 474–480 (2004).

54. Y. Xu, N. Iftimia, H. Jiang, L. Key, and M. Bolster, "Imaging of in vitro and in vivo bones and joints with continuous-wave diffuse optical tomography," Opt. Express **8**(7), 447–451 (2001).

55. S. L. Jacques, "Optical properties of biological tissues: a review," Phys. Med. Biol. **58**(11), R37–R61 (2013).

56. A. Custo, W. M. Wells 3rd, A. H. Barnett, E. M. Hillman, and D. A. Boas, "Effective scattering coefficient of the cerebral spinal fluid in adult head models for diffuse optical imaging," Appl. Opt. **45**(19), 4747–4755 (2006).

57. B. Montcel, R. Chabrier, and P. Poulet, "Time-resolved absorption and hemoglobin concentration difference maps: a method to retrieve depth-related information on cerebral hemodynamics," Opt. Express **14**(25), 12271–12287 (2006).

58. D. Comelli, A. Bassi, A. Pifferi, P. Taroni, A. Torricelli, R. Cubeddu, F. Martelli, and G. Zaccanti, "In vivo time-resolved reflectance spectroscopy of the human forehead," Appl. Opt. **46**(10), 1717–1725 (2007).

59. A. H. Barnett, J. P. Culver, A. G. Sorensen, A. Dale, and D. A. Boas, "Robust inference of baseline optical properties of the human head with three-dimensional segmentation from magnetic resonance imaging," Appl. Opt. **42**(16), 3095–3108 (2003).

60. P. Sawosz, S. Wojtkiewicz, M. Kacprzak, W. Weigl, A. Borowska-Solonynko, P. Krajewski, K. Bejm, D. Milej, B. Ciszek, R. Maniewski, and A. Liebert, "Human skull translucency: post mortem studies," Biomed. Opt. Express **7**(12), 5010–5020 (2016).

61. M. Jager and A. Kienle, "Non-invasive determination of the absorption coefficient of the brain from time-resolved reflectance using a neural network," Phys. Med. Biol. **56**(11), N139–N144 (2011).

62. E. Okada and D. T. Delpy, "Near-infrared light propagation in an adult head model. I. Modeling of low-level scattering in the cerebrospinal fluid layer," Appl. Opt. **42**(16), 2906–2914 (2003).

63. A. Torricelli, A. Pifferi, P. Taroni, E. Giambattistelli, and R. Cubeddu, "In vivo optical characterization of human tissues from 610 to 1010 nm by time-resolved reflectance spectroscopy," Phys. Med. Biol. **46**(8), 2227–2237 (2001).

64. M. Azimipour, R. Baumgartner, Y. Liu, S. L. Jacques, K. Eliceiri, and R. Pashaie, "Extraction of optical properties and prediction of light distribution in rat brain tissue," J. Biomed. Opt. **19**(7), 075001 (2014).

65. H. Sato, M. Kiguchi, F. Kawaguchi, and A. Maki, "Practicality of wavelength selection to improve signal-to-noise ratio in near-infrared spectroscopy," NeuroImage **21**(4), 1554–1562 (2004).

66. H. Wabnitz, D. R. Taubert, M. Mazurenka, O. Steinkellner, A. Jelzow, R. Macdonald, D. Milej, P. Sawosz, M. Kacprzak, A. Liebert, R. Cooper, J. Hebden, A. Pifferi, A. Farina, I. Bargigia, D. Contini, M. Caffini, L. Zucchelli, L. Spinelli, R. Cubeddu, and A. Torricelli, "Performance assessment of time-domain optical brain imagers, part 1: basic instrumental performance protocol," J. Biomed. Opt. **19**(8), 086010 (2014).

67. F. Lange, L. Dunne, L. Hale, and I. Tachtsidis, "MAESTROS: A Multiwavelength Time-Domain NIRS System to Monitor Changes in Oxygenation and Oxidation State of Cytochrome-C-Oxidase," IEEE J. Sel. Top. Quantum Electron. **25**(1), 1–12 (2019).

68. R. Re, D. Contini, M. Turola, L. Spinelli, L. Zucchelli, M. Caffini, R. Cubeddu, and A. Torricelli, "Multi-channel medical device for time domain functional near infrared spectroscopy based on wavelength space multiplexing," Biomed. Opt. Express **4**(10), 2231–2246 (2013).

69. G. Bale, S. Mitra, J. Meek, N. Robertson, and I. Tachtsidis, "A new broadband near-infrared spectroscopy system for in-vivo measurements of cerebral cytochrome-c-oxidase changes in neonatal brain injury," Biomed. Opt. Express **5**(10), 3450–3466 (2014).

70. K. Uludag, M. Kohl, J. Steinbrink, H. Obrig, and A. Villringer, "Cross talk in the Lambert-Beer calculation for near-infrared wavelengths estimated by Monte Carlo simulations," J. Biomed. Opt. **7**(1), 51 (2002).

71. S. R. Arridge, "Photon-measurement density functions. Part I : Analytical forms," Appl. Opt. **34**(31), 7395–7409 (1995).

72. S. R. Arridge, "Optical tomography in medical imaging," Inverse Problems **15**(2), R41–R93 (1999).

73. H. Dehghani, M. E. Eames, P. K. Yalavarthy, S. C. Davis, S. Srinivasan, C. M. Carpenter, B. W. Pogue, and K. D. Paulsen, "Near infrared optical tomography using NIRFAST: Algorithm for numerical model and image reconstruction," Commun. Numer. Methods Eng. **25**(6), 711–732 (2009).

Performance of measurands in time-domain optical brain imaging: depth selectivity versus contrast-to-noise ratio

ALEH SUDAKOU,[1,*] **LIN YANG,**[2] **HEIDRUN WABNITZ,**[2]
STANISLAW WOJTKIEWICZ,[1] **AND ADAM LIEBERT**[1]

[1] *Nalecz Institute of Biocybernetics and Biomedical Engineering Polish Academy of Sciences, Trojdena 4, 02-109 Warsaw, Poland*
[2] *Physikalisch-Technische Bundesanstalt, Abbestraße 2-12, 10587 Berlin, Germany*
*asudakou@ibib.waw.pl

Abstract: Time-domain optical brain imaging techniques introduce a number of different measurands for analyzing absorption changes located deep in the tissue, complicated by superficial absorption changes and noise. We implement a method that allows analysis, quantitative comparison and performance ranking of measurands under various conditions – including different values of reduced scattering coefficient, thickness of the superficial layer, and source-detector separation. Liquid phantom measurements and Monte Carlo simulations were carried out in two-layered geometry to acquire distributions of times of flight of photons and to calculate the total photon count, mean time of flight, variance, photon counts in time windows and ratios of photon counts in different time windows. Quantitative comparison of performance was based on objective metrics: relative contrast, contrast-to-noise ratio (CNR) and depth selectivity. Moreover, the product of CNR and depth selectivity was used to rank the overall performance and to determine the optimal source-detector separation for each measurand. Variance ranks the highest under all considered conditions.

1. Introduction

Near-infrared spectroscopy (NIRS) is a safe and non-invasive optical tool that allows the monitoring of signals containing information about tissue optical properties in real-time at the patient's bedside. A number of clinical trials have paved the way towards a broad clinical use of NIRS today for diverse applications [1], which is highlighted by an increasing number of commercially available NIRS devices [2]. The important clinically relevant information, e.g. cerebral metabolism [3], tissue perfusion and oxygenation [4], allow to study physiological conditions and results of clinical interventions.

Functional NIRS (fNIRS) is a fast developing methodology based on the assessment of changes in the absorption coefficient of tissues related to concentration changes in oxy- and deoxy-hemoglobin. fNIRS enables the monitoring of changes in tissue oxygenation and hemodynamic changes associated with neuronal activity [5]. The method has been proven as an effective tool for neuroscience with diverse applications [6,7].

The optical signals measured on the surface of the head contain entangled information originating within the extracerebral layer, i.e. scalp and skull, and the deep layer, i.e. brain. The physiological changes in the scalp layer can mask the hemodynamic changes in the cerebral layer, which is the major cause of false-positive results in fNIRS studies [8]. As such, the effectiveness of the fNIRS method improves with increased sensitivity to brain tissue [1].

fNIRS methods can be classified as continuous wave (CW), frequency domain (FD) and time domain (TD) according to their measured signal. The current study is focused on the assessment of the effectiveness of time-domain fNIRS to detect absorption changes in the brain cortex

and reduce the contamination of the signals caused by hemoglobin concentration changes of the extracerebral tissues. We report on measurands that can be (in part) relevant for all three modalities: CW, FD and TD-NIRS. TD-NIRS uses the most sophisticated instruments and provides superior information on the propagation of light in tissue. The advances in laser and detector technologies have reduced the instrumental costs and improved the performance of measurements allowing more information to be acquired and with more compact systems [9,10].

In brain studies, the signals in TD-NIRS are acquired in diffuse reflectance geometry by emitting short pulses of light, on the order of picoseconds in width, into the tissue and measuring the arrival times of remitted photons using time-correlated single photon counting (TCSPC) electronics, which provides the distribution of times of flight of photons (DTOF). Several methods of analyzing the DTOF have been developed. The fitting method uses essentially the entire DTOF for accurate estimation of the absolute values of absorption and reduced scattering coefficients in an optically turbid, homogeneous medium [11]. On the contrary, if monitoring of absorption changes is of interest, it is beneficial to calculate a few measurands that characterize the DTOF profile. A few approaches to analyze DTOFs include Mellin-Laplace moments [12], time-dependent mean partial pathlengths (TMPP) [13] and time segmented analysis [14]. The measurands used in the present work follow the choice used by Wabnitz *et al.*, [15,16]: statistical moments (number of photons, mean time of flight and variance) [17], photon counts in time windows [18,19] and ratios of photon counts in different time windows [18,20]. Currently, there is no quantitative comparison of the various measurands that would suggest the optimal choice for the purpose of monitoring small absorption changes in the deeper layers. Furthermore, such comparison could demonstrate the features of the various measurands and thus help interpret *in-vivo* measurements.

The theoretical background of the present work was presented in previous related studies [15,16,21]. In [21] it was shown that the higher-order moments reveal higher sensitivity to changes in absorption appearing in deeper tissues. Authors of [15] introduced methods for characterizing the performance of TD-fNIRS systems to detect, localize, and quantify small absorption changes in deep tissue compartments. In the recent study [16] it was shown that the ratios of photon counts in late time windows can yield the highest depth selectivity. However, it is expected that the practical utility of these measurands can be impeded by noise as the late time windows have particularly high relative noise levels.

In the present work we extend the analyses presented in [16] to include noise, which is often a limiting factor in fNIRS measurements, and propose a metric to rank the measurands (moments of DTOFs, time windows and ratios of photon counts) in terms of their overall performance in monitoring absorption changes in the deeper (brain cortex) layer. The main aim of this work is to provide a quantitative comparison of measurands' performances, and supplement it by including the dependence on other parameters, e.g. reduced scattering coefficient, thickness of the superficial layer, and the source-detector separation. We assess the performance of the various measurands based on three objective metrics: relative contrast to absorption changes in each layer, contrast-to-noise ratio (CNR) for each layer, and depth selectivity. A desired measurand should have high contrast to absorption changes in the deeper layer and little influence from absorption changes in the superficial layer. The product of CNR for the deeper layer and depth selectivity is proposed as a metric to rank measurands in terms of their overall performance. This metric incorporates the sensitivity to the deeper layer, contamination from the superficial layer and noise relative to the signal. We carried out TD-NIRS measurements on two-layered liquid phantoms with the absorption changing in each layer separately. The analysis using simulated data were repeated for various values of reduced scattering coefficient, thickness of the superficial layer and source-detector separation.

2. Measurands

This section introduces the analytical expressions of the measurands that exploit statistical moments and time windows. These measurands were calculated from measured DTOFs and also from simulated DTOFs convolved with the experimental instrument response function (IRF). In this study, we consider a 4 ns long range of the DTOFs to calculate the measurands. Within this range the photon counts at different times in the DTOF can differ by up to 4 orders of magnitude, i.e. the background signal is 0.01% of the maximum photon count. Usually the region that has $\geq 1\%$ of the maximum photon count (2 orders of magnitude) is used for analyses of DTOFs [22], i.e. a much smaller dynamic range.

Normalized moments of order n of a distribution function can be defined by [17]:

$$m_n = \sum_{i=1}^{i_{max}} t_i^n N_i \bigg/ \sum_{i=1}^{i_{max}} N_i, \tag{1}$$

where m_n is the nth normalized moment, t_i is the time corresponding to time channel i, and N_i is the number of detected photons in time channel i. In particular, we focus on three statistical moments: total number of photons ($m_0 = N$), mean time of flight (m_1) and variance ($V = m_2 - m_1^2$). V is the second centralized moment, which is related to the first two moments. For the calculation of N the temporal dependence of the photon counts is not used and this measurand represents the measure of light intensity that can be obtained with continuous-wave NIRS systems.

The time windows of equal width were defined in accordance with the definition used in the nEUROPt protocol [15]. The width of 500 ps results in eight consecutive time windows within the 4 ns range. The photon count (N_k) in the kth time window, between a and b time channels, is obtained by the summation:

$$N_k = \sum_{i=a}^{b} N_i \tag{2}$$

The ratio of the photon counts in different time windows ($N_{l/e}$) is calculated as:

$$N_{l/e} = \frac{N_l}{N_e}, \tag{3}$$

where N_l and N_e are the photon counts in later (l) and earlier (e) time windows, respectively. These ratios, similar to m_1 and V, have the potential to eliminate the influence of superficial changes on the signals, providing high sensitivity to changes appearing in the deeper regions, e.g. cerebral cortex.

3. Metrics for comparing TD-NIRS measurands

This section defines five metrics, some of which were introduced in the nEUROPt protocol [15]. They can provide comparable quantitative information about the performance of different measurands with respect to sensing of small absorption changes in layered structures.

3.1. Relative contrast

Relative contrast (C) is defined as the relative change of a measurand (M) with respect to its baseline value:

$$C_i = \frac{M_i - M_0}{M_0}, \tag{4}$$

where M_0 is the baseline value of a measurand and M_i is its value after an absorption change in layer i. Relative contrast will depend on the location, the volume and the magnitude of the absorption change and such dependence is different for different measurands, which in turn allows for various depth-resolved analyses. Relative contrast is dimensionless and hence appropriate for

comparing any measurands. However, relative contrast does not reflect the uncertainty of the measurand nor the contamination level due to unwanted absorption changes in the superficial layer.

3.2. Noise

The photon noise is the main limitation in optical *in-vivo* measurements, mainly due to the safety limitations for laser power. The standard deviation of measurands due to photon noise (σ) follows Poisson statistics and can be calculated from measured or simulated DTOF. The analytical expressions for σ of the three statistical moments were given in Liebert *et al.*, [17]. The photon counts in different time channels (N_i) are assumed to be uncorrelated, i.e. statistically independent, and the noise for each time channel is assumed to follow Poisson statistics [23]. Then, the following equations can be derived by applying the propagation of uncertainty in a similar manner as shown in Liebert *et al.*, [24]:

$$\sigma^2(N) = \sum N_i = N \tag{5}$$

$$\sigma^2(m_1) = \frac{V}{N} \tag{6}$$

$$\sigma^2(V) = \frac{m_{4,C} - V^2}{N}, \tag{7}$$

where $m_{4,C}$ is the fourth centralized moment and is related to the first four moments ($m_{4,C} = m_4 - 4m_3m_1 + 6m_2m_1^2 - 3m_1^4$). The following analytical expression is used for σ of the photon count within k^{th} time window, which contains time channels between a_k and b_k:

$$\sigma^2(N_k) = \sum_{i=a_k}^{b_k} N_i \tag{8}$$

The following analytical expression for the standard deviation of the ratios of photon counts in time windows was derived by applying the propagation of uncertainty using the photon noise within late $\sigma(N_l)$ and early $\sigma(N_e)$ time windows:

$$\sigma^2(N_{l/e}) = N_{l/e}^2 \left(\frac{\sigma(N_e)^2}{N_e^2} + \frac{\sigma(N_l)^2}{N_l^2} \right) \tag{9}$$

Note that instead of analytically calculating photon noise, it is possible to estimate the standard deviation directly from a number of repeated measurements. However, this 'measured' noise typically results in a higher noise level for all measurands, as it includes the instrumental noise as well. While the photon statistics remains the dominant source of noise in NIRS measurements.

3.3. Contrast-to-noise ratio

Contrast-to-noise ratio is the ratio between the change in a measurand ($M_i - M_0$), which originates from a change in absorption in layer i, and its standard deviation during baseline measurement ($\sigma(M_0)$) [15]:

$$CNR_i = \frac{M_i - M_0}{\sigma(M_0)} \tag{10}$$

Note that the definition of contrast used in *CNR* is different to the definition of relative contrast. σ can be calculated using Eqs. (5)–(9), which will include only photon noise, or using standard deviation of repeated measurements, which will also include instrumental noise. We assume the photon noise as the dominant source of noise and neglect the instrumental noise. *CNR* is dimensionless and hence appropriate for comparing different measurands. For brain studies, a good measurand should present high *CNR* for the deeper layer. However, *CNR* does not contain information about the level of contamination from the superficial layer.

3.4.　Depth selectivity

Depth selectivity (S) is defined as the ratio of the relative contrasts in two layers [15]:

$$S = \frac{C_2}{C_1} = \frac{M_2 - M_0}{M_1 - M_0}. \tag{11}$$

The nominator and the denominator correspond to a change in a measurand due to an absorption change in the deeper layer ($i = 2$) and in the superficial layer ($i = 1$), respectively. For estimation of this metric, the changes in absorption in the two layers must be of equal magnitude. It reflects the sensitivity of a measurand to the deeper layer compared to the superficial layer. A higher value of S indicates the measurand will be less influenced by absorption changes in the extracerebral layer, which is helpful for imaging absorption changes in the cerebral tissue. However, this metric does not reflect the uncertainty of a measurand.

3.5.　Product of depth selectivity and contrast-to-noise ratio for the deeper layer

We propose a new metric that combines the depth selectivity and the contrast-to-noise ratio in the deeper layer to give a score for the overall performance of a measurand for estimation of absorption changes in the deeper layer:

$$S \times CNR_2 = \frac{(M_2 - M_0)^2}{\sigma(M_0) \times (M_1 - M_0)}. \tag{12}$$

The product of S and CNR_2 represents a combination of sensitivity to the deeper layer, the influence of contamination from the superficial layer and the uncertainty in comparison to the contrast. This quantity is dimensionless and hence suitable for comparing performance of measurands of different units.

4.　Implementation

4.1.　TD-NIRS system

A supercontinuum laser FIU-15 PP (NKT Photonics) equipped with a variable bandpass filter VARIA (NKT Photonics) with a bandwidth of 10 nm was used as the light source providing picosecond light pulses with a repetition rate of 39 MHz. The filter was set to 760 nm. The output beam was guided to the phantom by a 1.6 m long multimode graded index fiber (core diameter 400 μm, NA 0.27, Leoni, Germany), and then collected by another 1.6 m long multimode graded index fiber (core diameter 600 μm, NA 0.22, Leoni, Germany). Both fibers' ends were embedded into a black fiber holder to prevent stray light and ambient light from entering the detecting fiber, and then faced the plexiglass windows of the phantom container.

A hybrid photomultiplier module (HPM-100-50, Becker & Hickl, Germany) received the light collected by the detecting fiber. A shutter, a motorized neutral-density attenuator, a collimator, and a focusing lens were placed between detecting fiber's end and detector to adapt the intensity and to properly image the detector fiber onto the detector.

The detected single-photon pulses were recorded by a time-correlated single photon counting (TCSPC) module (SPC-150, Becker & Hickl, Germany). Each DTOF contained 4096 time channels and every time channel was 4.07 ps in width. The photon counts in time windows (Eq. (2)) were calculated using the time channels inside the corresponding 500 ps time window, and the photon counts in the time channels that were on the limits were linearly interpolated.

The proper recording of the IRF is crucial for the accuracy in TD-NIRS measurements. Here the fibers were mounted into a cage system, and thin scatterers were included to engage the full aperture of both fibers [25]. The distance between the two fibers' ends (54 mm) determined the time shift between IRF and DTOF measurements.

4.2. Phantom measurements

Intrinsic optical properties of scattering and absorbing components may vary for different brands and even for different batches of scattering and absorbing components, especially so for India ink [26]. The intrinsic absorption coefficient of India ink (Higgins Ink #44201, Chartpak, USA) and the intrinsic reduced scattering coefficient of 20% Intralipid (Fresenius) were characterized in a 30 mm thick homogenous phantom container by measuring in reflectance and in transmittance geometries and applying the procedure that is described in detail in [26]. The characterization of absorption (μ_a) was carried out within the nominal values from 0 to $0.02\,\text{mm}^{-1}$ at 750 nm with 6 stepwise changes in India ink concentrations, while the nominal value of scattering was fixed at around $1\,\text{mm}^{-1}$. The characterization of scattering (μ_s') was carried out within the range from 0.5 to $1.5\,\text{mm}^{-1}$ at 750 nm with 3 stepwise changes in 20% Intralipid concentrations, while no India ink was added.

The two-layered phantom container, described in [15,27], was used for the layered liquid phantom measurements in reflectance geometry. The front wall was 2 mm thick and contained plexiglass windows of 7 mm in diameter for the source and the detector fibers. The time light travels through the plexiglass windows is subtracted from the time of arrival of photons. The thicknesses of the two compartments were 10 and 40 mm, and they were separated by a 50 µm thick translucent Mylar foil (DuPont). The distance between the source and detector fibers was set to 30 mm. Each DTOF was measured with a collection time of 1 s and 100 repetitions. The photon count rate of single DTOFs during homogeneous measurement was kept close to $5 \times 10^5\,\text{s}^{-1}$ to prevent counting loss and shape distortions of the DTOF due to dead time effects (see Fig. 414 in [28]). Single DTOFs were used for the photon noise calculation (Eqs. (5)–(9)) and the average of 100 DTOFs was used for calculating the values of the measurands (Eqs. (1)–(3)).

The target baseline optical properties were $\mu_a = 0.01\,\text{mm}^{-1}$ and $\mu_s' = 1\,\text{mm}^{-1}$ at 760 nm. A specific solution of India ink, water and 20% Intralipid was separated in three equal parts and added to increase absorption properties in one of the compartments by a total of 15% ($\Delta\mu_a = 0.0015\,\text{mm}^{-1}$) without changing the scattering properties. Then the liquid was removed from the container, and the experiment was repeated with another solution added into the other compartment in three steps to increase the other compartment's absorption properties from baseline by a total of 15% without changing the scattering properties. Therefore, four sets of measurements were used for the present study: i) homogeneous medium before adding absorber to the superficial layer, ii) after increasing absorption in the superficial layer by 15%, iii) homogeneous medium before adding absorber to the deeper layer, and iv) after increasing absorption in the deeper layer by 15%. The protocol allows to study measurands' ability to reflect changes in the deeper layer as well as in the superficial layer.

The considered absorption changes are somewhat higher than typically observed during functional near-infrared spectroscopy (fNIRS) studies [29,30]. The higher absorption changes were chosen to obtain results with better signal-to-noise ratio with regard to intrinsic uncertainties contained in measurements and Monte Carlo simulations. The linearity regime in which the changes in the measurands have a linear dependence on the absorption changes, as discussed in [15], is commonly assumed for many methods of analyzing fNIRS measurements, e.g. [21]. The three moments of DTOFs have good linearity for up to 40% change in absorption in any of the two layers of the model (Fig. 6 in [15]). Thus, we can assume that the scenario considered in this work, i.e. 15% change in absorption in each layer, is within the linear regime.

The position of time zero, i.e. the start of the first time window, was defined as the barycenter of the measured instrument response function (IRF) in the interval between the points of half maximum [15]. IRF was measured twice, at the start and end of the experiment, and the timing drift was negligible.

4.3. Monte Carlo simulations

Monte Carlo simulations (MC) were carried out using the code that was introduced by Wojtkiewicz *et al.*, [31], which evolved from the code reported by Liebert *et al.*, [32]. The symmetry of the slab-based layered model allows positioning a ring of many detectors around a center-located source to significantly increase the detection area and proportionally decrease the computational time. The optodes arrangement is shown in Fig. 1. The radius of each circular detector was set to 1 mm. The model (200×200×80 mm) was divided into uniform cube voxels of 0.25 mm width and consisted of the superficial layer (thickness 5, 10 or 15 mm) and the deeper layer. The superficial layer thicknesses were chosen based on the typical scalp thicknesses for an adult head, e.g. as in [33]. The refractive index was set to 1.33 and the scattering was assumed to be isotropic. Three MC simulations were carried out to mimic the measurement protocol: homogeneous model with $\mu_a = 0.01$ mm^{-1}, 15% increase in absorption in the superficial layer only, and 15% increase in absorption in the deeper layer only.
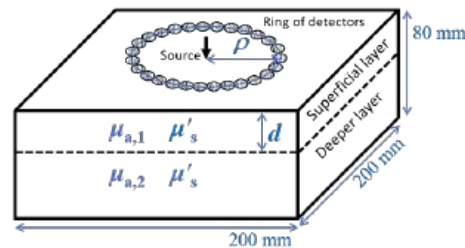

Fig. 1. The two-layered model for the Monte Carlo simulations.

MC simulations and analyses were repeated for the varying values of parameters as listed in Table 1. The first row lists the baseline optical properties for the homogeneous phantom measurements estimated with the curve fitting method [11,34] using NIRFASTer software [35]. The fitting method used the analytical solution of the radiative transfer equation under the diffusion approximation with extrapolated boundary conditions for time-resolved reflectance in a homogeneous slab. The second row lists the nominal values of baseline optical properties as used in the MC simulations. A total number of 2×10^9 and 9×10^9 photon packets were simulated for ρ up to 35 mm and for ρ larger than 35 mm, respectively. The simulated DTOFs were sampled at 700 time channels with 10 ps width. All DTOFs were convolved with the measured IRF and the first 400 time channels were used for further calculations as shown in Fig. 2(a). The three moments were calculated using this whole range and each of the eight time windows included 50 time channels.

Table 1. Model parameters used in Monte Carlo simulations and phantom data. μ_s' – reduced scattering coefficient of both layers, d – superficial layer thickness, ρ – source-detector separation. In all cases, absorption (μ_a) was increased separately within both layers by 15%.

	μ_a / mm^{-1}	μ_s' / mm^{-1}	d / mm	ρ / mm
Phantom	0.0102	1.09	10	30
Nominal	0.01	1.0	10	30
Varying μ_s'	0.01	0.5; 1.0; 1.5	10	30
Varying d	0.01	1.0	5; 10; 15	30
Varying ρ	0.01	1.0	10	10; 15; 20; 25; 30; 35; 40; 45; 50

All simulated DTOFs after convolution were scaled to match the measurement using the scaling factor, which was calculated by scaling measured and simulated curves for the homogeneous
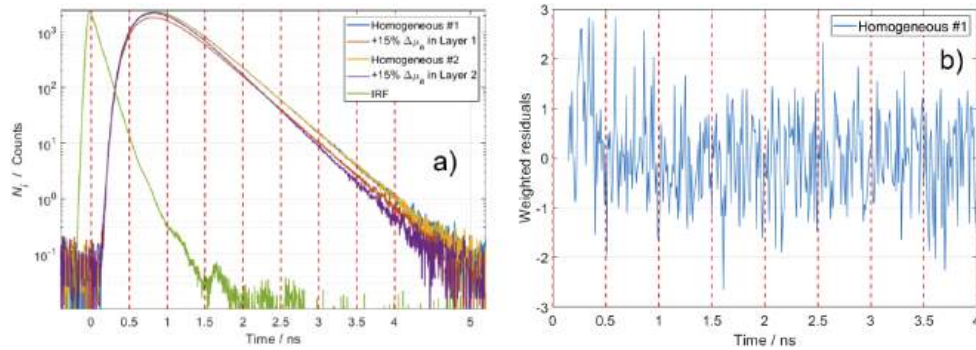
Fig. 2. (a) Measured DTOFs and IRF (both averaged over 100 repetitions) after background subtraction and correction for different time delays; time channel width is 4.07 ps. (b) Weighted residuals for comparison between a single measured DTOF and a simulated DTOF convolved with IRF for the phantom measurement parameters, which are shown in the first row of Table 1; time channel width was interpolated to 10 ps. The vertical dashed red lines show the limits of the eight time windows of 500 ps width. The range from 0 to 4 ns was used for the calculation of statistical moments.

phantom parameters (first row in Table 1). Hence, the photon noise level in results of MC simulations matches the one typically observed during *in-vivo* time-resolved measurements with a collection time of 1 s. A collection time of 1 s, which corresponds to the phantom measurement and its noise level, is adequate for monitoring hemodynamic changes in the brain. The number of collected photons, which is proportional to the collection time, has an influence on the photon noise and hence on *CNR*, while relative contrast and depth selectivity are unaffected.

5. Results and discussions

5.1. Measurements and corresponding Monte Carlo simulations

Figure 2(a) shows the measured DTOFs (averaged over 100 s) after accounting for the different time delays in the IRF and phantom measurements as explained in Section 4.2. The full width at half maximum of the measured IRF is 126 ps. The discrepancies between Monte Carlo simulations and measured DTOFs for homogeneous medium are on the level of noise, as can be verified by the weighted residuals calculated using a single DTOF and shown in Fig. 2(b). The weighted residuals for each time channel i were calculated as: $(N_{i,meas} - N_{i,sim})/\sqrt{N_{i,sim}}$, where N_i is the number of photons in individual time channels for measurement and simulation. Only for the calculation of weighted residuals, the measured single DTOF was interpolated in time domain to increase the width of time channels from 4.07 to 10 ps to match the time channels of the simulated DTOF. This simulated DTOF, which corresponds to the homogeneous case for the phantom parameters in Table 1, was rescaled to match the integrated photon count of the homogeneous measurement, $N = 5.2 \times 10^5$, as mentioned in Section 4.3. The same scaling factor was applied to all other simulated DTOFs, which corresponds to a detection system with a fixed sensitivity. Also, the analysis for different values of source detector separation, in Section 5.4, was repeated with $N = 5 \times 10^5$ for each homogeneous measurement, which corresponds to a detection system with a varied sensitivity.

5.2. Results of the various metrics for measured and simulated data

The results of the calculations of different metrics for all measurands are presented in Fig. 3 for the measured TD-NIRS data and for the corresponding MC simulated data. All possible ratios of late and early time windows are presented.
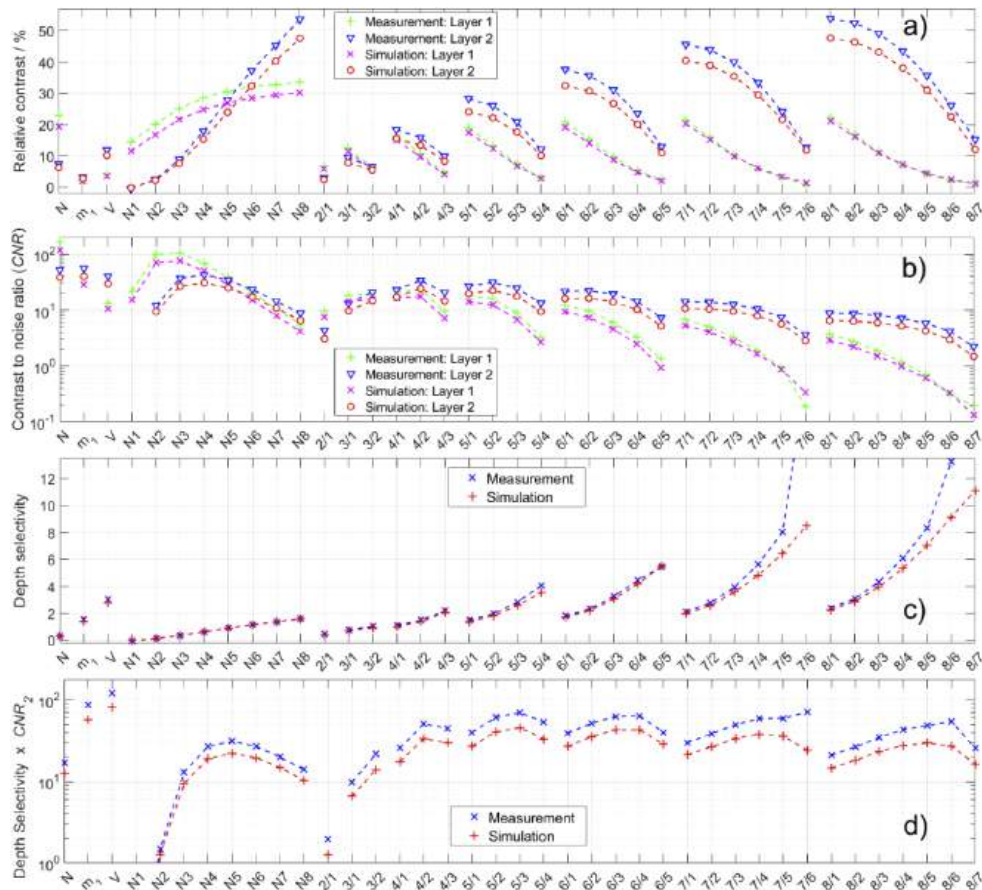
Fig. 3. Results of analysis of the various metrics obtained for moments (N, m_1, V), photon counts in time windows (N_1 to N_8) and their ratios ($N_{2/1}$ to $N_{8/7}$). (a) Relative contrasts caused by 15% absorption changes in superficial and deeper layers separately. (b) Contrast-to-noise ratio (unitless) for each of the two layers. (c) Depth selectivity (unitless). (d) Product (unitless) of contrast-to-noise ratio for the deeper layer and depth selectivity. Simulated data correspond to the parameters listed in the first row in Table 1. Photon noise calculation was based on a total photon count $N = 5.2 \times 10^5$ and using the simulated DTOF for the homogeneous case.

The relative contrasts related to absorption changes in the superficial layer (layer 1) and in the deeper layer (layer 2) are presented in Fig. 3(a). The magnitudes of relative changes in statistical moments are up to 23%, 8% and 11% for the number of photons (N), mean time of (m_1) flight and variance (V). These changes are higher than typically seen in fNIRS measurements, but do not go beyond the linear regime [15]. In agreement with known results [15,36], N has a much higher relative contrast to changes in the superficial layer than in the deeper layer, and on the contrary V has a much higher relative contrast to changes in the deeper layer than in the superficial layer. The early time windows (N_1 and N_2) have significant relative contrast to changes in the superficial layer only, which supports the expectation that the early photons do not penetrate the deeper layer [37]. As a consequence, the results highlight that early time windows are prominent for monitoring changes in the superficial layer. For the later time windows a nearly linear increase in the relative contrast related to the deeper layer with increase of time is observed. Also, a small increase in the relative contrast related to the superficial layer with increase of

time is noted, which highlights that all time windows are highly susceptible to contamination from the superficial layer. The observed trends for the relative contrasts of time windows are in agreement with trends for the time-dependent mean partial pathlengths (TMPP), which is a sensitivity measure for individual time channels introduced by Steinbrink *et al.*, [13]. The ratios of time windows reveal lower relative contrast when changes in absorption appear in either superficial or deeper layers compared to individual time windows, and in particular $N_{7/6}$ and $N_{8/7}$ show almost no relative contrast for a 15% absorption change in the superficial layer. The ratios between early time windows (N_1 to N_4) show a poor relative contrast for the changes located in deeper layer and a similar relative contrast for the absorption changes located in the superficial layer. Hence, later time windows (N_5 and later) are essential for detecting absorption changes located in the deeper layer. The magnitudes of relative contrasts cannot be used to objectively compare different measurands without accounting for their noise, e.g. the low values of relative contrast for m_1.

The contrast-to-noise ratios (Fig. 3(b)) for the two layers allow to quantitatively compare the contrasts with respect to the level of the associated noise for each measurand. For the first time window, the values of contrast and hence CNR_2 are close to zero, which cannot be displayed on the logarithmic graph. The CNR_2 for the statistical moments (N, m_1 and V) are higher than for any time window or ratio of time windows, and the ratios of time windows have lower CNR than single time windows. The limitation of CNR as an overall performance metric is the lack of information about the level of superficial contamination.

Depth selectivity, shown in Fig. 3(c), allows to quantitatively compare the level of superficial contamination for different measurands. Evidently, total number of photons N is highly susceptible to superficial contamination while variance of the DTOF V is less susceptible, which agrees with general knowledge [21,38]. The depth selectivity for time windows has a nearly linear dependence on time. The depth selectivity for V is significantly higher than for any time window, but the highest depth selectivity is achieved by the ratios of the latest time windows. Unfortunately, these ratios could be accurately calculated only using simulated data because of a substantial noise in the measured data.

In this study we propose a new metric to quantitatively rank various measurands with respect to their ability to monitor absorption changes in a deeper layer. The unitless product of CNR_2 and depth selectivity is presented in Fig. 3(d) for all measurands. The result for total number of photons N (16.9 using measured data and 12.5 using simulated data) is similar to the average of the results for all time windows (16.7 using measured data and 12.1 using simulated data), since N is the sum of all time windows. The values for the first two time windows and their ratio ($6.5 \cdot 10^{-3}$, 1.2 and 1.3, respectively, for simulated data) are many times lower than for other measurands, e.g. 31.3 for the 5$^{\text{th}}$ time window, which highlights the especially poor performance of early time windows. The value decreases for later time windows and the 5$^{\text{th}}$ is the optimal time window, which could not be deduced from any of the other metrics alone. The values for ratios of time windows are higher than for time windows, which suggests that ratios are superior for monitoring absorption changes in the deeper layers. The optimal ratio of time windows, which provides the highest value, uses the 5$^{\text{th}}$ and the 3$^{\text{rd}}$ time windows ($N_{5/3}$), although the values obtained for ratios with adjacent time windows are similar. A previous study compared depth selectivity only and showed evidence to prefer ratios of the latest time windows [16], whereas the current results, which incorporate photon noise, suggest that it is not always optimal to use the latest time windows because of the substantially increasing level of noise. The measurands ranked according to their product value from highest to lowest are: variance, mean time of flight, ratios of time windows, time windows, and total photon count.

For all measurands, the values of relative contrast (Fig. 3(a)) for both layers are higher for measured data than for simulated data by up to 20%, depending on the measurand. Therefore, the values of CNR as well as the product involving CNR are also higher for the measured data. This

discrepancy between results of measurements and Monte Carlo simulations can be explained by a number of measurement uncertainties, e.g. mismatch between absorption changes in the physical phantom and the MC model, uncertainty of the thickness of the superficial layer, mismatch between boundary conditions applied in the MC model and physical phantom, as well as the light reflections on the surface of the Mylar film. The differences between results for measured and simulated DTOFs do not change the findings based on the comparison of measurands.

5.3. *Results of the metrics for different parameters of the model*

MC simulations and the analyses were repeated for different values of parameters listed in Table 1: the reduced scattering coefficient ($\mu_s' = 0.5$, 1.0, 1.5 mm^{-1}) for both layers of the model, thickness of the superficial layer ($d = 5$, 10, 15 mm) and source-detector separation ($\rho = 20$, 30, 40 mm). The analyses for these parameters are presented in Fig. 4 for relative contrast (first row), contrast-to-noise ratio for the deeper layer (CNR_2) (second row), depth selectivity (third row), and product of CNR_2 and depth selectivity (fourth row). The results for the nominal values of parameters of the model ($\mu_s' = 1.0$ mm^{-1}, $d = 10$ mm, $\rho = 30$ mm) are similar to the results presented in Fig. 3. The total number of detected photons (N), which is used calculate the photon noise, strongly depends on the values of the models' parameters. N affects the photon noise, which influences CNR and hence the product of CNR_2 and depth selectivity. However, the values of relative contrast and selectivity are independent of N.

An increase in reduced scattering coefficient (μ_s') deteriorates the performance of all measurands as shown by evaluation of all metrics (Figs. 4(a)–4(d)). On the contrary, the relative contrast to absorption changes in the superficial layer increases for all measurands for increasing μ_s'. This effect is consistent with the general knowledge that photons travel more superficially through a medium with an increased μ_s' All measurands are affected similarly by a change in µ'$_s$. However, the overall performance of time windows (Fig. 4(d)) decreases slightly more for the earlier time windows for an increased μ_s'. The optimal choice of time window is the 4th for $\mu_s' = 0.5$ mm^{-1} and the 5th for higher μ_s'.

The thickness of the superficial layer (d) has the most effect on the metrics for all measurands. In particular for the relative contrasts, the probability that photons visit the deeper layer decreases with d, and the behavior is opposite for the probability that photons visit the superficial layer. The values of relative contrast are similar for all time windows for an absorption change in the superficial layer when $d = 5$ mm, which agrees with the previously demonstrated behavior of TMPPs in layers extending up to 4 mm in depth [13]. When $d = 15$ mm the dependence of relative contrast on time is nearly parabolic, which also agrees with the behavior of TMPPs. The optimal time window, based on Fig. 4(h), is N_4 for $d = 5$ mm, N_5 for $d = 10$ mm and N_6 for $d = 15$ mm. An increase in d worsens relatively more the performance of earlier time windows than later time windows. Therefore, later time windows are preferred for thicker d.

The influence of ρ on the measurands is shown in Figs. 4(i)–4(l). An increase in ρ improves the relative contrast for the deeper layer for statistical moments, as expected from previous studies [22], but interestingly it has almost no effect on the relative contrasts for time windows and hence for their ratios, especially for the later time windows. The observations for total number of photons N and time windows closely agree with findings by Del Bianco *et al.*, [39], where the average penetration depth and pathlength travelled in each layer for photons with the same arrival time was found to be independent of ρ (Fig. 4(i)). On the contrary, the continuous wave probability, i.e. N, was strongly dependent on ρ, as in the present work. Assuming N increases for decreasing ρ, which corresponds to a detection system with a fixed sensitivity, then CNR_2 is higher at shorter ρ for all measurands due to smaller photon noise level. With such dependence of N on ρ, for time windows the shortest ρ is preferred, which is confirmed by the product of CNR_2 and depth selectivity. To study the effect of ρ on statistical moments and in more detail on time windows, the next section contains results for a bigger range of ρ and a more thorough
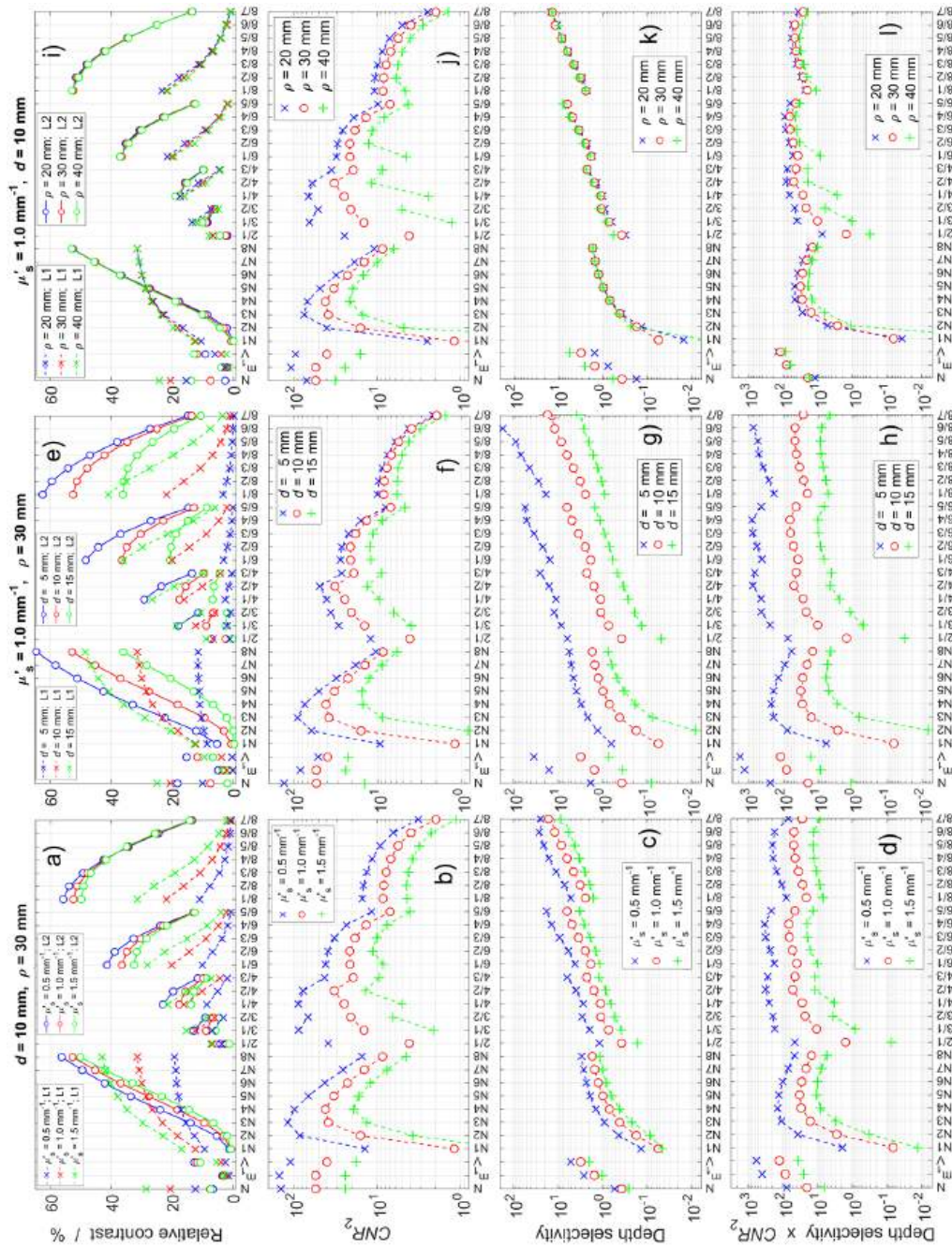
Fig. 4. Quantitative comparison of measurands using relative contrast (first row), contrast-to-noise ratio (second row), depth selectivity (third row) and product of CNR_2 and depth selectivity (fourth row) repeated for different parameters of the model: (a-d) reduced scattering coefficient (μ_s'), (e-h) thickness of superficial layer (d), and (i-l) source-detector separation (ρ). Markers with red circles correspond to the results for the nominal values ($\mu_s' = 1\,\mathrm{mm}^{-1}$, $d = 10\,\mathrm{mm}$, $\rho = 30\,\mathrm{mm}$), which are close to the values used for the comparison in Fig. 3. The ratios with 5th and 7th time windows in the numerator follow the trends of the ratios of other time windows, similar as in Fig. 3, and are not shown for clarity of the data presentation. Notations L1 and L2 in (a, e, i) correspond to Layer 1 and Layer 2, respectively.

analysis of the product of CNR_2 and depth selectivity. The shape of DTOFs strongly depends on the values of μ_s' and ρ. The width of time windows can be adapted to fit the whole range of a DTOF for different values of μ_s' and ρ, but it goes beyond the scope of the present study and therefore the width of time windows was kept constant (500 ps).

The presented metrics show how different parameters of the model affect the performance of measurands. Interestingly, the comparison of the product of CNR_2 and depth selectivity for different measurands has little dependence on the varied parameters of the model, and the order of measurands according to this metric remains the same: V, m_1, ratios of time windows, time windows and N. On the contrary, the varied parameters can differently affect the values of relative contrast, CNR, and depth selectivity for the different considered measurands. The analyses for different models' parameters can help explain the possible causes for discrepancies between measurements and simulations shown in Fig. 3. A change in reduced scattering coefficient or thickness of the superficial layer changes the relative contrasts for the two layers in opposite directions. The large influence of d poses an issue for brain studies using fNIRS as the thickness of extracerebral layer is usually unknown and varies greatly between subjects. The typical thickness of the scalp and skull is around 10 to 14 mm [40,41]. As a consequence of the lack of knowledge of d, the magnitudes of observed contrasts during measurements on different patients cannot be directly compared.

5.4. Depth selectivity vs. contrast-to-noise ratio

A more informative way to analyze the product of CNR_2 and depth selectivity (fourth row in Fig. 4) is to plot CNR_2 versus depth selectivity, which is shown in Fig. 5 for different values of scattering coefficient (μ_s') and thickness of the superficial layer (d). The similar analysis for different values of source-detector distance (ρ) is shown in Fig. 6. The graphs allow to view separately the contributions of CNR_2 and depth selectivity. The information contained in Figs. 3(b)–3(d) is shown in Fig. 5(b) for simulated data and in Fig. 5(e) for measured data.

Variance of the DTOF does not have the highest CNR_2 nor the highest depth selectivity, e.g. Figure 5(d), but its product of CNR_2 and depth selectivity is always the highest out of the considered measurands, which is shown as a dashed red line in all panels in Fig. 5. Mean time of flight (m_1) is the second best measurand. The results obtained using the simulated data (Fig. 5(b)) and using the measured data (Fig. 5(e)) have minor discrepancies. The latest time windows, e.g. N_7 and N_8, contain very few photons (see DTOFs in Fig. 2(a)), and hence the metrics for these windows cannot be precisely calculated from measured data. For real *in vivo* measurements it is likely not feasible to use the latest time windows due to the limited number of photons collected at long times. Acquiring data with longer collection time cannot be a solution when monitoring fast absorption changes, but increasing the detection area or reducing ρ may be considered.

A detailed analysis of the influence of ρ on the ranking metric is shown in Fig. 6. We consider two possible dependencies of total number of photons N on ρ : N changes with ρ according to constant detection sensitivity (Fig. 6(a)), and a fixed value of $N = 5 \times 10^5$ is assumed for all ρ for the homogeneous medium (Fig. 6(b)). Note that depth selectivity is independent of N. In real measurements, the first scenario is unrealistic for low ρ because the detector would over-saturate and the second scenario is unrealistic for high ρ because insufficient photons can reach the detector to obtain an adequate count rate. In practice, in order to detect the late photons at short ρ the detector is made insensitive to the early times by using a gated detection scheme [42]. Depth selectivity for time windows has almost no dependence on ρ, especially for the later time windows, and on the contrary depth selectivity for total number of photons N demonstrates a strong dependence on ρ, as discussed in the previous section and found in Ref. [39].

Interestingly, m_1 and V perform significantly better than time windows and ratios of time windows for all considered values of interoptode distance ρ. The depth selectivity for all three statistical moments increases significantly with ρ, while it remains the same for time windows.

For larger ρ the depth selectivity of m_1 and V is much higher than even for the latest time window. As mentioned previously, the very late time windows are impractical measurands due to low photon counts that can be on the level of noise.

Assuming that total number of photons N depends on ρ, i.e. detection system with fixed sensitivity, then CNR_2 is worsened with increasing ρ for all measurands except N (Fig. 6(a)). On the contrary, if N is independent of ρ, i.e. detection system with varied sensitivity, then CNR_2 is improved with increasing ρ for all measurands (Fig. 6(b)). Using the introduced method for plotting the product of CNR_2 and depth selectivity, the optimal choice of ρ can be easily determined for any measurand. The optimal choice of ρ strongly depends on how N depends on ρ. For the case when N changes with ρ and for an ideal detector that can detect at any count rate, i.e. over-saturation of the detection system is not considered, the optimal ρ for measuring changes in N, m_1 and V are between 30 and 35 mm, at 25 mm, and at 20 mm, respectively (Fig. 6(a)). The most commonly used ρ for NIRS measurements on the human head is 30 mm, which allows to collect sufficient number of photons and avoid oversaturation of detectors. These optimal values of ρ are pertaining for the thickness $d = 10$ mm and they can differ significantly for other
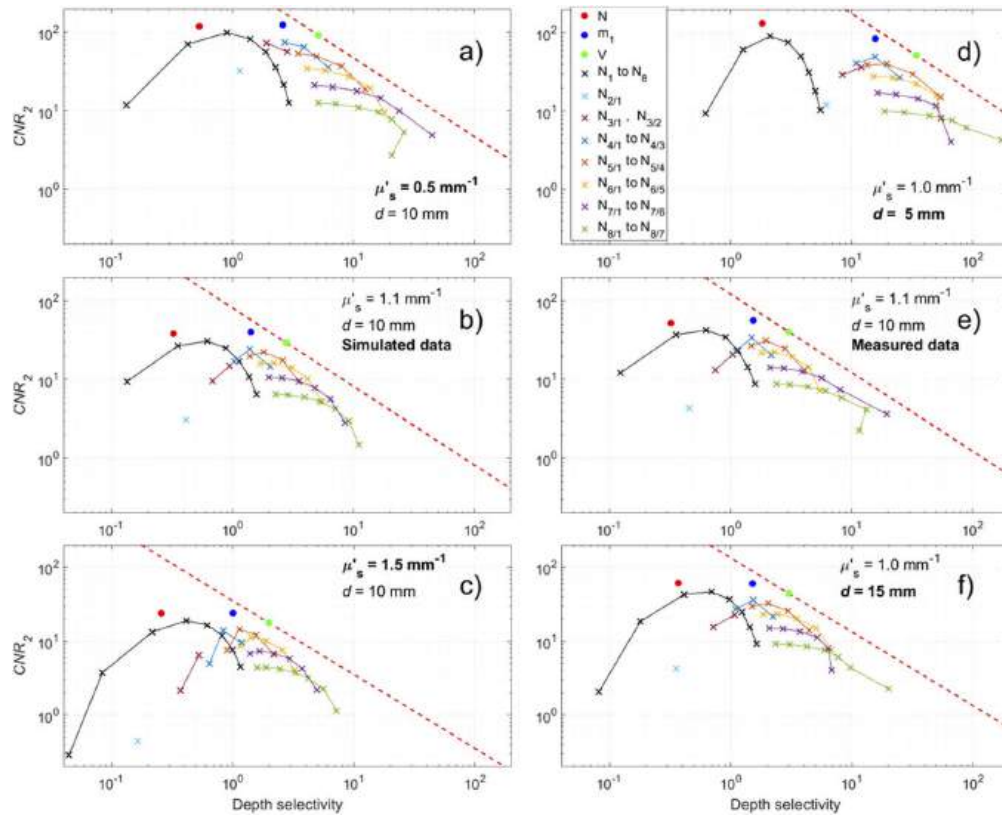

Fig. 5. Contrast-to-noise ratio for the deeper layer CNR_2 plotted against depth selectivity for all considered measurands. The analyses of data obtained by MC simulations were repeated for different values of reduced scattering (μ'_s) (a,b,c), and thickness of superficial layer (d) (d,b,f). The results obtained using simulated data (b) agree with the results obtained using measured data (e). In each panel, the dashed red line shows the value of the product of CNR_2 and depth selectivity for variance of the DTOF. Time windows (N_1 to N_8) and ratios of different time windows ($N_{2/1}$ to $N_{8/7}$) can be distinguished according to their depth selectivity, cf. Figure 3(c) and Figs. 4(c), 4(g), and 4(k).
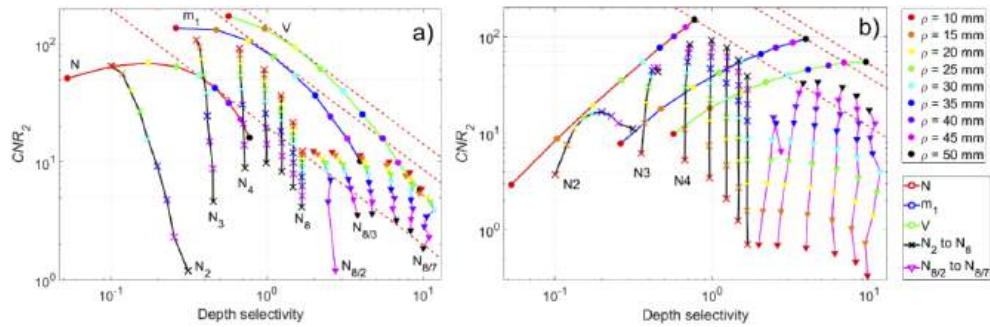
Fig. 6. CNR_2 vs. depth selectivity for various source-detector distances ρ, from 10 mm to 50 mm, and color-coded according to legend. (a) Total number of photons (N) for the homogeneous medium was assumed to change with ρ, which corresponds to measurements with a fixed detection sensitivity. (b) $N = 5 \times 10^5$ was assumed for the homogeneous medium for all values of ρ. Note that depth selectivity (x-axis) is independent of N for all measurands. The dashed red lines show the highest product of CNR_2 and depth selectivity, which correspond to the optimal choice of ρ, for N, m_1 and V. The thickness of the superficial layer was 10 mm. The values of depth selectivity for the 1$^{\text{st}}$ time window (N_1) are close to zero and are not displayed on the logarithmic graph. The ratios with the 8$^{\text{th}}$ time window in the numerator ($N_{8/2}$ to $N_{8/7}$) were chosen for display and for clarity of the data presentation; the results for other ratios have similar dependence on ρ.

values of d, which was not studied. Mean time of flight and especially variance of the DTOF are identified as the best measurands for estimating absorption changes in the deeper layer for all values of ρ between 10 and 50 mm.

6. Discussion

We carried out the quantitative comparison of the performance of measurands calculated from measured and simulated TD-NIRS data: number of photons (N), mean time of flight, variance of DTOF, photon counts in time windows and ratios of photon counts in different time windows. Measurands' ability to monitor absorption changes in the deeper layer were compared using relative contrast, contrast-to-noise ratio (CNR_2) and depth selectivity. The observed trends of measurands agree with the findings of previous studies [16,39]. However, the combination of all metrics is relevant and any single one of them is not sufficient to identify the measurand with the best overall performance. Therefore, we introduced the product of CNR_2 and depth selectivity for ranking measurands. The analyses were repeated for different reduced scattering coefficient, thickness of the superficial layer and source-detector separation (ρ), which also allowed us to determine the optimal choice of ρ for each measurand assuming the two dependencies of total number of collected photons N on ρ.

One of the findings of our study is that variance has the highest value of the product of CNR_2 and depth selectivity for all considered values of parameters of the model and for both assumptions of how N depends on ρ. This finding suggests that it is the best measurand for monitoring absorption changes in the deeper layers, despite the fact that variance does not have the highest value for any of the single evaluated metrics. It should be noted that N has a major influence on the photon noise and CNR, but the qualitative comparison and ranking of measurands is independent of N.

When N is assumed to be independent of ρ, an increase in ρ improves performance for all measurands. When N changes with ρ, the optimal ρ values are between 30 and 35 mm for N,

25 mm for m_1 and 20 mm for V. The shortest ρ is preferred for time windows method due to the highest N, neglecting the possibility of oversaturation.

The influence of IRF can have substantial consequences for measurands based on time windows [16]. However, the experimental IRF that is relevant in the present study has a clean shape with a fast, nearly exponential decay and no after-pulsing background, no slow tail and no afterpeaks. Such shape implicates little influence on the time-window measurands [15,16].

The depth selectivity shows that time windows and their ratios can be sensitive to absorption changes appearing at different depths, which suggests that they contain the most information about absorption changes in different layers. The higher photon noise associated with late time windows is the consequence of using fewer photons in their calculations compared to earlier time windows as well as to statistical moments. The study and optimization of measurands with the aim to retrieve the most information about deep absorption changes have been addressed previously [24]. The new methods for quantitative comparison facilitate further advancements in optimization of measurands.

The current work outlines the methodology for quantitatively comparing different measurands' performances, as available in time-domain, frequency-domain and continuous-wave fNIRS signals analyses, for detecting the absorption changes in the deep tissues, e.g. brain. The methodology was applied to the well-defined two-layered geometry, which is an easy to manipulate and understand analog of a human head [43], to highlight the expected behaviors of measurands as well as to show their ranking in a fully controlled measurement configuration. The adult head is commonly simplified as a homogeneous (or two-layered) model [43]. Therefore, the findings for a two-layered model could be applicable to brain measurements. Methodology as presented in this work can be further expanded by analyses of more realistic tissue composition e.g. to study the effect of cerebrospinal fluid, skull microcirculation, or analyses of influence of layers thicknesses. fNIRS measurements can be carried out on an adult head, or on neonates (who have very different thicknesses of tissue layers compared to adults), or on muscles under a layer of skin and fat. The proposed methodology can be applied to more realistic models (e.g. MRI-based head or thyroid).

7. Conclusions

The concepts used in this work were built upon previous studies [15,16], but were extended to include noise in the assessment of performance and provide an objective metric (CNR_2) for ranking of measurands in terms of their overall performance. The product of CNR_2 and depth selectivity that was applied to various scenarios turned out to yield a valid overall performance measure. It can be included in the future for performance characterization and comparison of NIRS measurands calculated from measured or simulated data in time domain or other domains.

We found that variance always (regardless of photon count noise, scattering coefficient, superficial layer thickness, and source-detector separation) has the highest overall performance compared to other measurands i.e. total number of photons, mean time of flight, time windows, and ratios of time windows.

Disclosures

The authors declare no conflicts of interest.

References

1. F. Lange and I. Tachtsidis, "Clinical Brain Monitoring with Time Domain NIRS: A Review and Future Perspectives," Appl. Sci. **9**(8), 1612 (2019).
2. M. Smith, "Shedding light on the adult brain: a review of the clinical applications of near-infrared spectroscopy," Philos. Trans. R. Soc., A **369**(1955), 4452–4469 (2011).
3. G. Bale, C. Elwell, and I. Tachtsidis, "From Jöbsis to the present day: a review of clinical near-infrared spectroscopy measurements of cerebral cytochrome-c-oxidase," J. Biomed. Opt. **21**(9), 091307 (2016).
4. T. Hamaoka and K. K. McCully, "Review of early development of near-infrared spectroscopy and recent advancement of studies on muscle oxygenation and oxidative metabolism," J. Physiol. Sci. **69**(6), 799–811 (2019).
5. M. Wolf, M. Ferrari, and V. Quaresima, "Progress of near-infrared spectroscopy and topography for brain and muscle clinical applications," J. Biomed. Opt. **12**(6), 062104 (2007).
6. M. A. Yücel, J. J. Selb, T. J. Huppert, M. A. Franceschini, and D. A. Boas, "Functional Near Infrared Spectroscopy: Enabling routine functional brain imaging," Curr. Opin. Biomed. Eng. **4**, 78–86 (2017).
7. M. Ferrari and V. Quaresima, "A brief review on the history of human functional near-infrared spectroscopy (fNIRS) development and fields of application," NeuroImage **63**(2), 921–935 (2012).
8. I. Tachtsidis and F. Scholkmann, "False positives and false negatives in functional near-infrared spectroscopy: issues, challenges, and the way forward," Neurophotonics **3**(3), 031405 (2016).
9. A. Torricelli, D. Contini, A. Pifferi, M. Caffini, R. Re, L. Zucchelli, and L. Spinelli, "Time domain functional NIRS imaging for human brain mapping," NeuroImage **85**(Pt 1), 28–50 (2014).
10. Y. Yamada, H. Suzuki, and Y. Yamashita, "Time-Domain Near-Infrared Spectroscopy and Imaging: A Review," Appl. Sci. **9**(6), 1127 (2019).
11. S. Mosca, P. Lanka, N. Stone, S. Konugolu Venkata Sekar, P. Matousek, G. Valentini, and A. Pifferi, "Optical characterisation of porcine tissues from various organs in the 650–1100 nm range using time-domain diffuse spectroscopy," Biomed. Opt. Express **11**(3), 1697–1706 (2020).
12. A. Puszka, L. Herve, A. Planat-Chretien, A. Koenig, J. Derouard, and J. M. Dinten, "Time-domain reflectance diffuse optical tomography with Mellin-Laplace transform for experimental detection and depth localization of a single absorbing inclusion," Biomed. Opt. Express **4**(4), 569–583 (2013).
13. J. Steinbrink, H. Wabnitz, H. Obrig, A. Villringer, and H. Rinneberg, "Determining changes in NIR absorption using a layered model of the human head," Phys. Med. Biol. **46**(3), 879–896 (2001).
14. C. Sato, M. Shimada, Y. Tanikawa, and Y. Hoshi, "Estimating the absorption coefficient of the bottom layer in four-layered turbid mediums based on the time-domain depth sensitivity of near-infrared light reflectance," J. Biomed. Opt. **18**(9), 097005 (2013).
15. H. Wabnitz, A. Jelzow, M. Mazurenka, O. Steinkellner, R. Macdonald, D. Milej, N. Zolek, M. Kacprzak, P. Sawosz, R. Maniewski, A. Liebert, S. Magazov, J. Hebden, F. Martelli, P. Di Ninni, G. Zaccanti, A. Torricelli, D. Contini, R. Re, L. Zucchelli, L. Spinelli, R. Cubeddu, and A. Pifferi, "Performance assessment of time-domain optical brain imagers, part 2: nEUROPt protocol," J. Biomed. Opt. **19**(8), 086012 (2014).
16. H. Wabnitz, D. Contini, L. Spinelli, A. Torricelli, and A. Liebert, "Depth-selective data analysis for time-domain fNIRS: moments vs. time windows," Biomed. Opt. Express **11**(8), 4224–4243 (2020).
17. A. Liebert, H. Wabnitz, D. Grosenick, M. Moller, R. Macdonald, and H. Rinneberg, "Evaluation of optical properties of highly scattering media by moments of distributions of times of flight of photons," Appl. Opt. **42**(28), 5785–5792 (2003).
18. J. Selb, J. J. Stott, M. A. Franceschini, A. G. Sorensen, and D. A. Boas, "Improved sensitivity to cerebral hemodynamics during brain activation with a time-gated optical system: analytical model and experimental validation," J. Biomed. Opt. **10**(1), 011013 (2005).
19. L. Zucchelli, D. Contini, R. Re, A. Torricelli, and L. Spinelli, "Method for the discrimination of superficial and deep absorption variations by time domain fNIRS," Biomed. Opt. Express **4**(12), 2893–2910 (2013).
20. D. Contini, L. Spinelli, A. Torricelli, A. Pifferi, and R. E. D. C. R. Cubeddu, "Novel method for depth-resolved brain functional imaging by time-domain NIRS," in *Diffuse Optical Imaging of Tissue* (Optical Society of America, 2007), p. 6629_7.
21. A. Liebert, H. Wabnitz, J. Steinbrink, H. Obrig, M. Möller, R. Macdonald, A. Villringer, and H. Rinneberg, "Time-Resolved Multidistance Near-Infrared Spectroscopy of the Adult Head: Intracerebral and Extracerebral Absorption Changes from Moments of Distribution of Times of Flight of Photons," Appl. Opt. **43**(15), 3037–3047 (2004).
22. A. Gerega, D. Milej, W. Weigl, M. Kacprzak, and A. Liebert, "Multiwavelength time-resolved near-infrared spectroscopy of the adult head: Assessment of intracerebral and extracerebral absorption changes," Biomed. Opt. Express **9**(7), 2974 (2018).

23. J. Philip and K. Carlsson, "Theoretical investigation of the signal-to-noise ratio in fluorescence lifetime imaging," J. Opt. Soc. Am. A **20**(2), 368–379 (2003).

24. A. Liebert, H. Wabnitz, and C. Elster, "Determination of absorption changes from moments of distributions of times of flight of photons: optimization of measurement conditions for a two-layered tissue model," J. Biomed. Opt. **17**(5), 057005 (2012).

25. A. Liebert, H. Wabnitz, D. Grosenick, and R. Macdonald, "Fiber dispersion in time domain measurements compromising the accuracy of determination of optical properties of strongly scattering media," J. Biomed. Opt. **8**(3), 512 (2003).

26. L. Spinelli, M. Botwicz, N. Zolek, M. Kacprzak, D. Milej, P. Sawosz, A. Liebert, U. Weigel, T. Durduran, F. Foschum, A. Kienle, F. Baribeau, S. Leclair, J. P. Bouchard, I. Noiseux, P. Gallant, O. Mermut, A. Farina, A. Pifferi, A. Torricelli, R. Cubeddu, H. C. Ho, M. Mazurenka, H. Wabnitz, K. Klauenberg, O. Bodnar, C. Elster, M. Benazech-Lavoue, Y. Berube-Lauziere, F. Lesage, D. Khoptyar, A. A. Subash, S. Andersson-Engels, P. Di Ninni, F. Martelli, and G. Zaccanti, "Determination of reference values for optical properties of liquid phantoms based on Intralipid and India ink," Biomed. Opt. Express **5**(7), 2037–2053 (2014).

27. F. Martelli, P. Ninni, G. Zaccanti, D. Contini, L. Spinelli, A. Torricelli, R. Phd, H. Wabnitz, M. Mazurenka, R. Macdonald, A. Sassaroli, and A. Pifferi, "Phantoms for diffuse optical imaging based on totally absorbing objects, part 2: Experimental implementation," J. Biomed. Opt. **19**(7), 076011 (2014).

28. B. H. GmbH, "The bh TCSPC Handbook," User Handbook, 8th edition, www.becker-hickl.com (2019).

29. D. Contini, A. Torricelli, A. Pifferi, L. Spinelli, F. Paglia, and R. Cubeddu, "Multi-channel time-resolved system for functional near infrared spectroscopy," Opt. Express **14**(12), 5418–5432 (2006).

30. R. Re, D. Contini, M. Caffini, L. Spinelli, and A. Torricelli, "A compact time-resolved system for near infrared spectroscopy based on wavelength space multiplexing," Rev. Sci. Instrum. **81**(11), 113101 (2010).

31. S. Wojtkiewicz and A. Liebert, "Parallel, multipurpose Monte Carlo code for simulation of light propagation in segmented tissues," Manuscript submitted for publication (2020).

32. A. Liebert, H. Wabnitz, N. Zolek, and R. Macdonald, "Monte Carlo algorithm for efficient simulation of time-resolved fluorescence in layered turbid media," Opt. Express **16**(17), 13188–13202 (2008).

33. M. Doulgerakis, A. Eggebrecht, and H. Dehghani, "High-density functional diffuse optical tomography based on frequency-domain measurements improves image quality and spatial resolution," Neurophotonics **6**(03), 1 (2019).

34. M. S. Patterson, B. Chance, and B. C. Wilson, "Time resolved reflectance and transmittance for the noninvasive measurement of tissue optical properties," Appl. Opt. **28**(12), 2331–2336 (1989).

35. H. Dehghani, M. E. Eames, P. K. Yalavarthy, S. C. Davis, S. Srinivasan, C. M. Carpenter, B. W. Pogue, and K. D. Paulsen, "Near infrared optical tomography using NIRFAST: Algorithm for numerical model and image reconstruction," Commun. Numer. Meth. Eng. **25**(6), 711–732 (2009).

36. A. Gerega, D. Milej, W. Weigl, N. Zolek, P. Sawosz, R. Maniewski, and A. Liebert, "Multi-wavelength time-resolved measurements of diffuse reflectance: phantom study with dynamic inflow of ICG," in *Biomedical Optics and 3-D Imaging* (Optical Society of America, 2012), p. JM3A.31.

37. A. Pifferi, D. Contini, A. Dalla Mora, A. Farina, L. Spinelli, and A. Torricelli, "New frontiers in time-domain diffuse optics, a review," J. Biomed. Opt. **21**(9), 091310 (2016).

38. H. Wabnitz, M. Moeller, A. Liebert, H. Obrig, J. Steinbrink, and R. Macdonald, "Time-resolved near-infrared spectroscopy and imaging of the adult human brain," Adv. Exp. Med. Biol. **662**, 143–148 (2010).

39. S. Del Bianco, F. Martelli, and G. Zaccanti, "Penetration depth of light re-emitted by a diffusive medium: Theoretical and experimental investigation," Phys. Med. Biol. **47**(23), 4131–4144 (2002).

40. P. Sawosz, S. Wojtkiewicz, M. Kacprzak, W. Weigl, A. Borowska-Solonynko, P. Krajewski, K. Bejm, D. Milej, B. Ciszek, R. Maniewski, and A. Liebert, "Human skull translucency: Post mortem studies," Biomed. Opt. Express **7**(12), 5010–5020 (2016).

41. J. D. Veesa and H. Dehghani, "Hyper-spectral Recovery of Cerebral and Extra-Cerebral Tissue Properties Using Continuous Wave Near-Infrared Spectroscopic Data," Appl. Sci. **9**(14), 2836 (2019).

42. L. Di Sieno, H. Wabnitz, A. Pifferi, M. Mazurenka, Y. Hoshi, A. Dalla Mora, D. Contini, G. Boso, W. Becker, F. Martelli, A. Tosi, and R. Macdonald, "Characterization of a time-resolved non-contact scanning diffuse optical imaging system exploiting fast-gated single-photon avalanche diode detection," Rev. Sci. Instrum. **87**(3), 035118 (2016).

43. J. Selb, T. M. Ogden, J. Dubb, Q. Fang, and D. A. Boas, "Comparison of a layered slab and an atlas head model for Monte Carlo fitting of time-domain near-infrared spectroscopy data of the adult head," J. Biomed. Opt. **19**(1), 016010 (2014).

Check for updates

Time-domain NIRS system based on supercontinuum light source and multi-wavelength detection: validation for tissue oxygenation studies

ALEH SUDAKOU,[1,*] FRÉDÉRIC LANGE,[2] HELENE ISLER,[3] PRANAV LANKA,[4] STANISLAW WOJTKIEWICZ,[1] PIOTR SAWOSZ,[1] DANIEL OSTOJIC,[3] MARTIN WOLF,[3] ANTONIO PIFFERI,[4] ILIAS TACHTSIDIS,[2] ADAM LIEBERT,[1] AND ANNA GEREGA[1]

[1]*Nalecz Institute of Biocybernetics and Biomedical Engineering, Warsaw, Poland*
[2]*Department of Medical Physics and Biomedical Engineering, University College London, London, UK*
[3]*Department of Neonatology, University Hospital Zurich, University of Zurich, Zurich, Switzerland*
[4]*Dipartimento di Fisica, Politecnico di Milano, Milano, Italy*
[*]asudakou@ibib.waw.pl

Abstract: We present and validate a multi-wavelength time-domain near-infrared spectroscopy (TD-NIRS) system that avoids switching wavelengths and instead exploits the full capability of a supercontinuum light source by emitting and acquiring signals for the whole chosen range of wavelengths. The system was designed for muscle and brain oxygenation monitoring in a clinical environment. A pulsed supercontinuum laser emits broadband light and each of two detection modules acquires the distributions of times of flight of photons (DTOFs) for 16 spectral channels (used width 12.5 nm / channel), providing a total of 32 DTOFs at up to 3 Hz. Two emitting fibers and two detection fiber bundles allow simultaneous measurements at two positions on the tissue or at two source-detector separations. Three established protocols (BIP, MEDPHOT, and nEUROPt) were used to quantitatively assess the system's performance, including linearity, coupling, accuracy, and depth sensitivity. Measurements were performed on 32 homogeneous phantoms and two inhomogeneous phantoms (solid and liquid). Furthermore, measurements on two blood-lipid phantoms with a varied amount of blood and Intralipid provide the strongest validation for accurate tissue oximetry. The retrieved hemoglobin concentrations and oxygen saturation match well with the reference values that were obtained using a commercially available NIRS system (OxiplexTS) and a blood gas analyzer (ABL90 FLEX), except a discrepancy occurs for the lowest amount of Intralipid. *In-vivo* measurements on the forearm of three healthy volunteers during arterial (250 mmHg) and venous (60 mmHg) cuff occlusions provide an example of tissue monitoring during the expected hemodynamic changes that follow previously well-described physiologies. All results, including quantitative parameters, can be compared to other systems that report similar tests. Overall, the presented TD-NIRS system has an exemplary performance evaluated with state-of-the-art performance assessment methods.

1. Introduction

Time-domain near-infrared spectroscopy (TD-NIRS) uses short pulses of light to non-invasively and in real-time monitor tissue optical properties, i.e. absorption (μ_a) and reduced scattering (μ'_s) coefficients, which are related to the concentrations of chromophores in tissue, e.g. oxyhemoglobin

(HbO$_2$) and deoxyhemoglobin (Hb). TD systems acquire the highest amount of information, for a defined number of source-detector pairs, compared to continuous-wave and frequency-domain acquisition modes [1]. The monitored parameters, e.g. cerebral metabolism [2] (related to changes of chromophores concentrations) or tissue oxygenation [3] (related to absolute values), help diagnose physiological conditions and monitor results of clinical interventions. NIRS is safe and non-ionizing, which makes it suitable for studies on neonates [4–6] and on adults [7].

A number of recent publications review instrumental developments for various applications of NIRS, including the past and the current status of TD-NIRS [8], clinical brain monitoring with TD-NIRS [1], metabolic brain measurements on neonates [9], neuromonitoring for neonatal encephalopathy [10], functional NIRS [7], instrumentation for functional NIRS [11], and applications related to stroke patients [12], studies on muscles [3], and evaluating the level of consciousness typically after a brain injury [13]. Continuous advancements in optical technologies and electronics for TD systems are leading to better measurements and a wider range of applications. The advancements have enabled TD-NIRS measurements at larger source-detector separations, e.g. 9 cm [14], at longer wavelengths, e.g. in the range from 600 to 1350 nm [15], with more sources and detectors, e.g. 16 sources and 8 detectors with fibers [16], or 1032 detectors [17], or 36288 detectors [18], with fast acquisitions, e.g. wavelength switching at 160 Hz [19], more compact, e.g. $200 \times 160 \times 50$ mm^3 [20], wearable [22,21] and also wireless [23], or with an improved light harvesting capability that allows collecting more photons than restricted by the pile-up limit [24]. Another direction of advancements involves integrating various imaging techniques, e.g. TD-NIRS and diffuse correlation spectroscopy [25,26].

Measurements at more wavelengths allow estimating absolute concentrations of more chromophores, e.g. lipid, water, and collagen [15], in addition to HbO$_2$ and Hb. Furthermore, to follow dynamic changes associated with physiology requires fast acquisitions on a time scale of typically 1 s. Of particular interest is monitoring concentration changes of cytochrome-c-oxidase (CCO) enzyme, which requires many wavelengths as well as fast acquisitions [2]. The importance of monitoring changes in CCO, which relates to tissue metabolism, and the relevant advances in optical technologies were reviewed in [9]. Recently, Lange *et al.* [19] presented an assessment study of a multi-wavelength TD-NIRS system that was designed for monitoring changes in CCO in addition to HbO$_2$ and Hb. The system uses a broadband light source coupled with two acousto-optic tunable filters that allow switching between many different wavelengths. Other common approaches for multi-wavelength TD-NIRS are time multiplexing [27] and space multiplexing [16]. In the first approach, multiple pulsed lasers with different wavelengths are shined in parallel and the optical pulses of different lasers are delayed relative to each other such that they arrive with different time offsets to a single TCSPC card and get recorded in the same TAC, which allows a limited number of wavelengths, typically two. In the second approach, multiple pulsed lasers are sequentially shined using an optical switch, which allows employing many wavelengths at the cost of acquisition time. Renna *et al.* [27] presented such system with 8 pulsed diode lasers, but recommend sequential scanning of no more than 2 or 3 wavelengths for monitoring dynamic processes.

In the present work, the multi-wavelength TD-NIRS system avoids switching wavelengths. The principle of this kind of instrument was introduced in [28]; the presented system is an advanced version and with modern electronics. We report the most relevant performance tests from three established protocols for photon migration instruments (MEDPHOT [29], BIP [30], and nEUROPt [31]), which were intended for quantitatively assessing the performance of time-domain instruments that use pulsed laser sources, single-photon detectors, and time-correlated single-photon counting electronics. Measurements on 32 homogeneous phantoms and a solid inhomogeneous phantom [32] were carried out as part of the BitMap campaign [33], which is a multi-laboratory effort to standardize the performance assessment of instruments for diffuse optics. Furthermore, the ability to estimate absolute concentrations of HbO$_2$ and Hb, and

hence oxygen saturation, is assessed on a series of blood-lipid phantom measurements using the phantom and the protocol developed by Kleiser *et al.* [34,35]. Lastly, *in-vivo* monitoring during hemodynamic changes is demonstrated using measurements on the forearm of three healthy volunteers during arterial and venous cuff occlusions. This study is intended to quantify the capabilities of the system and support its clinical use for diverse applications.

2. System description

2.1. Overview

The system measures the distributions of times of flight of photons (DTOFs) in parallel for 16 wavelengths with a sampling time of 0.3 s. Two emission fibers allow delivering light at two locations. Two detection fibre bundles allow measuring at up to two source-detector distances (ρ). Therefore, the system provides 32 DTOFs (16 wavelengths and 2 detection modules) at a sampling rate of up to 3 Hz. A previous version of the system was used for hemodynamic studies involving the injection of an optical contrast agent Indocyanine Green [36,37]. The system was designed for the clinical environment with the possibility to continuously monitor patients before, during, and after surgery. The current fiber holder design is suitable for adults and can be potentially adjusted for neonates.

2.2. Housing setup

A photo of the arrangement of the system is shown in Fig. 1 (a) and a schematic diagram of the inner components is shown in Fig. 1 (b). All components were mounted inside a 19-inch metal rack case with four wheels, which is a commonly used housing setup for TD-NIRS systems because it is compact, portable, and robust [19,38]. An uninterruptible power supply unit (APC Smart UPS SMC1500I-2U) protects against interruption of external power supply and also allows the system to operate without an external power supply for a brief period.
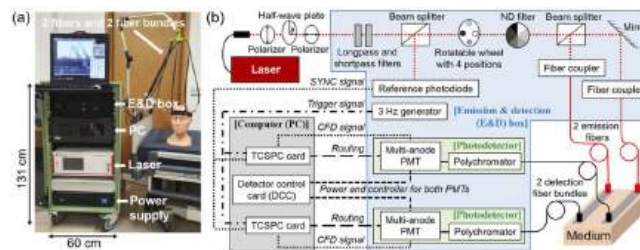
Fig. 1. (a) Photo of the system. (b) Schematic diagram of the components' layout. The acronyms are: emission and detection (E&D) box, neutral density (ND) filter, multi-anode photomultiplier tube (PMT), and time-correlated single-photon counting (TCSPC) card.

2.3. Emission module

The results in this study were obtained with fiber laser SC480-8 WhiteLase (Fianium, UK), which operates at 80 MHz repetition frequency. The fundamental pulse width is 6 ps, the maximum output power is up to 8 W, and the spectral bandwidth range is from 460 to 2000nm.

(1) The output beam of the laser first passes through a system of two polarizers with a half-wave plate in-between, which serves as a variable attenuator for unpolarized light. For a chosen output power of the laser, the half-wave plate is manually rotated and then secured with a screw, such that the power of light exiting any of the two emission fibers is always lower than 20 mW, which equates to a power density of less than 2 mW/mm^2 on the surface of

the skin due to angular spread and distance, which is in line with the safety regulations for measurements on patients. Next, the beam passes through two edgepass filters, which remove the wavelengths that are outside of a desired spectral range. The current chosen spectral range is from 650 to 850 nm, which is achieved with a longpass filter (FEL0650 with a cut-on wavelength of 650 nm, Thorlabs, Sweden) and a shortpass filter (FES0850 with a cut-off wavelength of 850 nm, Thorlabs, Sweden). The two filters allow some unwanted light above 1200 nm to be emitted, but this light does not pass through the polychromator on the detection side.

(2) A beam splitter directs a fraction of the laser light to a reference photodiode (PHD 400, Becker & Hickl GmbH, Germany), which feeds a signal into the SYNC input of each TCSPC card. The details of using reference photodiodes can be found in the TCSPC handbook, pages 76 and 202 [39].

(3) The rest of the light passes through one of four openings in a rotatable wheel: i) an unimpeded opening that lets all light pass through, ii) a solid wall that blocks all light, iii) a band-pass filter centered around 780 nm (FL780-10, Thorlabs), which is used to calibrate diffraction gratings of the two polychromators, and iv) a bandpass interference filter (750 nm with FWHM of 50 nm, Edmund Optics), which is used for the excitation of the ICG in the fluorescence mode measurements.

(4) Final filtering is achieved with the use of a continuously variable neutral density filter (NDC-50C-2-B, Thorlabs), which removes a variable amount of excessive light power.

(5) A beam splitter directs the filtered light into two fiber couplers that guide the light into two optical fibers, which deliver the light to the surface of a medium, e.g. tissue or phantom, at two chosen locations. The parameters of each emission fiber are: step index, 0.39 NA, 2 m length, and 400 μm diameter (FT400EMT, Thorlabs).

2.4. Detection module

After travelling through a diffusive medium, the remitted light is collected by two separate detection fiber bundles (2 m length, 0.22 NA, and a 90° bent tip on the patient side with a 30 mm long-term bending radius, custom-made, Ceram Optec), which are terminated with a circular tip (diameter 3.6 mm) on the medium side and a line-shaped tip (1.4×7.3 mm) that fits into the slit of a polychromator; illustrated in the TCSPC handbook, page 171 [39].

Each fiber bundle guides light to one of the two separate detection modules (PML Spec, Becker & Hickl GmbH, Germany). Each detection module is comprised of two parts: a polychromator (MS125, Oriel Instruments, USA), which has 0.135 NA and uses 77414 diffraction grating (Grating Groove Density is 600 lines / mm), and a multi-anode photomultiplier tube detector (PML-16-1-C, Becker & Hickl GmbH, Germany). The power to both photomultiplier tubes is provided by a detector control card (DCC-100, Becker & Hickl GmbH, Germany), which also allows controlling gain parameters and overload shutdown. The width of each spectral channel is about 12.5 nm, which can be changed by using another diffraction grating, e.g. 35, 18, 9, or 4.5 nm as in [28]. The spectral range, which is a parameter of a polychromator, was set from 674 to 874 nm. Consequently, the central wavelengths of spectral channels were: 680, 692.5, 705, 717.5, 730, 742.5, 755, 767.5, 780.5, 792.5, 805, 817.5, 830, 842.5, 855, and 867.5 nm. For a further description of the detection module, we refer to the instrumentation section in the previous version of the system [36].

The output electrical signals of two PML-16-1-C are passed to two 16-channel TCSPC cards (SPC 150, Becker & Hickl GmbH, Germany). The synchronization between the acquisitions of the two TCSPC cards was achieved using the PCI Express I/O card (PCIe-6321, National Instruments), which was configured with LabView software (National Instruments). The card

generates a trigger signal at 3 Hz for the start of the recording of the DTOF. The two TCSPC cards were used in continuous flow mode with a collection time of 0.3 s. During data analyses, the collection time can be increased by summing consecutive measured DTOFs. The parameters of a TCSPC card were configured such that each DTOF contained 1024 time bins with about 9.77 ps width each. For typical measurements, a temporal resolution of a recorded DTOF must be on the order of 10 ps to quantify the optical properties of diffuse media with accuracy better than 5% using a curve fitting method [40].

2.5. Software

All components were operated using the software provided by the manufacturers and run on a PC with Windows 7 Professional. The laser functions were controlled using the Fianium Laser Controller software. The DCC card and the two TCSPC cards were operated using the TCSPC Package 6.5.0 software (Becker & Hickl GmbH, Germany), which allows to adjust all TCSPC-related parameters, record the data, and assess the quality of the data before, during, and after a measurement. All data were saved and later processed offline using custom codes written in MatLab R2020b.

2.6. Optode holder

The two emission fibers and the two detection fiber bundles can be attached to the surface using custom 3D printed optode holders with holes at desired ρ (typically a few cm apart). The chosen printing materials were pure black ABS filament (Zortrax) for phantom measurements and black Fiberflex 40D filament (Fiberlogy) for *in-vivo* measurements, which is a more flexible material and achieves better contact with the skin. For phantom measurements, the optode holder was held in place using a support stand and covered with tape. For *in-vivo* measurements, the optode holder was fixed in place using Velcro strips and covered with a cohesive bandage.

3. Methods: measurements and data analysis

3.1. BIP protocol

The basic instrument protocol (BIP) [30] allows the assessment of parameters that are related to the hardware components of a time-domain instrument. In particular, we report the instrument response function (IRF), the differential nonlinearity (DNL), the warm-up, and the temporal fluctuations.

To measure the IRF [41], an emission fiber was aligned with a detection fiber bundle at a distance of 6 cm with a neutral density filter between them and two pieces of white paper covering the fiber and the fiber bundle. The DNL was assessed by recording the response to a battery-operated light-emitting diode, which produced a continuous light signal. Repeated measurements were summed to obtain more than 10^5 photon counts per time bin for a good signal-to-noise ratio. The deviation in the number of photons detected in different time bins was quantified by calculating the peak-to-peak difference normalized to the mean value (ε_{DNL}) [30]. To assess the warm-up, the IRF was repeatedly acquired for up to 6 hours. Afterward, to assess the temporal fluctuations, the DTOF was repeatedly acquired on a homogeneous solid phantom (label B2 in the MEDPHOT protocol) at $\rho = 3$ cm. The first three statistical moments, i.e. the total number of photons (N), the mean time of flight (m_1), and the variance (V) [31], were calculated after background subtraction and using time bins that have photon counts higher than 1% of the maximum. Each DTOF contained about 10^6 photons, which was achieved by integrating repeated acquisitions. The temporal fluctuations of the moments were assessed using the standard deviation of 100 values.

3.2.   MEDPHOT protocol

The MEDPHOT protocol [29] allows the assessment of a system's capability to recover μ_a and μ'_s in terms of linearity, coupling, and accuracy. The protocol includes measuring on 32 solid homogeneous phantoms that are labeled with a letter and a number. The phantoms make up all combinations of four nominal μ'_s values and eight nominal μ_a values (see the caption of Fig. 3). The base component of these phantoms is epoxy resin and we assumed the refractive index as 1.55. A measurement on each phantom was acquired for 30 s.

Four scatter plots were obtained: the measured μ_a (or μ'_s) versus the nominal μ_a (or μ'_s) and the measured μ_a (or μ'_s) versus the nominal μ'_s (or μ_a). Using the first two plots, the mean deviation in μ_a (or μ'_s) from linearity was quantified by fitting a straight line and calculating the mean percentage difference between the measured data and the fitted line. This calculation does not use the values of nominal optical properties. Using the other two plots, the coupling of $\Delta\mu_a$ to $\Delta\mu'_s$ (or $\Delta\mu'_s$ to $\Delta\mu_a$) was quantified by fitting a straight line and calculating the slope, which requires using the changes of nominal values (assumed 0.05 cm^{-1} for $\Delta\mu_a$ and 5 cm^{-1} for $\Delta\mu'_s$).

The nominal values of μ_a and μ'_s of the 32 phantoms do not match the true values, and there is no established consensus yet on the agreed true values, as pointed out in [24]. Also, μ_a and μ'_s depend on wavelength, especially μ'_s [27]. Therefore, to assess the accuracy, we present the obtained spectra of μ_a and μ'_s for three well-characterized phantoms: phantom B2, the solid inhomogeneous phantom, and the 1% aqueous solution of Intralipid (the two inhomogeneous phantoms are presented in the next section). The obtained values can be compared to the reported results of other systems that measured on the same phantoms at multiple wavelengths.

3.3.   nEUROPt protocol

The nEUROPt protocol [31] allows the assessment of a system's sensitivity to a small localized μ_a perturbation positioned at various depths and later positions. Measurements were repeated on two inhomogeneous phantoms (solid and liquid) that had similar μ'_s but different μ_a. Monte Carlo simulations were performed for a qualitative comparison.

The mechanically switchable solid inhomogeneous phantom was described in detail in [32]. The phantom has a cavity (diameter 14 mm) for a movable cylindrical rod that has a localized cylindrical μ_a perturbation (we used the rod with the following perturbation: 5 mm in diameter and length, i.e. 98 mm^3 volume, and $\Delta\mu_a$ equivalent to 0.017 cm^{-1}). The rod can be precisely moved by a step motor.

The liquid phantom was a 1% aqueous solution of Intralipid (Fresenius Kabi AG, Bad Homburg, Germany) poured inside a dedicated cell [42]. A localized μ_a perturbation was introduced using a submerged small black PVC cylinder (4 mm in diameter and length, i.e. 50 mm^3 volume), which was fixed to an end of a 0.5 mm thin, rigid, white metallic wire, which was verified to have a negligible effect on TD-NIRS measurements [42]. The depth and the lateral position of the metallic wire can be manually changed with a precision of about 1 mm.

The reported optical properties of the two phantoms without a perturbation are: μ_a ~0.1 cm^{-1} (~0.026 cm^{-1}) and μ'_s ~8 cm^{-1} (~10.5 cm^{-1}) at 800 nm for the solid [32] (liquid [19,43]). The solid phantom mimics the typical μ_a and μ'_s of biological tissue. The liquid phantom, which contained only water and Intralipid and hence can be easily replicated, is used for a comparison with the results on the solid phantom. The refractive index was assumed as 1.55 for the solid and 1.33 for the liquid.

One emission fiber and one detection fiber bundle were fixed at $\rho = 3$ cm. Their positions on the solid phantom were illustrated in [32,38]. When varying the depth, a perturbation was positioned in the midplane between the emitter and the detector, and it was moved in steps of 1 mm (2.5 mm) in the solid (liquid). When varying the lateral position, a perturbation was 1.5 cm (1.2 cm) below the surface and it was moved in steps of 2 mm (2 mm) in the solid (liquid).

The position of a perturbation was defined as the center of a perturbation, as in [31,32]. A measurement was acquired at each position of a perturbation for 60 s (18 s) on the solid (liquid).

The contrasts that result from introducing a perturbation were calculated for five measurands: N, m_1, V, and the number of photons in early and late time windows (from 0.5 to 1 ns for N_{Eearly} and from 3 to 4 ns for N_{Late}). The zero time (0 ps) was defined at the maximum of the IRF. Measurands were calculated from DTOFs after background subtraction and using time bins that have photon counts $\geq 0.1\%$ (2%) of the maximum for measurements on the solid (liquid) phantom. The contrasts were calculated as:

$$\Delta A_{TW}(x) = -\ln(N_{TW}(x)/N_{TW,0}), \tag{1}$$

$$\Delta m_1(x) = m_{1,0} - m_1(x), \tag{2}$$

$$\Delta V(x) = V_0 - V(x), \tag{3}$$

where $\Delta A_{TW}(x)$ is the change in the attenuation for a time window TW (N, N_{Early}, and N_{Late}) due to a perturbation located at x, which is either the depth or the lateral position. The zero subscript represents the reference measure when a perturbation was furthest away from the emitter and the detector.

Monte Carlo (MC) simulations were performed to obtain the sensitivity factors for the first three statistical moments: the mean partial pathlength (*MPP*), the mean time of flight sensitivity factor (*MTSF*), and the variance sensitivity factor (*VSF*). The MC code was developed by Wojtkiewicz *et al.* [44]. The sensitivity factors relate changes in moments to localized changes in μ_a ($MPP = \Delta A / \Delta\mu_a$, $MTSF = \Delta m_1 / \Delta\mu_a$, and $VSF = \Delta V / \Delta\mu_a$) at different depths and lateral positions, and hence they can be used for a comparison with the measured contrasts. For a detailed description of the sensitivity factors and their use, we refer to [44,45]. The MC parameters were chosen as in [46]. The model parameters were set to mimic the solid and the liquid inhomogeneous phantoms, using their optical properties obtained at 805 nm (values listed in Table 2).

3.4. Blood-lipid phantoms

Blood-lipid phantoms allow the assessment of a system's capability to retrieve absolute concentrations of HbO_2 and Hb, and hence total hemoglobin ($HbT = HbO_2 + Hb$) and oxygen saturation ($StO_2 = HbO_2 / HbT$), during controlled dynamic StO_2 changes.

The presented system was transported to University Hospital Zurich, University of Zurich, in Switzerland, to perform measurements on their blood-lipid phantom in parallel with a commercially available oximeter (OxiplexTSTM, frequency-domain, 692 and 834 nm, ISS, Champaign, Illinois, USA). OxiplexTS provides the absolute values of μ_a and μ'_s at two wavelengths, the concentrations of HbO_2, Hb, and HbT, and StO_2. A rigid sensor with four source-detector separations (2.5, 3.0, 3.5, and 4.0 cm) was used and the sampling rate was set to 1 s. Co-oximetry was used as another reference measure of HbT, by analyzing blood samples from the erythrocyte bag using a blood gas analyzer (ABL90 FLEX, Radiometer Medical ApS, Brønshøj, Denmark) and calculating the degree of dilution in the phantom, which is the same method as used in [47].

A detailed description of the phantom can be found in [34,35] and the following is a brief overview. The phantom and a similar protocol were used in previous studies that also used OxiplexTS [48–50]. The phantom consisted of a black 3D printed cubic container with windows on four sides, which allows simultaneously measuring with up to four systems. The windows were made from silicone and had tailored properties to mimic a layer of fat: $\mu_a = 0.063\,\text{cm}^{-1}$, $\mu'_s = 6\,\text{cm}^{-1}$ at 690 nm, and 1 mm thickness. The three main components that made up the liquid were: 2.5 L of phosphate-buffered saline (PBS, after Kreis, pH = 7.4, Kantonsapotheke Zurich, Zurich, Switzerland), a varying amount of Intralipid (Fresenius Kabi AG, Bad Homburg, Germany), and a varying amount of human blood from a human erythrocyte concentrate bag.

Fresh baker's yeast (3.0 g) was added to deoxygenate the phantom ($StO_2 = 0\%$) and the rate was increased by adding glucose 50% (AlleMan Pharma GmbH, Reutlingen, Germany). Blood was fully oxygenated ($StO_2 = 100\%$) by bubbling oxygen gas from an oxygen tank (typically for 1 min). Sodium bicarbonate buffer was added to keep the *pH* level close to 7.4. The temperature (37°C) and the mixing speed (500 rpm) were controlled with a hotplate that has a magnetic stirrer.

Measurements were repeated on two blood-lipid phantoms in which either blood or Intralipid was added at the end of each deoxygenation cycle before bubbling oxygen, i.e. when $StO_2 = 0\%$, similar as in [50]. The first phantom contained 74 ml of Intralipid and four amounts of blood: 20, 35, 55, and 70 ml. The second phantom contained 45 ml of blood and five amounts of Intralipid: 25, 50, 75, 100, and 125 ml. The refractive index was assumed as 1.33. The optical properties resulting from 74 ml of Intralipid and 45 ml of blood mixed with 2.5 L of saline are close to the typical optical properties of a neonatal brain ($\mu'_s \approx 5.5\,\mathrm{cm}^{-1}$) [34].

3.5. In-vivo measurements

In-vivo measurements during cuff occlusions were performed to provide an example of a system's ability to monitor hemodynamic responses in tissue. It is an easy-to-repeat test that allows checking the performance of oximeters *in-vivo* [51]. Measurements were repeated on three healthy volunteers: skinfold thickness (2.1, 2.4, and 2.5 mm), age (25, 26, and 29 years), one male. The measured blood pressure before the start of the experiment was around 120/80 mmHg. Written informed consent was filled in by participants.

A subject was relaxed in a Fowler's position on a medical bed. A probe holder was attached on the posterior side of the left forearm, over the extensor muscles about midpoint between elbow and wrist. An arm-intended pneumatic cuff was loosely placed around the upper arm and rapid inflation was achieved with an electro-pneumatic regulator (SMC ITV2010-31F2N3). The inflation time was a few seconds; the recommended upper limit for a calf muscle was is 6 s [52]. 250 mmHg pressure was applied to occlude arterial and venous flow [25,38,53,54], and 60 mmHg pressure was applied to partially restrict venous flow without obstructing arterial flow [52,55]. The pressure was applied for 2 min. The refractive index of tissue was assumed as 1.4 [56].

3.6. TD-NIRS data analysis

Most measurements were performed with two detection modules at two source-detector distances ($\rho = 2$ and 3 cm, or 3 and 4 cm) away from the same emission fiber. The acquisition time was 0.3 s and the sampling rate was 3 Hz. During post-processing, 3 consecutive DTOFs were summed to increase the signal-to-noise ratio, resulting in a sampling rate of 1 s.

μ_a and μ'_s were estimated using the curve fitting method [57,58] as implemented in NIRFAST software [59]. It is considered a gold standard method to determine the absolute optical properties. A homogeneous semi-infinite medium model under extrapolated boundary conditions was used. The fitting region of the DTOFs was limited based on the percentage of its maximum, i.e. from 85% on the rising edge to 1% on the tail for phantom measurements (Section 4.2), and from 75% to 3% for blood-lipid phantoms and *in-vivo* measurements (Sections 4.4 and 4.5).

The concentrations of HbO_2 and Hb were calculated using the estimated μ_a at multiple wavelengths and the Beer-Lambert law. For *in-vivo* measurements, another method was also used to calculate the changes in concentrations relative to a baseline, and the results were compared to the first method, as in [60]. The second method uses changes in light attenuation and the modified Beer-Lambert law (MBLL). The mean optical pathlength was calculated for each spectral channel using the method demonstrated by Delpy *et al.* [61], which relies on the measured mean time of flight and the speed of light in tissue. Zhao *et al.* [62] compared the hemoglobin absorption spectra from different sources and found that the most consistent performance was achieved with the values provided by Moaveni *et al.* [63], which were used in this study. We used the

absorption spectra of water provided by Matcher *et al*. [64]. The concentration of water was assumed constant and the contribution of water's μ_a for the estimation of absolute concentrations was addressed as follows. The concentrations of three chromophores (HbO_2, Hb, and water) were estimated in the first step. A mean value of water concentration over the whole measurement was calculated and its contribution to the measured μ_a was subtracted. Finally, the concentrations of only two chromophores (HbO_2 and Hb) were estimated using the water-subtracted μ_a. Resolving for concentrations of only two chromophores leads to less noisy results. The concentrations were calculated using 11 spectral channels that covered the spectral range from 705 to 830 nm.

4. Results and discussions

Results were similar for both detection modules and hence some results are shown for only one.

4.1. BIP protocol

Figure 2 (a) shows the IRFs for 14 spectral channels measured with one detection module and Fig. 2 (b) reports the corresponding FWHM for both detection modules. Figure 2 (c) shows the IRF at 805 nm and the DTOFs measured on two inhomogeneous phantoms that were used for the nEUROPt protocol (before introducing a perturbation). Similar DTOFs for the same solid phantom were reported in [25]. The IRFs match the reported IRF for the same PML detector [39] since the FWHM is close to 150 ps and there is a small afterpulse peak (1 to 2% of the maximum) about 1 ns after the main peak. It is common for conventional PMTs to have such afterpulse peaks, which are probably due to photoelectrons that are reflected at the first dynode but then forced back to the dynode by the electric field, page 169 in [39]. The reported FWHM of multi-wavelength TD-NIRS systems are typically broader, e.g. 465 ps [19], 370 [38], 230 ps [53], and 83 to 263 ps depending on the detector [15], at around 800 nm. The narrowest reported IRF (83 ps) was obtained with a detector that has a much smaller active area (0.1 mm diameter) and hence a much lower responsivity.
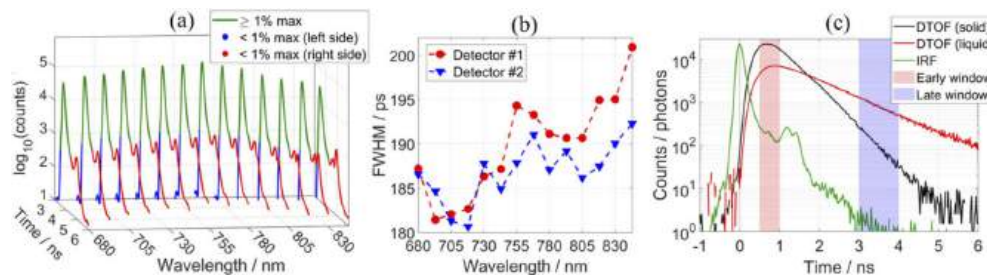
Fig. 2. (a) The IRFs for 14 spectral channels after background subtraction, and (b) the FWHM of the IRFs. (c) The IRF and the DTOFs measured on solid and liquid inhomogeneous phantoms that were used for the nEUROPt protocol, after background subtraction, at 805 nm. Each IRF and DTOF contains about 10^6 photons.

The ε_{DNL} was found to be 3% in the interval between 1 and 10 ns; the maximum deviation of the photon count was 1.5%. This is consistent with the previously reported measures of ε_{DNL}, e.g. 6.77% [16] and 3.5% [24]. The warmup period was found to be between 30 to 60 min, during which time the parameters of the IRF can change drastically. Afterward, long-term drifts can be observed during the next few hours (up to about 5 hours), which can be accounted for by periodically measuring the IRF (e.g. every 30 min). The duration of most clinical measurements is typically less than 1 hour, in which case, after a 30 to 60 min warmup period, it is sufficient to measure the IRF at the start and at the end, i.e. before and after attaching probes to a patient. The two IRFs can be used in data analysis to remove drift in N, m_1, and V, by assuming that the drift

was constant over time. Also, the first and second IRFs can be used for analyzing the first and second half of the measurement, respectively. A more rigorous approach to account for drifts involves directing a small portion of the laser beam to the detector along with the signal from the tissue [15], which can be adapted in the next version of the system.

The calculated temporal fluctuations of moments, which were measured on phantom B2, were about: $\pm 0.2\%$ for N, ± 1.0 ps for m_1, and ± 700 ps^2 for V, at 805 nm. The values at other wavelengths were similar. These reported standard deviations contain the photon noise, which depends on the count rate and shape of the DTOF, and the instrumental noise, which depends on the system [65].

4.2. MEDPHOT protocol

Figure 3 shows the four scatter plots that illustrate the linearity and the coupling of μ_a and μ'_s (for $\rho = 2$ cm and 805 nm). Qualitatively, the scatter plots illustrate an exemplary level of linearity and coupling, for both μ_a and μ'_s. The same was observed for $\rho = 3$ cm and for other wavelengths (not shown). Important to note, for measurements at $\rho = 3$ cm, the signals were too low for some of the more absorbing phantoms and hence phantoms with nominal $\mu_a \geq 0.25$ cm^{-1} (labels 6 to 8) were excluded. For measurements at $\rho = 2$ cm, 31 phantoms were used, excluding only phantom C8. The power of the laser was within the safe limit for measurements on patients (2 mW/mm^2), although it could be increased for phantom measurements.

The mean deviations from linearity and the coupling are reported in Table 1 for two ρ (2 and 3 cm) and two wavelengths (705 and 805 nm). The results are presented for each subset of the 32 phantoms, which provides more information about the system's performance and also allows comparing with other systems that measured on only a subset of phantoms. Measurements on phantoms with the lowest nominal μ'_s (5 cm^{-1}, label A) and lowest nominal μ_a (0 cm^{-1}, label #1) have the highest deviations from linearity for $\rho = 2$ cm but not so much for $\rho = 3$ cm. When estimating low values of optical properties, even small deviations have a high magnitude in units of percentage. Increasing ρ reduces the uncertainty due to the finite width of time bins [40]. Furthermore, the deviation from linearity will be lower if using fewer phantoms since a straight line is easier to fit with fewer data points, while for the same reason the coupling of $\Delta\mu_a$ to $\Delta\mu'_s$ will be worse if using fewer phantoms. This is observed when comparing the results for $\rho = 2$ cm (31 phantoms were used) and $\rho = 3$ cm (20 phantoms were used). The coupling is similar for different phantom sets, except for those that had a low signal level (at $\rho = 3$ cm on phantoms with nominal $\mu_a = 0.20$ cm^{-1}, label 5). The coupling could be in part due to the theoretical model that was used for the fitting method.

The overall measure of linearity and coupling can be taken as the mean of different phantom sets. For $\rho = 2$ cm and 805 nm, the mean deviation from linearity is 4.3% for μ_a and 1.4% for μ'_s, and the mean coupling is 2.8 for $\Delta\mu_a$ to $\Delta\mu'_s$ and 2.2×10^{-4} for $\Delta\mu'_s$ to $\Delta\mu_a$. In other words, if μ'_s increases by ~ 1 cm^{-1}, the system and the used method will show an increase also in μ_a by $\sim 2.2 \times 10^{-4}$ cm^{-1}. The obtained linearity is consistent with previously reported systems, e.g. mean deviation of 4.2% for μ_a and 4.9% for μ'_s [29]. The linearity and coupling reported in [33] were calculated using the median instead of the mean of different phantom sets, which lead to smaller values of linearity (as low as 1% for μ_a and 1.5% for μ'_s) although similar values of coupling (between 1 and 10 for $\Delta\mu_a$ to $\Delta\mu'_s$ and between 2×10^{-4} and 15×10^{-4} for $\Delta\mu'_s$ to $\Delta\mu_a$ for the 29 instruments that were enrolled in the BitMap exercise). The obtained coupling is consistent with the best performance of the reported TD-NIRS systems.

The calculation of linearity requires an array of phantoms with linear increments of μ_a and μ'_s. The calculation of coupling requires also a rough estimate of the step size of the increments. Therefore, similar results could be obtained using e.g. a liquid phantom as in [66], where μ_a and μ'_s were linearly increased by adding ink and Intralipid, respectively. The assessment of linearity and coupling can be enhanced if the true optical properties of the 32 phantoms get established.
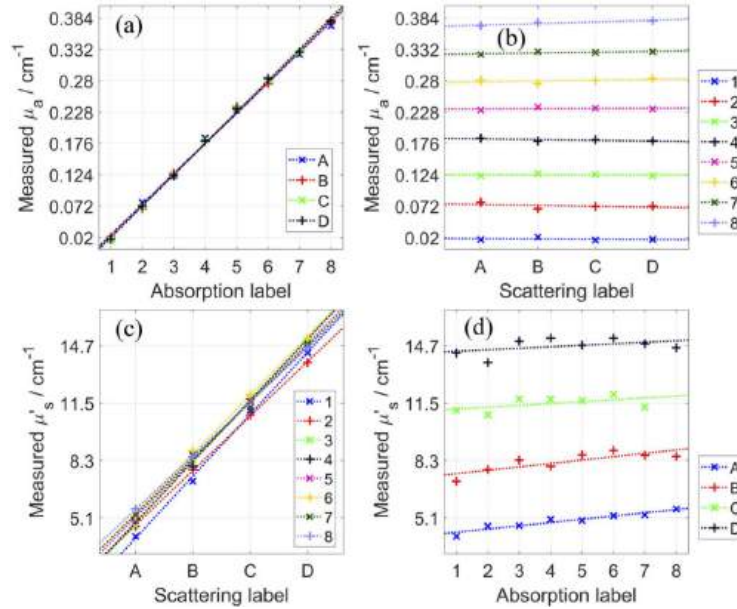
Fig. 3. The obtained μ_a and μ'_s of the 32 phantoms, which make up all combinations of four nominal μ'_s values (from 5 to 20 cm^{-1} in steps of 5 cm^{-1}, labels from A to D) and eight nominal μ_a values (from 0 to 0.35 cm^{-1} in steps of 0.05 cm^{-1}, labels from 1 to 8). These scatter plots can be used to assess the deviation from linearity for μ_a (a) and μ'_s (c), and the coupling of $\Delta\mu'_s$ to $\Delta\mu_a$ (b) and $\Delta\mu_a$ to $\Delta\mu'_s$ (d). The shown values are for $\rho = 2$ cm and 805 nm.

Table 1. The mean deviation from linearity (%) and the coupling (unitless), for μ_a and μ'_s obtained on the 32 phantoms, at two ρ and two wavelengths. Phantoms with nominal $\mu_a \geq 0.25$ cm^{-1} (labels 6 to 8) were excluded for $\rho = 3$ cm due to low signals.

	$\rho = 2$ cm		$\rho = 3$ cm		$\rho = 2$ cm		$\rho = 3$ cm	
	705 nm	805 nm	705 nm	805 nm	705 nm	805 nm	705 nm	805 nm
	Mean deviation in μ_a (%) from linearity				**Coupling of $\Delta\mu_a$ to $\Delta\mu'_s$**			
A	7.8	6.5	3.6	1.8	3.1	3.6	6.8	7.7
B	3.2	3.1	2.9	1.0	4.1	3.8	4.4	5.3
C	2.5	4.1	5.5	1.1	0.9	2.1	3.0	2.4
D	3.6	3.5	3.8	2.5	0.1	1.7	1.7	3.1
Mean	**4.3**	**4.3**	**4.0**	**1.6**	**2.0**	**2.8**	**4.0**	**4.6**
	Mean deviation in μ'_s (%) from linearity				**Coupling of $\Delta\mu'_s$ to $\Delta\mu_a$ ($\times 10^{-4}$)**			
1	4.8	2.2	4.7	4.3	0.2	0.9	1.1	1.1
2	0.2	0.6	2.5	2.4	2.4	2.9	2.0	0.1
3	1.5	1.3	2.4	1.6	4.4	0.3	3.3	6.8
4	1.7	1.9	2.2	3.7	1.8	2.4	0.3	4.8
5	2.8	1.9	2.8	1.9	1.5	0.7	5.6	12.0
6	2.6	1.5	-	-	1.0	2.9	-	-
7	1.0	1.4	-	-	5.3	2.7	-	-
8	0.7	0.4	-	-	5.7	5.2	-	-
Mean	**1.9**	**1.4**	**2.9**	**2.8**	**2.8**	**2.2**	**2.5**	**5.0**

Here, we report the system's accuracy of retrieving the absolute μ_a and μ'_s. The values shown in Fig. 3 match the values in similar scatter plots in [23,25,27,67] for a similar wavelength. The obtained values for $\rho = 3$ cm are similar and one example is shown in Fig. 4 (a). However, due to a lack of true values for the 32 phantoms, we focus on the three well-characterized phantoms that are commonly used for assessing a system's performance. Figure 4 shows the spectra of the obtained μ_a and μ'_s for the three phantoms, and Table 2 reports these values for two ρ along with the previously reported values around the same four wavelengths. Note, most referenced values were roughly estimated from the reported spectral figures for the chosen four wavelengths. The results for phantom B2 match with the previously reported spectra [27–29] since μ'_s is close to 10 cm^{-1} and decreases with wavelength and μ_a is close to 0.07 cm^{-1} at all wavelengths. The obtained values of μ_a, and especially μ'_s, are slightly lower than the previously reported, but consistent with reproducibility of modern TD-NIRS systems, e.g. maximum day-to-day variations with respect to the mean: -5% to +6% for μ_a and -4% to +3% for μ'_s [25]. Similarly, the results for the solid inhomogeneous phantom match the spectra reported in [32], although now the obtained values of μ'_s, and especially μ_a, are slightly higher than the previously reported.
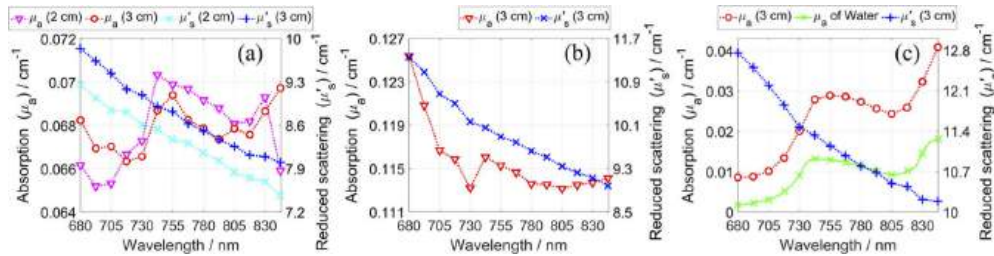

Fig. 4. Obtained spectra of μ_a and μ'_s for phantom B2 (a), solid inhomogeneous phantom (b), and 1% aqueous solution of Intralipid (c). The spacing between data points is 12.5 nm and the dashed lines help guide the eye. The μ_a of water was taken from [64] and plotted with 1 nm spacing.

Table 2. The values of μ_a and μ'_s at four wavelengths for the three phantoms that are shown in Fig. 4, alongside the results that were previously shown for other systems.[a]

μ_a / cm^{-1}				μ'_s / cm^{-1}				ρ / cm	Ref.
~705	~755	~805	~830	~705	~755	~805	~830		
				Phantom B2					
0.065	0.070	0.068	0.069	8.8	8.4	7.8	7.7	2	Fig. 4 (a)
0.067	0.069	0.068	0.069	9.4	8.8	8.3	8.1	3	Fig. 4 (a)
~0.07[690]	~0.07[730]	~0.07[800]	~0.07[830]	~10.5[690]	~10[730]	~9[800]	~8.5[830]	~2.4	[27]
~0.07	~0.07	~0.07	~0.07	~11	~10	~9	~8	2	[29]
0.078[685]	0.076[760]	-	0.073[820]	11.5[685]	9.7[760]	-	8.7[820]	1.5	[25]
~0.075	~0.075	~0.075	-	~12	~11	~10	-	2	[28]
				Solid dynamic phantom					
0.117	0.115	0.113	0.114	10.7	9.9	9.3	9.1	3	Fig. 4 (b)
~0.10	~0.10	~0.09	~0.09	~9.5	~8.5	~8	~7.5	3	[32]
				1% aqueous solution of Intralipid					
0.010	0.029	0.024	0.033	12.2	11.1	10.5	10.2	3	Fig. 4 (c)
~0.01	~0.03	0.026[800]	~0.04	~12.5	~11.5	~10.5	10.38[830]	2	[19]
-	~0.03	~0.025	~0.035	n.a.	n.a.	n.a.	n.a.	1 to 3	[43]

[a]n.a.: Referenced work used other concentrations of Intralipid (0.94% to 4.00%), which resulted in different μ'_s.

Figure 4 (c) shows the results for a 1% aqueous solution of Intralipid alongside the reported μ_a of water. The shape of the obtained μ_a spectra matches that of water, which supports that the system's spectral channels correspond to the specified wavelengths. The μ_a and μ'_s values are close to those reported in [15,19,43] for four wavelengths, and to those reported in [68] for 760 nm ($\mu_a = 0.029\,\text{cm}^{-1}$ and $\mu'_s = 10\,\text{cm}^{-1}$). The system and the used method can retrieve spectra of μ_a and μ'_s with high accuracy, as compared to the previously reported spectra.

4.3. nEUROPt protocol

Figure 5 shows the obtained contrasts of five measurands and the sensitivity factors (SF) of three statistical moments, for the two inhomogeneous phantoms. The quantitative results are
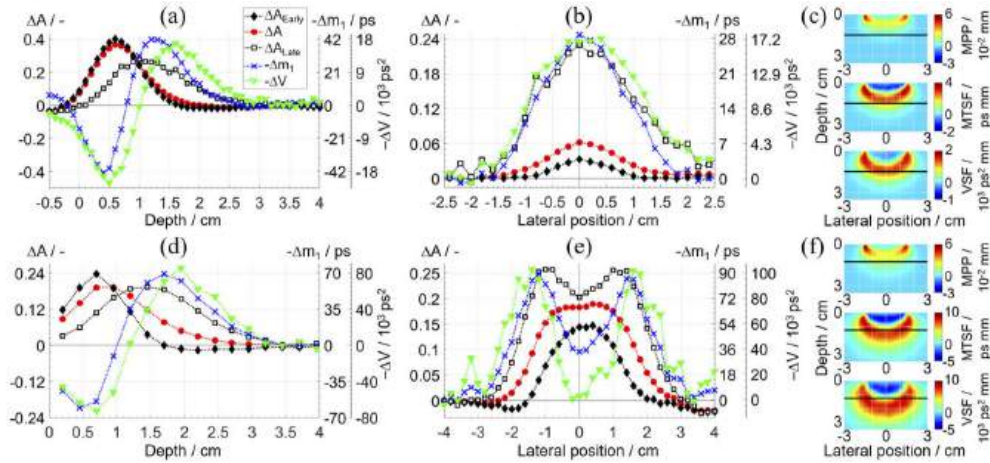

Fig. 5. Contrasts of five measurands (ΔA_{Early}, ΔA, ΔA_{Late}, Δm_1, and ΔV) during depth scans (a, d) and lateral scans (b, e) measured on the solid (top row) and the liquid (bottom row) inhomogeneous phantoms. The lines are drawn to guide the eye. The sensitivity factors (MPP, MTSF, and VSF) (c, f) illustrate the expected behavior for ΔA, Δm_1, and ΔV; the horizontal black lines show the depth of a perturbation during lateral scans. The presented values were obtained at 805 nm.

Table 3. Quantitative parameters of the contrasts in Fig. 5.

Measurand	Maximum contrast		Contrast at 1.5 cm (1.2 cm for liquid)		FWHM / cm
	Depth / cm	Magnitude	Depth scan	Lateral scan	
Solid inhomogeneous phantom, data in Fig. 5 (a, b)					
ΔA_{Early}	0.6	0.400	0.025	0.033	1.1
ΔA	0.6	0.366	0.057	0.062	1.5
ΔA_{Late}	1.0	0.278	0.196	0.230	2.2
Δm_1 / ps	1.2	41.9	37.3	28.7	1.9
ΔV /10^3 ps^2	1.6, ~1.6 [31,42]	16.9, ~20 [31,42]	15.3	16.9	2.3
1% aqueous solution of Intralipid, data in Fig. 5 (d, e)					
ΔA_{Early}	0.70	0.237	0.112	0.144	2.2
ΔA	0.70 to 0.95	0.192	0.164	0.183	3.1
ΔA_{Late}	1.45	0.194	0.188	0.203	-
Δm_1 / ps	1.70	68.9	35.1	34.2	-
ΔV / 10^3 ps^2	1.95	85.6	2.2	2.5	-

summarized in Table 3. The findings for the two phantoms are similar, except for the liquid phantom the contrasts reach deeper and have a higher magnitude.

The contrasts for moments agree with SF and with their known behavior [45] since the position of the maximum contrast is deeper for higher order moments and the FWHM of the lateral scan increases following the broadening of 'banana' shapes. The moments m_1 and V increase when a perturbation is positioned near the surface and decrease when it is positioned deeper; this effect has been well described [45]. Oddly, the contrasts for ΔA can be negative at the smallest depths (the same was reported in [23,24,53]), which corresponds to an increase in the photon count rate after introducing a perturbation, although at these depths a perturbation is outside of the phantom (negative depth). The phantom inherently has a weak heterogeneity in the structure due to a movable part, and importantly, it was found that a homogeneous rod causes a noticeable perturbation [32]. Also, the measurement geometry is not semi-infinite because the rod extends beyond the phantom's surface. These reasons could have contributed to the difference between the obtained Δm_1 (37.3 and 28.7 ps, shown in Table 3) during two scans when a perturbation was at the same depth and lateral position. These reasons are not present for the liquid phantom and the obtained Δm_1 was similar during two scans (35.1 and 34.2 ps). The measure of ΔA is more prone to a slight drift, as seen in Fig. 5 (e) by comparing the values at -4 and 4 cm. Also, the sensitivity of ΔA is focused at a shallow depth, which is a known challenge for continuous-wave NIRS [69]. The results for ΔV are consistent with previous studies on similar phantoms [31,42].

The contrasts of the early $\Delta A_{\mathrm{Early}}$ and late ΔA_{Late} time windows confirm that the later photons on average travel deeper and hence have a higher sensitivity to deeper perturbations. For an ideal system, the latest time windows could probe well beyond a depth of 3 cm [70]. However, an IRF with a substantial late afterpeak can have a devastating effect for time windows [31], although the changes in moments are independent of the IRF if the time range encompasses the whole DTOF [45]. The presented system's IRF allows to confidently use time windows and relevant methods, as confirmed by the IRF parameters (Section 4.1) and ΔA_{Late} in Fig. 5.

4.4. Blood-lipid phantoms

Figure 6 shows time traces of the obtained concentrations and StO_2 for two blood-lipid phantoms during dynamic StO_2 changes. The concentrations obtained with the presented system (TD-NIRS) at 3 and 4 cm are similar, and the values for $\rho = 3$ cm are shown because they contain lower noise. The signal level, i.e. photon count rate, greatly reduced after adding blood, which is a consequence of an increase in μ_a.

The bubbling of oxygen can form bubbles inside the phantom, which then dissipate over time. In Fig. 6 (a, b), HbT always drops by a few μM during the bubbling of oxygen and afterward gradually returns to the initial value (prior to bubbling). The magnitude of the drop is higher for a higher blood concentration and reaches up to ~5 μM for TD-NIRS at 3 cm and OxiplexTS, and up to ~10 μM for TD-NIRS at 4 cm. The time to return to the initial value is about 12 min for TD-NIRS and always longer for OxiplexTS. The chosen zero-time is after oxygen was bubbled, and hence the first cycles show an increasing HbT as it returns to the value that it had. Apart from this dip, HbT remains constant during all desaturation cycles as intended.

The concentration of oxyhemoglobin HbO_2 obtained with TD-NIRS at 3 cm approaches 0 μM at the end of all desaturation events, except at the lowest scattering (25 ml Intralipid) where it is always above 5 μM. Consequently, the corresponding StO_2 is in the range from 100% to 0%, except at the lowest scattering where it is always above 10%. The amount of blood and Intralipid have no apparent effect on the estimation of StO_2 with TD-NIRS at 3 cm, except for the lowest amount of Intralipid. TD-NIRS at 3 and 4 cm obtain similar values of Hb, but the values of HbO_2 for 4 cm are slightly lower at the maximum and higher at the minimum compared with the values for 3 cm, which is amplified for the following cycles. Consequently, StO_2 for 4 cm is in the range from 95% to 10% during the first cycle, and the maximum decreases reducing the

range with each addition of blood or Intralipid. Also, StO$_2$ for 4 cm is significantly noisier, which is visible in Fig. 6 despite the higher temporal averaging. Under most conditions, the system reliably retrieves concentrations and StO$_2$ with good precision.

For an assessment of the accuracy, we compare TD-NIRS with the results of OxiplexTS and co-oximetry. The closest match between the TD-NIRS and the OxiplexTS results is observed for 55 ml of blood (Fig. 6 (a, c)) and 75, 100, and 125 ml of Intralipid (Fig. 6 (b, d)). The largest difference is observed for the lowest concentrations of blood (20 and 35 ml) and Intralipid (25 and 50 ml), where OxiplexTS obtained values slightly below zero. When blood or Intralipid is increased, for the results of OxiplexTS, the maximum of HbO$_2$ remains the same while the minimum increases, such that HbO$_2$ and hence StO$_2$ become non-negative and match closer with TD-NIRS at 3 cm. The previously reported measurements with OxiplexTS on a similar phantom do not have negative values [50], which is probably because the authors used windows that
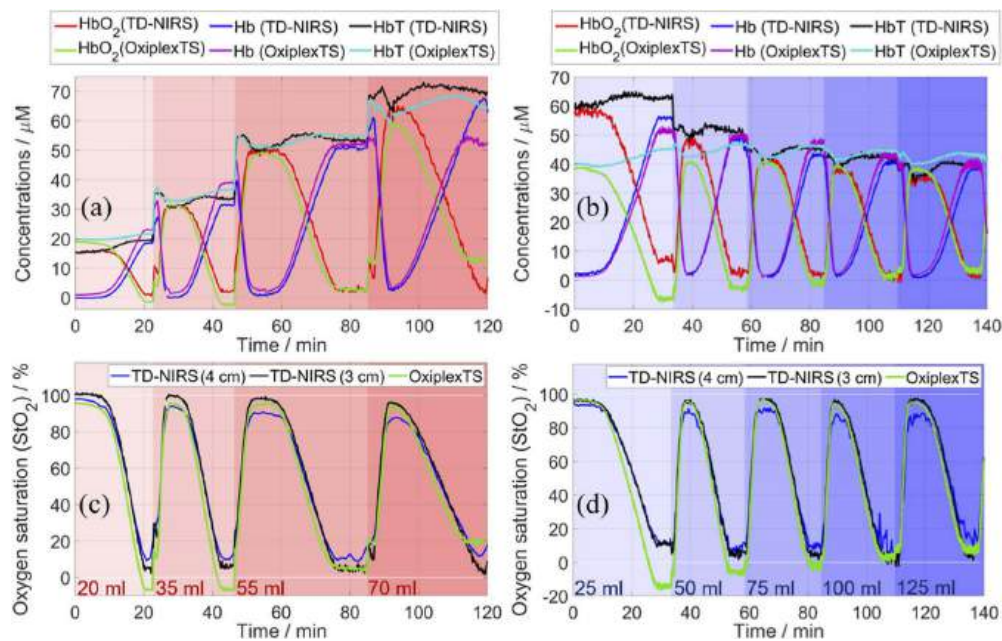

Fig. 6. Measurements on two blood-lipid phantoms that contained a varying amount of blood (left panels) or Intralipid (right panels); the amount is expressed as the background color and written in the bottom panels. Concentrations of HbO$_2$, Hb, and HbT obtained with TD-NIRS at 3 cm and OxiplexTS (a, b). StO$_2$ obtained with TD-NIRS at 3 and 4 cm and OxiplexTS (c, d). For displaying purposes, 10 data points were averaged for TD-NIRS at 3 cm and OxiplexTS, and 30 data points were averaged for TD-NIRS at 4 cm due to higher noise.

Table 4. Comparison of HbT / (μM) obtained using different instruments.

Blood	20 ml	35 ml	55 ml	70 ml	45 ml				
Intralipid	74 ml				25 ml	50 ml	75 ml	100 ml	125 ml
Co-oximetry	21.3	37.0	57.3	72.1	48.1	48.6	48.6	48.4	48.3
OxiplexTS	21.6	36.6	54.7	65.3	45.1	46.8	46.3	44.5	43.1
TD-NIRS (4 cm)	21.4	36.7	56.6	73.0	62.0	50.7	47.7	42.5	42.9
TD-NIRS (3 cm)	19.6	33.5	53.4	69.9	62.9	50.6	45.1	41.9	39.6

mimick a neonatal head (4 mm thickness, $\mu_a = 0.10\,\text{cm}^{-1}$, and $\mu'_s = 9.6\,\text{cm}^{-1}$) and the windows in the present study mimick a layer of fat (1 mm thickness, $\mu_a = 0.063\,\text{cm}^{-1}$, and $\mu'_s = 6\,\text{cm}^{-1}$).

Table 4 reports the mean values of HbT during the plateau regions at the end of desaturation events, which lasted a few minutes, and the results of co-oximetry. The standard deviations of these values are negligible, except for TD-NIRS at 4 cm (~1 µM). OxiplexTS values are close to the results of co-oximetry; the biggest discrepancies are for the highest concentrations of blood and Intralipid. The values of TD-NIRS at 4 cm match with OxiplexTS and co-oximetry within a
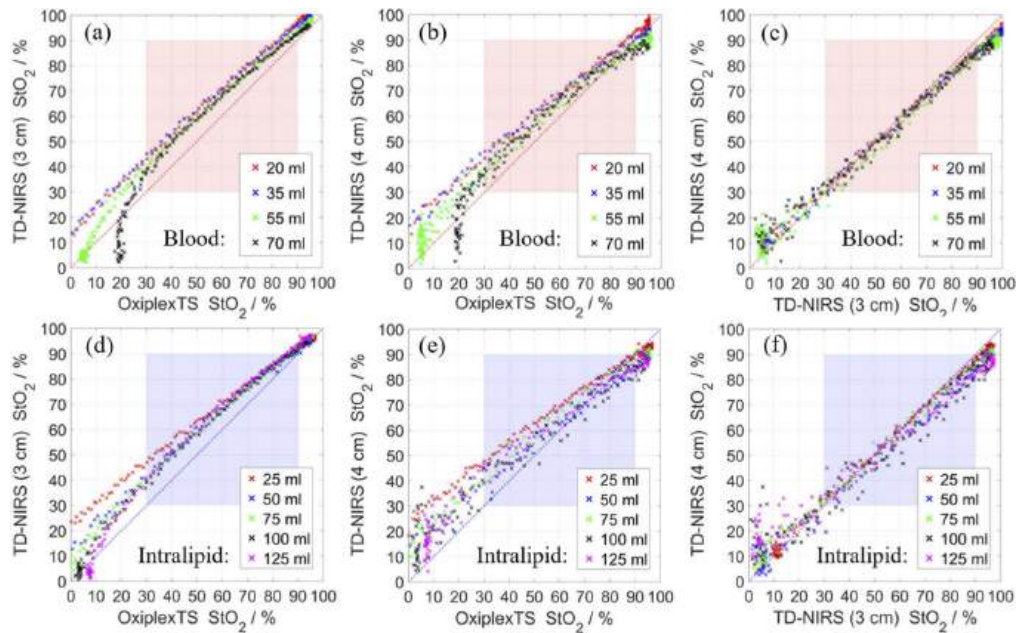

Fig. 7. Comparison of three traces of StO$_2$ in Fig. 6. TD-NIRS at 3 cm versus OxiplexTS (Left panels). TD-NIRS at 4 cm versus OxiplexTS (Middle panels). TD-NIRS at 4 cm versus at 3 cm (Right panels). The legends correspond to the amount of blood or Intralipid inside the phantom. Linear fits were obtained for data points $30\% < \text{StO}_2 < 95\%$ and reported in Table 5.

Table 5. Coefficients for linear transformation of data in Fig. 7:
$StO_2(\textbf{\textit{Device}}\#1) = \textbf{\textit{a}} \times StO_2(\textbf{\textit{Device}}\#2) + \textbf{\textit{b}}$ **. The parameters include intercept (\textbf{\textit{b}}), slope (\textbf{\textit{a}}), and coefficient of determination (\textbf{\textit{R}}^{2}).**

Device #1 → Device #2 →		TD-NIRS (3 cm) OxiplexTS			TD-NIRS (4 cm) OxiplexTS			TD-NIRS (4 cm) TH-NIRS (3 cm)		
Blood	Intralipid	b	a	R^2	b	a	R^2	b	a	R^2
20 ml	74 ml	17.1	0.89	0.9980	19.7	0.82	0.9945	4.1	0.91	0.9936
35 ml	74 ml	19.2	0.86	0.9980	22.4	0.77	0.9953	5.3	0.89	0.9936
55 ml	74 ml	14.5	0.89	0.9972	14.1	0.84	0.9841	0.3	0.95	0.9858
70 ml	74 ml	12.8	0.91	0.9947	14.2	0.83	0.9794	2.5	0.92	0.9837
45 ml	25 ml	25.5	0.75	0.9973	26.9	0.71	0.9934	2.8	0.95	0.9910
45 ml	50 ml	16.9	0.84	0.9923	17.1	0.76	0.9680	2.1	0.89	0.9670
45 ml	75 ml	14.6	0.87	0.9980	18.1	0.79	0.9821	4.8	0.90	0.9845
45 ml	100 ml	14.2	0.88	0.9947	15.6	0.78	0.9360	3.8	0.87	0.9198
45 ml	125 ml	16.1	0.87	0.9960	21.3	0.73	0.9769	8.1	0.83	0.9745

few percent, except at the lowest concentration of Intralipid where TD-NIRS overestimated HbT. The values of TD-NIRS at 3 cm are only slightly lower than the values at 4 cm. In summary, the system can retrieve HbO_2, Hb, HbT, and StO_2 with an accuracy that is consistent with OxiplexTS and co-oximetry, except for the lowest concentration of Intralipid.

The StO_2 data in Fig. 6 were resampled to 10 s on a common time base for comparing the values obtained by different systems during deoxygenation events. The StO_2 values obtained with TD-NIRS are almost always higher than obtained with OxiplexTS (Fig. 7(a, b, d, e)), which could be observed also in Fig. 6. The values obtained with the two systems better match at higher StO_2, which was also found for most systems that were similarly compared with OxiplexTS in [34,35]. Increasing the amount of blood brings the data points closer to the unity line, and varying the amount of Intralipid (excluding 25 ml) does not significantly affect the results. For the TD-NIRS measurements at 3 cm versus 4 cm (Fig. 7(c, f)), most data points are slightly above the unity line at low StO_2 and below the unity line at high StO_2.

The differences between the traces of the obtained StO_2 can be quantified using the approach proposed by Kleiser *et al*. [34,35]: apply a first degree polynomial fit (lowest least square error) to the data in Fig. 7 for values of StO_2 from 30 to 90% (Kleiser *et al.* used 15 to 95%). The obtained parameters of the fit are presented in Table 5 for each deoxygenation cycle. There is no noticeable dependence on the concentration of blood and Intralipid. The slope is always lower than 1 and the y-intercept is always positive. The fits are better than for most systems that were used in [34,35].

The duration of deoxygenation cycles ranged from 23 to 38 min (mean 28 min) and it depended mostly on the added amounts of glucose and blood. A previous study showed a significant decrease in μ'_s (around 2 cm^{-1}) following deoxygenations inside a similar phantom [48]. The μ'_s (obtained with TD-NIRS and OxiplexTS, not shown) was stable in both phantoms and decreased by an insignificant amount. The greatest reduction (about 0.2 cm^{-1} in 30 min) was during the last deoxygenation cycle that had the highest amount of blood. Similar results for Fig. 6 and 7 and Tables 4 and 5 were obtained using a subset of spectral channels of the TD-NIRS system, as long as the first and last channels were included, apart from an increased level of noise when using fewer channels.

4.5.　*In-vivo measurements*

Figure 8 shows the retrieved dynamic changes in concentrations, which were calculated using the fitting method (time-domain information) and the MBLL method (intensity information), during arterial and venous cuff occlusions on the forearm of one subject. For the other two subjects, the following findings were also observed. During the venous occlusion (Fig. 8(a, b)), both HbO_2 and Hb increase at two rates, first rapidly and then much slower (close to 0 for the shown subject, and even negative for HbO_2 for another subject). The observed changes are consistent with the physiology of a venous occlusion [52,55]. During the arterial occlusion (Fig. 8(c, d)), the obtained increase in Hb is greater than the decrease in HbO_2, which leads to an increase in HbT similar as found in [19,38,53,54,56]. After releasing the pressure, the concentrations 'overshoot' and then slowly return to baseline. The expected hemodynamic responses for both occlusions were retrieved using measurements at either $\rho = 3$ or 4 cm.

The measurements at two ρ lead to similar changes in concentrations if using the fitting method, but not if using the MBLL method. The magnitudes are higher for $\rho = 4$ cm and closer to the results of the fitting method. A difference in the trend is noticeable in Fig. 8 (b), where HbO_2 for 3 cm decreases between 2.5 and 4 min but HbO_2 for 4 cm remains constant. An arm is a heterogeneous medium and greater hemodynamic changes are expected to occur in the deeper tissues, i.e. in muscles. The sensitivity is more focused inside the superficial layer for the MBLL method compared to the fitting method [68] and depth sensitivity can be improved for both methods by increasing ρ.
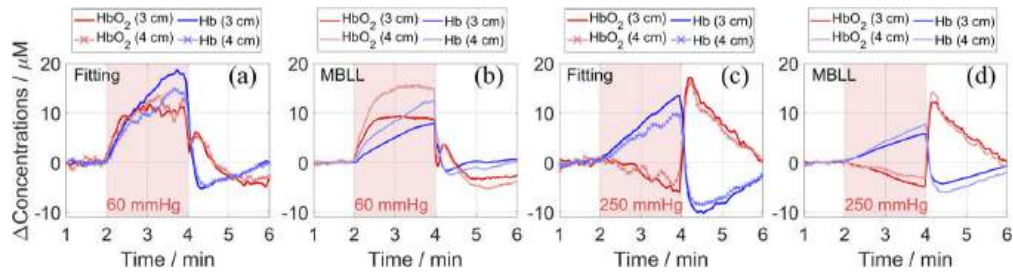
Fig. 8. Changes in the concentrations of HbO$_2$ and Hb obtained *in-vivo* at two ρ (3 and 4 cm) on the forearm of one subject, during a venous (a, b) and an arterial (c, d) cuff occlusion. The results were obtained with the fitting method (a, c) and the MBLL method (b, d). The red background represents the start and end of a 2-min occlusion period. The results of the fitting method were smoothed for displaying purposes: a third order median filter (13.8 s) for ρ = 4 cm, and a smoothing filter (1.5 s) for both ρ.

5. Discussion and future perspectives

This work demonstrated the performance of the system, which is intended for muscle and brain monitoring in a clinical environment. The IRF, the temporal fluctuations, and the warmup time confirm the good specifications of modern electronics (BIP protocol). The warmup time must be considered when planning clinical measurements, and a good IRF is necessary for using time windows and relevant methods [31]. The linearity for μ_a and μ'_s, the coupling between $\Delta\mu_a$ and $\Delta\mu'_s$, and the accuracy of retrieving μ_a and μ'_s were quantitatively assessed (MEDPHOT protocol). The results are consistent with the best performances of previously reported multi-wavelength TD-NIRS systems for a big range of μ_a and μ'_s; the nominal optical properties of the tested phantoms ranged from 0 to 0.04 cm^{-1} for μ_a and from 5 to 20 cm^{-1} for μ'_s. The contrasts measured on the solid inhomogeneous phantom, which has μ_a and μ'_s similar to tissue, confirm the system's sensitivity at great depths for measurements on tissues (if tissue has similar μ_a and μ'_s) since the obtained ΔV is non-zero at up to ~2.5 cm depth. The contrasts measured on the liquid inhomogeneous phantom, which had a much lower μ_a but similar μ'_s, showed a different behavior of measurands but which was consistent with the theory as illustrated with Monte Carlo simulations. Although using later time windows improves depth sensitivity, it also increases noise which hinders the overall performance of detecting deeper changes in μ_a [46].

Blood-lipid phantom measurements demonstrated the system's ability to reliably and accurately retrieve absolute concentrations of hemoglobin, and hence StO$_2$, for phantoms with a varying amount of blood and Intralipid. The results obtained using the reported system (TD-NIRS) are close to the reference measurements, which were obtained using OxiplexTS and co-oximetry. The biggest discrepancy is for the lowest amount of Intralipid, which corresponds to μ'_s lower than a typical biological tissue. Improvements in the method of retrieving optical properties could improve the results. The used blood-lipid phantom is well suited for assessing the performance of oximeters: the ingredients can be precisely varied, the controlled deoxygenation cycles are highly repeatable, and up to four systems can measure in parallel without experiencing cross-talk. The used windows were mimicking a layer of fat, but they could be replaced to mimic other layers, e.g. neonatal head [48]. Previous studies have reported that occasionally the scattering properties of blood-lipid phantoms change over time, which is addressed in [48] and where possible reasons are discussed. In the present work, μ'_s was obtained by both NIRS systems and it did not change significantly over time. The challenges of validating oximeters were described in detail in a review paper [71], including the pros and cons of *in-vitro* and *in-vivo* methods. Recently, Kovacsova *et al.* [72] presented a novel algorithm for measuring StO$_2$ and compared its performance to other published algorithms using data from a blood-lipid phantom that was

developed in their group, as well as *in-vivo* data on a neonate, which demonstrates an example of another blood-lipid phantom and the latest improvements in the assessment of StO_2.

The description of the system explained how 32 DTOFs (16 spectral channels and 2 detection modules) get acquired at up to 3 Hz. A drawback of measuring at 16 wavelengths with a single TCSPC card is the limited count rate, e.g. because of the pile-up effect, which inherently limits the count rate per wavelength compared to measuring at a single wavelength. The optical power is spread over a chosen wavelength range and the current version of the system cannot redistribute it to specific, desired wavelengths. For accurately estimating concentrations of chromophores, the extinction coefficients can be modified to account for the finite spectral bandwidth [73]. An advantage of the system is the excessive number of spectral channels and the fast sampling rate, which combined, may potentially allow monitoring the oxidation state of the CCO enzyme. The time-domain information allows applying depth-resolved methods for separating signals that come from different depths, e.g. brain and extracerebral tissue. Additionally, different spectral channels have slightly different depth profiles, which was exploited by Gerega *et al.* [37] to estimate changes in concentrations of ICG in many layers. The depth-resolved assessment will be investigated in the future and it has the potential to overcome the problems related to the extracerebral layer [69], which will make the measurements more reliable as well as more informative of the cerebral tissue.

The system is well suited for detecting fluorescence during an injection of Indocyanine Green [37], which allows assessing brain perfusion. The current study supports using the system also for other applications that involve monitoring constant and changing optical properties of tissue, e.g. tissue oximetry, tissue spectroscopy, and functional imaging.

6. Conclusions

We presented a description of the multi-wavelength time-domain NIRS system that obtains 32 DTOFs at up to 3 Hz. The quantitative results for the three established protocols are consistent with the best performances of the reported systems. The results for measurements on blood-lipid phantoms are close to the reference values obtained with OxiplexTS and co-oximetry, except a discrepancy was found for the lowest concentration of Intralipid. Venous and arterial cuff occlusions on the forearm resulted in the expected hemoglobin changes that are consistent with the physiology of such hemodynamic challenges. The presented quantitative parameters can be compared to other systems that measured similar tests.

Disclosures. MW is president of the board and co-founder of OxyPrem AG. The other authors declare no conflicts of interest.

Data availability. Data underlying the results presented in this paper are not publicly available at this time but may be obtained from the authors upon reasonable request.

References

1. F. Lange and I. Tachtsidis, "Clinical brain monitoring with time domain NIRS: a review and future perspectives," Appl. Sci. **9**(8), 1612 (2019).
2. G. Bale, C. Elwell, and I. Tachtsidis, "From Jöbsis to the present day: a review of clinical near-infrared spectroscopy measurements of cerebral cytochrome-c-oxidase," J. Biomed. Opt. **21**(9), 091307 (2016).
3. T. Hamaoka and K. K. McCully, "Review of early development of near-infrared spectroscopy and recent advancement of studies on muscle oxygenation and oxidative metabolism," J Physiol Sci **69**(6), 799–811 (2019).
4. G. Bale, S. Mitra, I. de Roever, M. Sokolska, D. Price, A. Bainbridge, R. Gunny, C. Uria-Avellanal, G. S. Kendall, J. Meek, N. J. Robertson, and I. Tachtsidis, "Oxygen dependency of mitochondrial metabolism indicates outcome of newborn brain injury," J Cereb Blood Flow Metab **39**(10), 2035–2047 (2019).

5. S. Kleiser, D. Ostojic, N. Nasseri, H. Isler, H. U. Bucher, D. Bassler, M. Wolf, F. Scholkmann, and T. Karen, "In vivo precision assessment of a near-infrared spectroscopy-based tissue oximeter (OxyPrem v1.3) in neonates considering systemic hemodynamic fluctuations," J. Biomed. Opt. **23**(06), 1–10 (2018).

6. M. Wolf, G. Naulaers, F. van Bel, S. Kleiser, and G. Greisen, "A review of near infrared spectroscopy for term and preterm newborns," J. Near Infrared Spectrosc. **20**(1), 43–55 (2012).

7. V. Quaresima and M. Ferrari, "A mini-review on functional near-infrared spectroscopy (fNIRS): where do we stand, and where should we go?" Photonics **6**(3), 87 (2019).

8. Y. Yamada, H. Suzuki, and Y. Yamashita, "Time-Domain near-infrared spectroscopy and imaging: a review," Appl. Sci. **9**(6), 1127 (2019).

9. G. Bale, S. Mitra, and I. Tachtsidis, "Metabolic brain measurements in the newborn: Advances in optical technologies," Physiol. Rep. **8**(17), e14548 (2020).

10. K. Harvey-Jones, F. Lange, I. Tachtsidis, N. J. Robertson, and S. Mitra, "Role of optical neuromonitoring in neonatal encephalopathy—current state and recent advances," Front. Pediatr. **9**, 653676 (2021).

11. M. Althobaiti and I. Al-Naib, "Recent developments in instrumentation of functional near-infrared spectroscopy systems," Appl. Sci. **10**(18), 6522 (2020).

12. M. Yang, Z. Yang, T. Yuan, W. Feng, and P. Wang, "A systemic review of functional near-infrared spectroscopy for stroke: current application and future directions," Front. Neurol. **10**, 58 (2019).

13. A. Abdalmalak, D. Milej, L. Norton, D. B. Debicki, A. M. Owen, and K. S. Lawrence, "The potential role of fNIRS in evaluating levels of consciousness," Front. Hum. Neurosci. **15**, 703405 (2021).

14. A. Liebert, P. Sawosz, D. Milej, M. Kacprzak, W. Weigl, M. Botwicz, J. Maczewska, K. Fronczewska, E. Mayzner-Zawadzka, L. Królicki, and R. Maniewski, "Assessment of inflow and washout of indocyanine green in the adult human brain by monitoring of diffuse reflectance at large source-detector separation," J. Biomed. Opt. **16**(4), 046011 (2011).

15. S. K. V. Sekar, A. D. Mora, I. Bargigia, E. Martinenghi, C. Lindner, P. Farzam, M. Pagliazzi, T. Durduran, P. Taroni, A. Pifferi, and A. Farina, "Broadband (600–1350 nm) time-resolved diffuse optical spectrometer for clinical use," IEEE J. Sel. Top. Quantum Electron. **22**(3), 406–414 (2016).

16. R. Re, D. Contini, M. Turola, L. Spinelli, L. Zucchelli, M. Caffini, R. Cubeddu, and A. Torricelli, "Multi-channel medical device for time domain functional near infrared spectroscopy based on wavelength space multiplexing," Biomed. Opt. Express **4**(10), 2231–2246 (2013).

17. C. Zhang, S. Lindner, I. M. Antolovic, M. Wolf, and E. Charbon, "A CMOS SPAD imager with collision detection and 128 dynamically reallocating TDCs for single-photon counting and 3D Time-of-flight imaging," Sensors (Basel) 18(11), 4016 (2018).

18. C. Zhang, S. Lindner, I. M. Antolović, J. M. Pavia, M. Wolf, and E. Charbon, "A 30-frames/s, 252 × 144 SPAD flash LiDAR with 1728 dual-clock 48.8-ps TDCs, and pixel-wise Integrated Histogramming," IEEE J. Solid-State Circuits **54**(4), 1137–1151 (2019).

19. F. Lange, L. Dunne, L. Hale, and I. Tachtsidis, "MAESTROS: a multiwavelength time-domain nirs system to monitor changes in oxygenation and oxidation state of cytochrome-C-oxidase," IEEE J. Sel. Top. Quantum Electron. **25**(1), 1–12 (2019).

20. M. Buttafava, E. Martinenghi, D. Tamborini, D. Contini, A. D. Mora, M. Renna, A. Torricelli, A. Pifferi, F. Zappa, and A. Tosi, "A Compact Two-Wavelength Time-Domain NIRS system based on SiPM and pulsed diode lasers," IEEE Photonics J. **9**(1), 1–14 (2017).

21. D. Chitnis, D. Airantzis, D. Highton, R. Williams, P. Thanh, V. Giagka, S. Powell, R. Cooper, I. Tachtsidis, M. Smith, C. Elwell, J. Hebden, and N. Everdell, "Towards a wearable near infrared spectroscopic probe for monitoring concentrations of multiple chromophores in biological tissue in vivo," Rev. Sci. Instrum. **87**(6), 065112 (2016).

22. E. Conca, V. Sesta, M. Buttafava, F. Villa, L. D. Sieno, A. D. Mora, D. Contini, P. Taroni, A. Torricelli, A. Pifferi, F. Zappa, and A. Tosi, "Large-area, fast-gated digital SiPM with integrated TDC for portable and wearable time-domain NIRS," IEEE J. Solid-State Circuits **55**(11), 1 (2020).

23. M. Lacerenza, M. Buttafava, M. Renna, A. D. Mora, L. Spinelli, F. Zappa, A. Pifferi, A. Torricelli, A. Tosi, and D. Contini, "Wearable and wireless time-domain near-infrared spectroscopy system for brain and muscle hemodynamic monitoring," Biomed. Opt. Express **11**(10), 5934–5949 (2020).

24. L. Di Sieno, A. Behera, S. Rohilla, E. Ferocino, D. Contini, A. Torricelli, B. Krämer, F. Koberling, A. Pifferi, and A. D. Mora, "Probe-hosted large area silicon photomultiplier and high-throughput timing electronics for enhanced performance time-domain functional near-infrared spectroscopy," Biomed. Opt. Express **11**(11), 6389–6412 (2020).

25. M. Giovannella, D. Contini, M. Pagliazzi, A. Pifferi, L. Spinelli, R. Erdmann, R. Donat, I. Rocchetti, M. Rehberger, N. König, R. Schmitt, A. Torricelli, T. Durduran, and U. Weigel, "BabyLux device: a diffuse optical system integrating diffuse correlation spectroscopy and time-resolved near-infrared spectroscopy for the neuromonitoring of the premature newborn brain," Neurophotonics **6**(02), 1 (2019).

26. C. Amendola, M. Lacerenza, M. Buttafava, A. Tosi, L. Spinelli, D. Contini, and A. Torricelli, "A compact multi-distance DCS and time domain NIRS hybrid system for hemodynamic and metabolic measurements," Sensors **21**(3), 870 (2021).

27. M. Renna, M. Buttafava, A. Behera, M. Zanoletti, L. Di Sieno, A. Dalla Mora, D. Contini, and A. Tosi, "Eight-wavelength, dual detection-channel instrument for near-infrared time-resolved diffuse optical spectroscopy," IEEE J. Select. Topics Quantum Electron. **25**(1), 1 (2018).

28. J. Swartling, A. Bassi, C. D'Andrea, A. Pifferi, A. Torricelli, and R. Cubeddu, "Dynamic time-resolved diffuse spectroscopy based on supercontinuum light pulses," Appl. Opt. **44**(22), 4684–4692 (2005).

29. A. Pifferi, A. Torricelli, A. Bassi, P. Taroni, H. Wabnitz, D. Grosenick, M. Möller, R. Macdonald, J. Swartling, T. Svensson, S. andersson-engels, R. Veen, H. Sterenborg, J.-M. Tualle, N. Halien, S. Avrillier, M. Whelan, and H. Stamm, "Performance assessment of photon migration instruments: The MEDPHOT protocol," Appl. Opt. **44**(11), 2104–2114 (2005).

30. H. Wabnitz, D. Taubert, M. Mazurenka, O. Steinkellner, A. Jelzow, R. Macdonald, D. Milej, P. Sawosz, M. Kacprzak, A. Liebert, R. Cooper, J. Hebden, A. Pifferi, A. Farina, I. Bargigia, D. Contini, M. Caffini, L. Zucchelli, L. Spinelli, R. Cubeddu, and A. Torricelli, "Performance assessment of time-domain optical brain imagers, part 1: basic instrumental performance protocol," J. Biomed. Opt. **19**(8), 086010 (2014).

31. H. Wabnitz, A. Jelzow, M. Mazurenka, O. Steinkellner, R. Macdonald, D. Milej, N. Zolek, M. Kacprzak, P. Sawosz, R. Maniewski, A. Liebert, S. Magazov, J. Hebden, F. Martelli, P. Di Ninni, G. Zaccanti, A. Torricelli, D. Contini, R. Re, L. Zucchelli, L. Spinelli, R. Cubeddu, and A. Pifferi, "Performance assessment of time-domain optical brain imagers, part 2: nEUROPt protocol," J. Biomed. Opt. **19**(8), 086012 (2014).

32. A. Pifferi, A. Torricelli, G. Quarto, R. Re, S. Konugolu Venkata Sekar, L. Spinelli, A. Farina, F. Martelli, and H. Wabnitz, "Mechanically switchable solid inhomogeneous phantom for performance tests in diffuse imaging and spectroscopy," J. Biomed. Opt. **20**(12), 121304 (2015).

33. P. Lanka, L. Yang, D. Orive-Miguel, J. Deepak Veesa, S. Tagliabue, A. Sudakou, S. Samaei, M. Forcione, Z. Kovacsova, A. Behera, T. Gladytz, D. Grosenick, L. Hervé, G. Lo Presti, L. Cortese, T. Durduran, K. Bejm, M. Morawiec, P. Sawosz, M. Kacprzak, A. Gerega, A. Liebert, A. Belli, I. Tachtsidis, F. Lange, G. Bale, L. Baratelli, S. Gioux, A. Kalyanov, M. Wolf, S. Konugolu Venkata Sekar, M. Zanoletti, I. Pirovano, M. Lacerenza, L. Qiu, E. Ferocino, G. Maffeis, C. Amendola, L. Colombo, M. Buttafava, M. Renna, L. Di Sieno, R. Re, A. Farina, L. Spinelli, A. Dalla Mora, D. Contini, A. Torricelli, A. Tosi, P. Taroni, H. Dehghani, H. Wabnitz, and A. Pifferi, "A multi-laboratory comparison of photon migration instruments and their performances: the BitMap exercise," Proc. SPIE **11639**, 116390F (2021).

34. S. Kleiser, N. Nasseri, B. Andresen, G. Greisen, and M. Wolf, "Comparison of tissue oximeters on a liquid phantom with adjustable optical properties," Biomed. Opt. Express **7**(8), 2973–2992 (2016).

35. S. Kleiser, D. Ostojic, B. Andresen, N. Nasseri, H. Isler, F. Scholkmann, T. Karen, G. Greisen, and M. Wolf, "Comparison of tissue oximeters on a liquid phantom with adjustable optical properties: an extension," Biomed. Opt. Express **9**(1), 86–101 (2018).

36. A. Gerega, D. Milej, W. Weigl, N. Zolek, P. Sawosz, R. Maniewski, and A. Liebert, "Multi-wavelength time-resolved measurements of diffuse reflectance: phantom study with dynamic inflow of ICG," Biomedical Optics and 3-D Imaging (Optical Society of America, 2012), p. JM3A.31.

37. A. Gerega, D. Milej, W. Weigl, M. Kacprzak, and A. Liebert, "Multiwavelength time-resolved near-infrared spectroscopy of the adult head: assessment of intracerebral and extracerebral absorption changes," Biomed. Opt. Express **9**(7), 2974 (2018).

38. R. Re, I. Pirovano, D. Contini, L. Spinelli, and A. Torricelli, "Time domain near infrared spectroscopy device for monitoring muscle oxidative metabolism: custom probe and in vivo applications," Sensors **18**(1), 264 (2018).

39. B. H. GmbH, "The bh TCSPC Handbook," User Handbook, 8th edition, https://www.becker-hickl.com (2019).

40. V. Ntziachristos and B. Chance, "Accuracy limits in the determination of absolute optical properties using time-resolved NIR spectroscopy," Med. Phys. **28**(6), 1115–1124 (2001).

41. A. Liebert, H. Wabnitz, D. Grosenick, and R. Macdonald, "Fiber dispersion in time domain measurements compromising the accuracy of determination of optical properties of strongly scattering media," J. Biomed. Opt. **8**(3), 512 (2003).

42. F. Martelli, P. Ninni, G. Zaccanti, D. Contini, L. Spinelli, A. Torricelli, R. Phd, H. Wabnitz, M. Mazurenka, R. Macdonald, A. Sassaroli, and A. Pifferi, "Phantoms for diffuse optical imaging based on totally absorbing objects, part 2: Experimental implementation," J. Biomed. Opt. **19**(7), 076011 (2014).

43. B. Cletus, R. Kunnemeyer, P. Martinsen, A. McGlone, and R. Jordan, "Characterizing liquid turbid media by frequency-domain photon-migration spectroscopy," J. Biomed. Opt. **14**(2), 024041 (2009).

44. S. Wojtkiewicz and A. Liebert, "Parallel, multi-purpose Monte Carlo code for simulation of light propagation in segmented tissues," Biocybernetics and Biomedical Engineering, https://doi.org/10.1016/j.bbe.2021.03.001 (2021).

45. H. Wabnitz, D. Contini, L. Spinelli, A. Torricelli, and A. Liebert, "Depth-selective analysis in time-domain optical brain imaging: moments vs time windows," Biomed. Opt. Express **11**(8), 4224–4243 (2020).

46. A. Sudakou, L. Yang, H. Wabnitz, S. Wojtkiewicz, and A. Liebert, "Performance of measurands in time-domain optical brain imaging: depth selectivity versus contrast-to-noise ratio," Biomed. Opt. Express **11**(8), 4348–4365 (2020).

47. S. Hyttel-Sorensen, S. Kleiser, M. Wolf, and G. Greisen, "Calibration of a prototype NIRS oximeter against two commercial devices on a blood-lipid phantom," Biomed. Opt. Express **4**(9), 1662–1672 (2013).

48. D. Ostojic, S. Kleiser, N. Nasseri, H. Isler, B. Andresen, H. Wabnitz, T. Karen, F. Scholkmann, and M. Wolf, "In Vitro Comparisons of Near-Infrared Spectroscopy Oximeters: Impact of Slow Changes in Scattering of Liquid Phantoms," Adv. Exp. Med. Biol. **1072**, 375–379 (2018).

49. D. Ostojic, S. Kleiser, N. Nasseri, H. Isler, F. Scholkmann, T. Karen, and M. Wolf, "Hemoglobin spectra affect measurement of tissue oxygen saturation," Proc. SPIE **10486**, 104860T (2018).

50. S. Kleiser, S. Hyttel-Sorensen, G. Greisen, and M. Wolf, "Comparison of Near-infrared oximeters in a liquid optical phantom with varying intralipid and blood content," Adv. Exp. Med. Biol. **876**, 413–418 (2016).

51. S. Hyttel-Sorensen, L. C. Sorensen, J. Riera, and G. Greisen, "Tissue oximetry: a comparison of mean values of regional tissue saturation, reproducibility and dynamic range of four NIRS-instruments on the human forearm," Biomed. Opt. Express **2**(11), 3047–3057 (2011).

52. C. Casavola, L. A. Paunescu, S. Fantini, and E. Gratton, "Blood flow and oxygen consumption with near-infrared spectroscopy and venous occlusion: spatial maps and the effect of time and pressure of inflation," J. Biomed. Opt. **5**(3), 269–276 (2000).

53. R. Re, E. Martinenghi, A. Dalla Mora, D. Contini, A. Pifferi, and A. Torricelli, "Probe-hosted silicon photomultipliers for time-domain functional near-infrared spectroscopy: phantom and in vivo tests," Neurophotonics **3**(4), 045004 (2016).

54. D. Orive-Miguel, L. Di Sieno, A. Behera, E. Ferocino, D. Contini, L. Condat, L. Hervé, J. Mars, A. Torricelli, A. Pifferi, and A. Dalla Mora, "Real-time dual-wavelength time-resolved diffuse optical tomography system for functional brain imaging based on probe-hosted silicon photomultipliers," Sensors **20**(10), 2815 (2020).

55. T. J. Cross and S. Sabapathy, "The impact of venous occlusion per se on forearm muscle blood flow: implications for the near-infrared spectroscopy venous occlusion technique," Clin. Physiol. Funct. Imaging **37**(3), 293–298 (2017).

56. R. Re, D. Contini, L. Zucchelli, A. Torricelli, and L. Spinelli, "Effect of a thin superficial layer on the estimate of hemodynamic changes in a two-layer medium by time domain NIRS," Biomed. Opt. Express **7**(2), 264–278 (2016).

57. S. Mosca, P. Lanka, N. Stone, S. Konugolu Venkata Sekar, P. Matousek, G. Valentini, and A. Pifferi, "Optical characterisation of porcine tissues from various organs in the 650–1100 nm range using time-domain diffuse spectroscopy," Biomed. Opt. Express **11**(3), 1697–1706 (2020).

58. M. S. Patterson, B. Chance, and B. C. Wilson, "Time resolved reflectance and transmittance for the noninvasive measurement of tissue optical properties," Appl. Opt. **28**(12), 2331–2336 (1989).

59. H. Dehghani, M. E. Eames, P. K. Yalavarthy, S. C. Davis, S. Srinivasan, C. M. Carpenter, B. W. Pogue, and K. D. Paulsen, "Near infrared optical tomography using NIRFAST: Algorithm for numerical model and image reconstruction," Commun. Numer. Meth. Engng **25**(6), 711–732 (2009).

60. F. Lange, L. Dunne, and I. Tachtsidis, "Evaluation of haemoglobin and cytochrome responses during forearm ischaemia using multi-wavelength time domain NIRS," Adv. Exp. Med. Biol. **977**, 67–72 (2017).

61. D. T. Delpy, M. Cope, P. van der Zee, S. Arridge, S. Wray, and J. Wyatt, "Estimation of optical pathlength through tissue from direct time of flight measurement," Phys. Med. Biol. **33**(12), 1433–1442 (1988).

62. Y. Zhao, L. Qiu, Y. Sun, C. Huang, and T. Li, "Optimal hemoglobin extinction coefficient data set for near-infrared spectroscopy," Biomed. Opt. Express **8**(11), 5151–5159 (2017).

63. M. K. Moaveni, "A multiple scattering field theory applied to whole blood," PhD thesis in Dept. of Electrical Engineering. University of Washington (1970).

64. S. J. Matcher, M. Cope, and D. T. Delpy, "Use of the water absorption spectrum to quantify tissue chromophore concentration changes in near-infrared spectroscopy," Phys. Med. Biol. **39**(1), 177–196 (1994).

65. A. Jelzow, "In vivo quantification of absorption changes in the human brain by time-domain diffuse near-infrared spectroscopy," PhD Thesis, Technischen Universität Berlin (2013).

66. R. Cubeddu, A. Pifferi, P. Taroni, A. Torricelli, and G. Valentini, "Compact tissue oximeter based on dual-wavelength multichannel time-resolved reflectance," Appl. Opt. **38**(16), 3670–3680 (1999).

67. A. Pifferi, A. Torricelli, P. Taroni, D. Comelli, A. Bassi, and R. Cubeddu, "Fully automated time domain spectrometer for the absorption and scattering characterization of diffusive media," Rev Sci Instrum **78**(5), 053103 (2007).

68. S. Gunadi, T. S. Leung, C. E. Elwell, and I. Tachtsidis, "Spatial sensitivity and penetration depth of three cerebral oxygenation monitors," Biomed. Opt. Express **5**(9), 2896–2912 (2014).

69. I. Tachtsidis and F. Scholkmann, "False positives and false negatives in functional near-infrared spectroscopy: issues, challenges, and the way forward," Neurophotonics **3**(3), 031405 (2016).

70. A. D. Mora, D. Contini, S. Arridge, F. Martelli, A. Tosi, G. Boso, A. Farina, T. Durduran, E. Martinenghi, A. Torricelli, and A. Pifferi, "Towards next-generation time-domain diffuse optics for extreme depth penetration and sensitivity," Biomed. Opt. Express **6**(5), 1749–1760 (2015).

71. C. Hornberger and H. Wabnitz, "Approaches for calibration and validation of near-infrared optical methods for oxygenation monitoring," Biomedical Engineering / Biomedizinische Technik **63**(5), 537–546 (2018).

72. Z. Kovacsova, G. Bale, S. Mitra, F. Lange, and I. Tachtsidis, "Absolute quantification of cerebral tissue oxygen saturation with multidistance broadband NIRS in newborn brain," Biomed. Opt. Express **12**(2), 907–925 (2021).

73. M. Singh, J. Singh, B. Singh, and C. Ghanshyam, "Quantifying the effect of finite spectral bandwidth on extinction coefficient of species in laser absorption spectroscopy," Journal of Molecular Spectroscopy **329**, 20–27 (2016).

Two-layered blood-lipid phantom and method to determine absorption and oxygenation employing changes in moments of DTOFs

ALEH SUDAKOU,[1] **HEIDRUN WABNITZ,**[2] **ANDRÉ LIEMERT,**[3] **MARTIN WOLF,**[4] **AND ADAM LIEBERT**[1]

[1]*Nałęcz Institute of Biocybernetics and Biomedical Engineering Polish Academy of Sciences, Warsaw, Poland*
[2]*Physikalisch-Technische Bundesanstalt (PTB), Berlin, Germany*
[3]*Institut für Lasertechnologien in der Medizin und Meßtechnik an der Universität Ulm, Germany*
[4]*Department of Neonatology, University Hospital Zurich, University of Zurich, Zurich, Switzerland*

Abstract: Near-infrared spectroscopy (NIRS) is an established technique for measuring tissue oxygen saturation (StO$_2$), which is of high clinical value. For tissues that have layered structures, it is challenging but clinically relevant to obtain StO$_2$ of the different layers, e.g. brain and scalp. For this aim, we present a new method of data analysis for time-domain NIRS (TD-NIRS) and a new two-layered blood-lipid phantom. The new analysis method enables accurate determination of even large changes of the absorption coefficient ($\Delta\mu_a$) in multiple layers. By adding $\Delta\mu_a$ to the baseline μ_a, this method provides absolute μ_a and hence StO$_2$ in multiple layers. The method utilizes (i) changes in statistical moments of the distributions of times of flight of photons (DTOFs), (ii) an analytical solution of the diffusion equation for an N-layered medium, (iii) and the Levenberg–Marquardt algorithm (LMA) to determine $\Delta\mu_a$ in multiple layers from the changes in moments. The method is suitable for NIRS tissue oximetry (relying on μ_a) as well as functional NIRS (fNIRS) applications (relying on $\Delta\mu_a$). Experiments were conducted on a new phantom, which enabled us to simulate dynamic StO$_2$ changes in two layers for the first time. Two separate compartments, which mimic superficial and deep layers, hold blood-lipid mixtures that can be deoxygenated (using yeast) and oxygenated (by bubbling oxygen) independently. Simultaneous NIRS measurements can be performed on the two-layered medium (variable superficial layer thickness, L), the deep (homogeneous), and/or the superficial (homogeneous). In two experiments involving ink, we increased the nominal μ_a in one of two compartments from 0.05 to 0.25 cm^{-1}, L set to 14.5 mm. In three experiments involving blood (L set to 12, 15, or 17 mm), we used a protocol consisting of six deoxygenation cycles. A state-of-the-art multi-wavelength TD-NIRS system measured simultaneously on the two-layered medium, as well as on the deep compartment for a reference. The new method accurately determined μ_a (and hence StO$_2$) in both compartments. The method is a significant progress in overcoming the contamination from the superficial layer, which is beneficial for NIRS and fNIRS applications, and may improve the determination of StO$_2$ in the brain from measurements on the head. The advanced phantom may assist in the ongoing effort towards more realistic standardized performance tests in NIRS tissue oximetry. Data and MATLAB codes used in this study were made publicly available.

1. Introduction

Near-infrared spectroscopy (NIRS) is a non-invasive and safe (even for long continuous monitoring) technique in biomedical optics for studying brain functions and its disorders. NIRS tissue oximetry enables monitoring vital parameters in real time, reporting on the balance between

oxygen supply and consumption. The clinical usefulness of NIRS has been demonstrated by a wide range of clinical applications and trials (reviewed in [1–9]) and the popularity of NIRS continues to grow in part due to the continuous advancements in instrumentation and the resultant increasing number of NIRS systems (reviewed in [10–15]). A significant improvement to NIRS tissue oximetry would be the determination of StO_2 in multiple layers and a means of testing such method. Another field of NIRS is functional NIRS (fNIRS), which typically involves small hemodynamic changes (i.e. small $\Delta\mu_a$) related to brain activity [16,17]. The new data analysis method and the phantom introduced in this study may be useful for both fNIRS and NIRS tissue oximetry applications.

The analysis of NIRS measurements carried out on a layered tissue structure, such as the head, require a multi-layered model as the homogeneous model is inadequate [18–22]. Recent advances in modeling the light propagation in tissue (theories, solutions, and validations) are explained in the most recent book by Martelli et al. [23]. In this study, we used the time-domain NIRS (TD-NIRS) modality, which records the distribution of times of flight of photons (DTOFs), providing the most information about light propagation compared to continuous-wave (steady-state) and frequency-domain modalities [16]. Light in tissue can be modelled using the radiative transfer equation (RTE) and a commonly employed solution is the diffusion equation, which relies on the diffusion approximation [24–26]. Helton et al. [27] presented an open-access numerical routine for solving the diffusion equation for an arbitrary number of layers, for the steady-state case and in the time domain. Geiger et al. [28] modeled light propagation using spherical harmonics instead of the diffusion equation and presented the analytical solutions for the RTE. To solve for complex geometries, the finite element method can be used, e.g. NIRFAST [29]. Another approach for modelling light propagation is based on the Monte Carlo method [30,31], which allows implementing any geometry but the main disadvantage is the long computational time. We will use the analytical solution for an N-layered medium presented by Liemert et al. [32], which applies the Laplace transform (LT) to a solution in the frequency domain (could be either numerical or analytical) to obtain the solution in the time domain. LT has important advantages over the commonly used Fourier transform, such as accuracy, efficiency (speed-up of up to several orders of magnitude), and numerical stability. Having a model for light propagation and its solution, the optical properties can be obtained from measured NIRS data by solving the inverse problem.

Various algorithms have been developed for determining the absorption (μ_a) or its changes ($\Delta\mu_a$) at multiple depths of a multi-layered turbid medium using TD-NIRS measurements, e.g. more recently in Refs. [28,33–36]. We will use the Levenberg–Marquardt algorithm (LMA), which allows solving nonlinear iterative least squares minimization problems [37,38]. The LMA is a fitting routine that searches for a solution that minimizes an error, i.e. the difference between the measured data and the theoretically-calculated data. Garcia et al. [35] proposed implementing the Kalman filter algorithm, which is another iterative algorithm that has some advantages over the LMA. Instead of using the DTOF as a measurand, Hallacoglu et al. [39] used the amplitude change and the phase shift at multiple source-detector distances as the measurands for the LMA. Steinbrink et al. [40] used changes in the number of photons in different time-channels of a DTOF for determining $\Delta\mu_a$ at different depths, since different time-channels have different depth sensitivity profiles. Similarly, different-order statistical moments of the DTOF have different depth sensitivity profiles and Liebert et al. [41,42] outlined the use of moments for the determination of $\Delta\mu_a$ at multiple depths. This has become a well-established method, e.g. [43–46]. Recent performance-assessment studies, including quantitative tests, found that moments outperform other measurands in terms of assessing $\Delta\mu_a$ in deep layers [47–49]. Using changes in moments at multiple wavelengths, which have slightly different depth sensitivity profiles, it was possible to estimate changes in the concentration of an injected indocyanine green (ICG) bolus in up to 24 layers [50]. However, up to now, the method relied on the assumption that

the changes in moments are linearly proportional to $\Delta\mu_a$, where the proportionality constants are the sensitivity factors [41]. This inverse problem of determining $\Delta\mu_a$ from changes in moments was solved using the linear least squares method or the singular value decomposition approach, i.e. non-iterative approaches.

One goal of this work is to improve the method based on the analysis of moments of DTOFs by using the analytical solution of the diffusion equation for a multi-layered medium and implementing the LMA. With this approach, we solve a nonlinear iterative least squares minimization problem, hence we remove the limiting assumption that changes in moments are linearly proportional to $\Delta\mu_a$. In addition to testing the method on phantom measurements, we will investigate how errors in the values of the baseline parameters affect the determined $\Delta\mu_a$ values. We aim to provide a more accurate and robust method for determining $\Delta\mu_a$ at multiple depths in a multi-layered medium.

When introducing a new method of data analysis or a new system, phantom measurements are a necessary test before conducting *in-vivo* studies as phantoms allow to study the influence of the instrumental factors and uncertainties for well-defined geometries and optical properties [51]. There is an ongoing effort towards standardization of system performance tests in the field of NIRS [15,51], which has become increasingly important in part due to the increasing number of NIRS systems [10–15]. Recently, Lanka et al. [52] presented the results of the BitMap campaign, which was a multi-laboratory effort to perform a standardized performance assessment of instruments for diffuse optics, which used the BIP [53], nEUROPt [54], and MEDPHOT [55] protocols. Other standardization efforts resulted in a consensus by many groups on the guidelines for the best practices for fNIRS publications [56]. Over the past decade, many tissue-mimicking phantoms for optical spectroscopy have been developed, and they are reviewed in [51,57–59], including challenges related to their construction and utilization. Konugolu Venkata Sekar et al. [60] developed solid tissue-like phantoms that mimic the anatomically correct 3D shapes of human organs for biomedical applications, e.g. [61]. For testing tissue oximeters and for other biophotonics applications, there is a need for advanced phantoms that can provide realistic simulations of tissues' optical properties. Liu et al. [62] developed a phantom that achieves simulating vascular oxygenation and perfusion, by filling with blood the tubes that mimic vessels. Afshari et al. [59] developed a phantom with an array of 148 cylindrical channels, filled with whole bovine blood, as a new approach for standardized testing of clinical oximeters. An established concept for a phantom is using whole human blood (mixed in a turbid suspension) for mimicking repeatable controlled dynamic oxygen saturation (StO_2) levels from 0 to 100%. To date, all presented phantoms that used this concept had a single homogeneous liquid compartment, e.g. [63–67]. However, when NIRS is intended to study deeper structures, e.g. the brain, it is crucial to address the influence of the superficial layer on the measured StO_2 [18–22].

The second goal of this work is to develop a phantom with two compartments (superficial and deep), each of which can hold a mixture containing blood that can be oxygenated or deoxygenated. The phantom is a tool that will allow quantitatively studying the contamination from the superficial layer when determining StO_2 in a two-layered medium. We will utilize the phantom to demonstrate the proposed method's capabilities of determining StO_2 in both layers.

Data and MATLAB codes used in this study were made publicly available [68].

2. Methods and materials

2.1. NIRS system

The multi-wavelength TD-NIRS system was developed by Gerega et al. [69] at IBIB PAN and it was described and experimentally tested in our recent study [70], revealing its advantages compared to the current state-of-the-art systems. The system can simultaneously acquire DTOFs at 16 spectral channels (from 680 to 875 nm, with a 12.5 nm/channel width) for each of two detection modules. Each module consists of a polychromator, a multi-anode 16-channel

photomultiplier tube, and a 16-channel TCSPC card, as described in [70]. Two emitting fibers and two detection fiber bundles allow simultaneous measurements on two windows of the phantom in reflectance geometry. The previous supercontinuum laser (SC480-8 WhiteLase, Fianium, UK) was replaced with a newer laser (NKT SuperK EXTREME (EXR-15), Denmark), which has similar characteristics. We used the repetition rate of 78 MHz and set the constant current power to 50% in the laser driver. The parameters of a TCSPC card were configured so that each DTOF contained 1024 time bins with a width of 12.22 ps. This width is sufficiently small as a study on accuracy suggested that a bin width of about 10 ps enables a better than 5% accuracy in quantifying optical properties using the curve fitting method [71].

In this study, the distance between the source and detector fibers was set to 30 mm. The acquisition time was 0.3 s and the sampling rate was 3 Hz. To increase the signal-to-noise ratio and reduce the computational time, 9 consecutive DTOFs were summed for measurements on phantoms with blood, resulting in a sampling time of 3 s. For measurements with ink, 128 DTOFs were summed for each $\Delta\mu_a$ step, resulting in a sampling time of 42.7 s. We used a shorter sampling time for analyzing measurements with blood to resolve the dynamic changes of StO_2. We used a longer sampling time for experiments involving ink to reduce noise since the optical properties were stable.

To measure the instrumental response function (IRF), an emission fiber was aligned with a detection fiber bundle in transmission geometry at a distance of 6 cm with a neutral density filter between them and two pieces of white paper covering the source fiber and the detection fiber bundle [72]. The maximum laser power was measured as 15 mW for each emission fiber, which would equate to a power density of less than 1.5 mW/mm^2 on a skin's surface [70]. For a recent comprehensive study on IRF, see the study conducted by Pirovano et al. [73].

2.2. Data analysis

The measured NIRS data were stored and later analyzed using custom codes written in MATLAB R2020b. The LMA was implement using the function *lsqcurvefit* in MATLAB.

2.2.1. Determination of μ_a and μ'_s (homogeneous model)

To determine the values of μ_a and the reduced scattering coefficient (μ'_s) from a measured DTOF, we used a solution of the diffusion equation for a homogeneous medium and the LMA. This is known as the curve-fitting method and it is regarded as the gold-standard approach for analyzing time-domain diffuse reflectance measurements [37,38,71], and an example of the distribution of error norm was presented in [74].

We used a homogeneous semi-infinite medium model under the extrapolated boundary conditions, which was done by using the solution of the diffusion equation for an N-layered medium [32] with N set to 1. We used equations presented in [25], which allow to account for the boundary conditions. The theoretically-obtained DTOFs are convolved with the IRF that was measured at the start of an experiment. Analyzing each measured DTOF separately, we first subtracted the background signal and then used the time-channels from 85% on the rising edge to 1% on the tail for determining μ_a and μ'_s.

2.2.2. Determination of $\Delta\mu_a$ in two layers

In this section we outline an improved method of determining $\Delta\mu_a$ in multiple layers. To obtain the absolute μ_a with this method, we added the determined $\Delta\mu_a$ values to the baseline μ_a values, which were obtained using the method explained in the previous section.

DTOF is represented by a histogram of photon counts (N_i) at time channels (t_i) indexed by i [41]. The first three statistical moments of DTOFs are: $m_0 = N_{tot} = \sum N_i$ (total number of photons), $m_1 = \sum t_i N_i / N_{tot}$ (mean time of flight), and $m_2^C = V = \sum (t_i - m_1)^2 N_i / N_{tot}$ (variance). The change in attenuation is: $\Delta A = -\log(N_{tot}^* / N_{tot})$, where N_{tot}^* is after $\Delta\mu_a$. Moments have

several important advantageous properties. To deconvolve the influence of the IRF, the moments of the IRF are subtracted from the moments of the DTOF; valid for m_1, m_2^C, and m_3^C (third central moment) [46]. The resulting moments can be used to calculate the optical properties of tissue [75]. Changes in moments are independent of the IRF under the assumption that the moments of the IRF are constant. The uncertainty of moments due to photon noise, which behaves like Poisson noise (Poisson statistics), can be calculated using higher-order moments [42,46].

The method that uses the changes in moments (ΔA, Δm_1, and/or ΔV) requires two DTOFs: during baseline and after $\Delta\mu_a$. For small $\Delta\mu_a$ in multiple layers, the corresponding changes in moments are linearly proportional to $\Delta\mu_a$ in each layer, where the proportionality constants are the sensitivity factors (SF) for each layer, as explained by Steinbrink et al. [40] and Liebert et al. [41,42]. The SF for baseline optical properties can be obtained using Monte Carlo simulations [30] or an analytical solution of the diffusion equation [43], and then it is a linear inverse problem to determine $\Delta\mu_a$ from the measured changes in moments.

To improve the method, we overcome the assumption that the changes in moments are linearly proportional to $\Delta\mu_a$ by using the solution of the diffusion equation for an N-layered medium [32] and the LMA. In this study, we set N to 2, assumed the deeper layer is semi-infinite, and assumed the extrapolated boundary conditions. The use of LMA avoids the need for sensitivity factors. For a guess of $\Delta\mu_a$ in each layer, the analytical solution is used to generate the corresponding two DTOFs for which changes in moments are calculated. The LMA searches for $\Delta\mu_a$ in each layer that result in the smallest error norm (χ^2), which is the difference between the measured and the theoretically calculated changes in moments. The different-order moments have different units and levels of uncertainty. To account for these, we weighted each moment by its uncertainty due to photon noise [42]. When all three moments are considered, χ^2 can be calculated using the equation:

$$\chi^2 = \left(\frac{\Delta A_{\text{sim}} - \Delta A}{\delta\Delta A}\right)^2 + \left(\frac{\Delta m_{1,\text{sim}} - \Delta m_1}{\delta\Delta m_1}\right)^2 + \left(\frac{\Delta V_{\text{sim}} - \Delta V}{\delta\Delta V}\right)^2 \tag{1}$$

where changes in moments are calculated from two DTOFs: $\Delta A = A - A^*$, $\Delta m_1 = m_1 - m_1^*$, and $\Delta V = V - V^*$, where the star denotes the value of a moment after $\Delta\mu_a$. For a guess of $\Delta\mu_a$, the corresponding changes in moments (ΔA_{sim}, $\Delta m_{1,\text{sim}}$, and ΔV_{sim}) are calculated from the theoretically obtained DTOFs. The uncertainties due to photon noise ($\delta\Delta A$, $\delta\Delta m_1$, and $\delta\Delta V$) can be calculated using higher-order moments [42]. We make a simplifying assumption that the noise of moments of two DTOFs (before and after $\Delta\mu_a$) is the same (true if $\Delta\mu_a = 0$).

$$\chi^2 = \left(\frac{\Delta A_{\text{sim}} - \Delta A}{\sqrt{2/N_{\text{tot}}}}\right)^2 + \left(\frac{\Delta m_{1,\text{sim}} - \Delta m_1}{\sqrt{2V/N_{\text{tot}}}}\right)^2 + \left(\frac{\Delta V_{\text{sim}} - \Delta V}{\sqrt{2(m_4^C - V^2)/N_{\text{tot}}}}\right)^2 \tag{2}$$

$$\frac{2}{N_{\text{tot}}}\chi^2 = (\Delta A_{\text{sim}} - \Delta A)^2 + \left(\frac{\Delta m_{1,\text{sim}} - \Delta m_1}{\sqrt{V}}\right)^2 + \left(\frac{\Delta V_{\text{sim}} - \Delta V}{\sqrt{m_4^C - V^2}}\right)^2 \tag{3}$$

To assess the method, we will calculate and plot the distribution of $(2/N_{\text{tot}})\chi^2$ (Eq. (3)) for all combinations of $\Delta\mu_a$ in two layers [34,74,76,77]. N_{tot} is a scaling factor, and it is a function of the selected laser intensity and acquisition time. Therefore, the calculated χ^2 is unitless, except for the linear dependence on N_{tot}.

In this study, we did not use the intensity information (ΔA) for determining $\Delta\mu_a$ because it requires careful data processing to account for possible laser drifts and changes in the optical filters. During measurements, the optical filters were adjusted (by rotating the Neutral Density filter) in order to regulate the count rate. Additionally, ΔA is more susceptible to laser drifts than other moments.

We used the developed phantom, which mimics two layers with changing μ_a, for experimentally testing the new method. The method requires knowing the values of all parameters at baseline, which can be obtained for phantom measurements. The refractive index (n) was assumed to be 1.33 for both layers because the main component of the phantom mixture was distilled water. The thickness of the superficial layer (L) was measured with rulers glued to the phantom. To obtain the values of μ_a and μ'_s of each layer, we used measurements on the individual compartments (superficial and deep) and applied the curve-fitting method with the homogeneous model. For experiments involving blood, the targeted optical properties at baseline were the same for both layers, so measurements on a single layer were sufficient to determine the optical properties of both layers.

Although the changes in the first three statistical moments are independent of the IRF, their values are influenced by the chosen time-channels that are used for their computation [43]. We computed moments using the same time-channels for all theoretically obtained and measured DTOFs: from 25% on the rising edge to 3% on the tail of the DTOF that was measured at baseline. Prior to calculations of moments, the theoretically obtained DTOFs were convolved with the IRF that was measured at the start of an experiment.

The new method's computation time for each DTOF is typically a few seconds, which can be reduced with a good initial guess. Therefore, we employed the established method based on moments, which uses sensitivity factors, for obtaining the initial guess of $\Delta\mu_a$ in two layers. We obtained the sensitivity factors by computing the changes in moments resulting from $\pm 2\%$ $\Delta\mu_a$ in each layer, as done in [43].

2.2.3. Calculation of concentrations of oxy- and deoxyhemoglobin

To determine the concentrations of oxyhemoglobin (HbO$_2$) and deoxyhemoglobin (Hb) in experiments involving blood, we used the determined μ_a values at multiple wavelengths and the known molar absorption coefficients (ε) of HbO$_2$ and Hb. We used 9 spectral channels (3rd to 11th out of 16) covering the spectral range from 705 to 805 nm, which is consistent with our previous study with blood-lipid phantoms [70]; the dependence on the choice of wavelengths should be further investigated.

We used the ε spectra provided by Gratzer et al. [78] and the absorption spectra of water provided by Matcher et al. [79]. We calculated the concentrations of only HbO$_2$ and Hb using the μ_a values, which were obtained by subtracting the μ_a of water (multiplied by 0.985, which was the volume fraction of water and SMOFlipid) from the determined μ_a values.

2.3. Phantom setup

2.3.1. Construction of phantom

In recent years, various tissue-mimicking phantoms containing blood have been developed, e.g. [59,62–67]. However, to our knowledge, no presented phantom has two blood-lipid compartments with variable StO$_2$, which could be used to mimic the extra- and intracerebral compartments of the head.

We present a new tissue-mimicking phantom that was built in-house at IBIB PAN. The phantom consists of three containers, as shown in Fig. 1. **The deep container** is similar to the one presented by Kleiser et al. [63] and holds the liquid for the deep compartment. The container has an irregular octagonal shape. Three walls have windows for optodes, which allow three NIRS systems to measure simultaneously, and the fourth wall has a separating window (100 mm × 100 mm). **The superficial container** holds the liquid for the superficial compartment and **the third container** separates this liquid into parts A and B. The superficial container has three walls and the side without a wall attaches to the deep container. The third container is shorter and suspended, which leaves a 25 mm gap underneath for the liquid to flow between parts A and B, as shown in Fig. 1 (b). The thickness of part A can be changed from approximately 0 to 65 mm by

moving the third container. Part B of the superficial compartment allows adding and efficiently mixing ingredients. Measurements can be performed simultaneously on any of the five windows (60 mm × 40 mm) for measuring on different compartments: the deep (Pos. #1), the two-layered medium (Pos. #2), and the superficial (Pos. #3). Below we list the main features of the phantom.
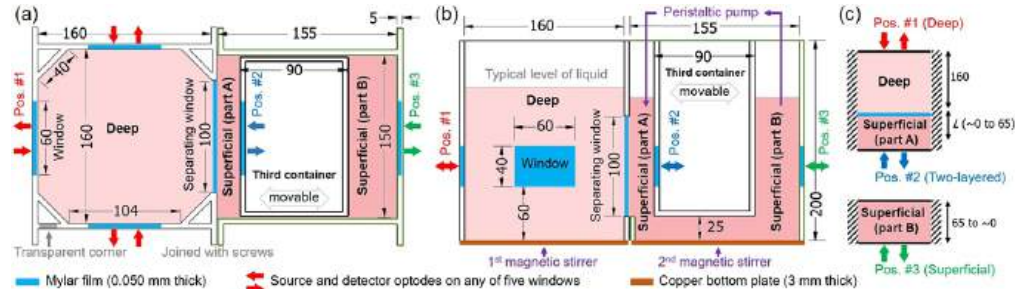

Fig. 1. Diagrams of the phantom showing top view (a) and side view (b), and the corresponding model (c). The three containers are labeled: Deep, Superficial, and Third container, which is movable. Units are mm.

Materials. Five walls have windows for measurements (next to red, blue, and green arrows in Fig. 1) and these walls are made from black PVC (5 mm thick). All other walls and the covering lids are made from transparent PVC (5 mm thick), which allows seeing inside the phantom. To see and measure the height of the liquid in the deep container, one corner was cut out and replaced with transparent PVC, shown in Fig. 1 (a). To prevent ambient light interference during measurements, the entire phantom was covered with a black blanket. The deep and the superficial containers are held together by four screws, which have washers (2 mm thick solid plates cut from PVC), and in-between is a glued water-resistant rubber cord, which gets squeezed to prevent leakage. The bottom parts are made from copper (3 mm thick), which allows using hot plates for controlling the temperature. Each of the five windows (60 × 40 mm) has two latches for holding the optode holders (58 × 38 mm), which were 3D printed (pure black ABS material, Zortrax Z-ABS v2). All windows were covered with translucent Mylar film (0.050 mm thick, 785-0786 RS Pro, UK), which was permanently fixed to the walls using silicone. The effect of a thin, slightly scattering Mylar film on diffuse reflectance measurements can be considered negligible [80]. To limit ambient oxygen diffusion, the two containers were covered with lids, which have openings for fixing a thermometer, an oxygen supply, a peristaltic pump, and for adding ingredients.

Thickness of the superficial layer (*L*). The third container is designed to slide along one direction, which is achieved by four linear bearing guides attached to its top and two linear shafts attached to the top of the other two containers. A threaded rod is attached between the two linear shafts to enable precise movement of the container. Rulers were glued on top of the third and the superficial containers to facilitate measurement of the third container's position and hence *L*. To counteract buoyant forces, heavy objects can be placed inside the third container.

Separating window and bending of Mylar film. To separate mixtures contained in the deep and superficial containers, we covered the separating window (100 mm x 100 mm, as shown in Fig. 1) with Mylar film. When the Mylar film gets wet, it is able to bend easily. To maintain a constant position of the Mylar film, we applied pressure on it by pouring more liquid into the deep container, so that the liquid level was approximately 2 cm higher than in the superficial container. This created a uniform high pressure on the Mylar film, resulting in a constant and repeatable bending. During data analysis, we estimated that the Mylar film bent by approximately 0.5 mm, which we approximated as a flat boundary, given the large area of the separating window.

Stirring and heating. Stirring and heating were accomplished by placing the deep and the superficial containers on top of two hot plates (Stuart US152D, Bibby Sterlin Ltd. and SMP-TC, SET GSM, Poland). In all experiments, the stirring was set at 500 RPM. Additionally, in the superficial container, a peristaltic pump (372.C Elpan, Poland) was used to move the liquid from the top of part B to the top of part A (shown in Fig. 1 (b)) at a flow rate of 500 ml per min through an 8 mm diameter silicone tube. In experiments involving blood, the temperature was maintained at 37 ± 1 °C. To verify the efficacy of stirring, we added ink to either the deep or the superficial container and checked how quickly the measured signals reached new stable values, which typically occurred within about 10 seconds.

Controlled and monitored parameters. In experiments involving blood, the following parameters were controlled and monitored. The temperature in each compartment was recorded every 10 s using two submerged digital thermometers (RC-5+, Elitech). The pH level was kept constant at 7.4 by adding the phosphate-buffered saline powder (PBS powder, sc-24947, ChemCruz). The blood was deoxygenated by adding dry bakery yeast (Drozdze Suszone Instant, Dr. Oetker, Poland). To oxygenate the blood, medical-grade oxygen from a tank was bubbled (3 L/min flow setting on the pressure regulator) through an air stone (Mist-Air, fine bubbles, Kordon) submerged in the deep container. The air stone was held in place by a long rigid plastic tube and positioned in the middle of the deep container, approximately 3 cm above the bottom. Experiments involving ink required controlling only the stirring rate.

Simultaneous NIRS measurements can be performed on up to five windows, i.e. with up to five NIRS systems. If the source-detector distance (ρ) of the optodes fixed on the phantom is 40 mm, then the minimum distance between fibers on different windows is at least 75 mm, as in [63]. Light has a negligible chance of traversing 75 mm if the optical properties of the phantom are similar to those of biological tissue [76].

Boundary conditions. We assumed semi-infinite model with extrapolated boundary conditions. We approximated the deep container as an infinite medium (semi-infinite for measurements on the surface). For $\rho = 40$ mm, the distance from a fiber to the closest neighbouring wall is 60 mm, so the laser light needs to traverse at least 160 mm to reach a neighbouring wall and then a detection fiber bundle. Optodes were attached 75 mm above the ground level and the liquid was filled up to about 150 mm (or 170 mm) above the ground level in the superficial (or deep) container. We assumed that black PVC and black optode holders absorb all light that penetrates the surface. We neglected the effect of the Mylar film [80].

2.3.2. Characterizing ink and SMOFlipid

The use of ink and Intralipid in tissue-simulating phantoms has been studied and described in the literature, e.g. Di Ninni et al. [81,82] and Spinelli et al. [83,84]. In this section, we summarize how we determined the nominal values of μ_a and μ'_s, which we used as a guide for the experimental protocol and later for a comparison with our TD-NIRS results.

We used SMOFlipid 20% (Fresenius Kabi, Poland) as a substitute for Intralipid, which we confirmed has similar μ'_s and μ_a. We calculated the nominal μ'_s of a phantom based on the volume fraction of SMOFlipid [81,84]:

$$\mu'_s = \frac{V_{SL}}{V_{Diluted\ ink} + V_{SL} + V_{water}} \varepsilon'_{s,SL} \tag{4}$$

where $\varepsilon'_{s,SL}$ is the specific reduced scattering coefficient of SMOFlipid. We used the value 21.5 mm^{-1} for 750 nm, which was reported for Intralipid [81,83,84]. $V_{Dilted\ ink}$, V_{SL}, and V_{water} are the volumes of diluted ink, SMOFlipid, and water, respectively.

We characterized the μ_a of ink (Rotring, black, 23 ml, Germany) because it can have large brand-to-brand and batch-to-batch variations [82,84]. We diluted pure ink in distilled water (d_{ink} = weight of ink / total weight), measured its absorbance (A_p) in a 1 cm thick cuvette with

a spectrophotometer, and calculated its effective absorption coefficient ($\varepsilon_{\text{eff,ink}} = A_p / d_{\text{ink}}$). At 750 nm, we obtained $\varepsilon_{\text{eff,ink}} = 626\,\text{mm}^{-1}$, which is consistent with a previously reported value for this brand of ink [82]. We combined the value of $\varepsilon_{\text{eff,ink}}$ obtained from spectrophotometric measurements and the value of the single-scattering albedo (Λ) to predict the value of the specific absorption coefficient of ink ($\varepsilon_{\text{a,ink}}$), as proposed in [84]. By definition, $\Lambda = (\varepsilon_{\text{eff,ink}} - \varepsilon_{\text{a,ink}}) / \varepsilon_{\text{eff,ink}}$ and we used the value of 0.15 for Λ. We calculated the nominal μ_a of a phantom based on the volume fraction of the diluted ink [82,84]:

$$\mu_{a,\text{nominal}} = \mu_{a,\text{water}} + \frac{V_{\text{Diluted ink}}d_{\text{ink}}}{V_{\text{Diluted ink}} + V_{\text{SL}} + V_{\text{water}}}\varepsilon_{\text{eff,ink}}(1 - \Lambda) \tag{5}$$

We made a simplifying assumption that SMOFlipid has the same μ_a as water, since their μ_a are similar and the main constituent of the phantoms in all experiments was water.

2.3.3. Protocol for experiments involving ink

We conducted two experiments involving ink, in which we increased μ_a in either the deep or the superficial compartment. In one compartment, the targeted μ_a values ranged from 0.05 to 0.25 cm^{-1} (at 750 nm) in 20 steps, while in the other compartment, the targeted μ_a was fixed at 0.10 cm^{-1} at 750 nm. The targeted μ'_s was 10.7 cm^{-1} at 750 nm in both compartments. These values of optical properties are within the typical range for tissues [85,86], specifically of the human head [87]. Table 1 lists the targeted amounts of ingredients. To increase μ_a without changing μ'_s, we prepared Mixture #2 (water, diluted ink, and SMOFlipid), which has a much higher μ_a (~ 4.7 cm^{-1}) but the same μ'_s as the mixture in the phantom. We set L to 14.5 mm in both experiments, which were conducted on two consecutive days. We used the TD-NIRS system to measure on the deep compartment (Pos. #1), the two-layered medium (Pos. #2), and/or the superficial compartment (Pos.#3), according to Fig. 1.

Table 1. Ingredients (in grams) and targeted μ_a values (at 750 nm) for the two experiments involving ink. SL is SMOFlipid.

Exp.	Deep container				Superficial container			
	Water	SL	Mixture #2	Targeted μ_a / cm^{-1}	Water	SL	Mixture #2	Targeted μ_a / cm^{-1}
#1	3420	180	17 → 170	0.05 → 0.25	1710	90	27	0.10
#2	-//-	-//-	54	0.10	-//-	-//-	8.5 → 85	0.05 → 0.25

The nominal μ_a values were calculated by using the weights of the added ingredients and Eq. (5). Distilled water and SMOFlipid were weighted with a precision of 0.2 g. For adding Mixture #2, we used a syringe and measured its weight before and after injecting the mixture into the phantom, with a precision of 0.1 µg. We waited at least 40 s for the ingredients to stir before taking NIRS measurements. After adding an ingredient, its measured weight was recorded and used to update the targeted weight of the next ingredient to be added, which helped achieve the targeted μ_a values across the twenty $\Delta\mu_a$ steps.

2.3.4. Protocol for experiments involving blood

We conducted three experiments involving blood using the same protocol, but setting different thickness of the superficial layer L (12, 15, and 17 mm). We used TD-NIRS system to measure on the deep compartment (Pos. #1) and the two-layered medium (Pos. #2). Measurements on the deep compartment allow assessing the repeatability of the experiment, as they are independent of L.

We changed the oxygen saturation (StO$_2$) of blood separately in the superficial and the deep compartments, in one compartment at a time. The targeted μ'_s of both compartments was 10.7 cm^{-1} at 750 nm. Table 2 lists the protocol steps along with the targeted StO$_2$. Table 3 lists

the targeted amounts of ingredients. The preparation of the phantom before starting TD-NIRS measurements comprised of six steps (P1 to P6). After step P6, the deep compartment contained 3366 g of distilled water with PBS and 180 g of SMOFlipid, as in Table 3. In step S1, we added human erythrocyte concentrate to each compartment. We used a syringe with 1.6 mm inner diameter for handling blood-containing mixtures. In step S2, we took some of the mixture (approximately 40 ml) from the deep compartment, mixed yeast in it, and poured it back into the deep compartment. We denoted this as time zero (Time = 0 min). In step S3, we bubbled oxygen in the deep compartment for 2 min. In step S4, we added yeast to the superficial compartment using a similar procedure as was used for adding yeast to the deep compartment. Then, we repeated step S3 three times (steps S5, S6, and S7). The protocol consisted of six deoxygenation cycles: one in the superficial compartment and five in the deep compartment. These cycles are indicated by six arrows at the top of figures that show time traces of the TD-NIRS results.

Table 2. Protocol steps and the targeted StO$_2$ in two compartments for the three experiments involving blood.

Step	Time/min	Description	Targeted StO$_2$ / %	
			Deep	Superficial
P1		Turn on the laser and let it warm up for at least 1 hour		
P2		Assemble three containers and add water with PBS to both compartments		
P3		Start stirring and heating, and attach two thermometers		
P4		Remove air bubbles in both compartments by tapping with a long metal rod		
P5		Add SMOFlipid to both compartments, which makes them opaque		
P6		Measure IRF and then start measuring on the phantom		
S1		Add blood to each compartment	~100	~100
S2	0	Add yeast to the Deep compartment		
		Wait 13 min until plateau (cycle #1)	100 → 0	
S3	13–15	Oxygenate the Deep compartment	0 → 100	
		Wait 15 min until plateau (cycle #2)	100 → 0	
S4	31	Add yeast to the Superficial compartment		
		Wait 15 min until plateau (cycle #3)		100 → 0
S5	45–47	Oxygenate the Deep compartment	0 → 100	
		Wait 13 min until plateau (cycle #4)	100 → 0	
S6	60–62	Oxygenate the Deep compartment	0 → 100	
		Wait 15 min until plateau (cycle #5)	100 → 0	
S7	77–79	Oxygenate the Deep compartment	0 → 100	
		Wait 13 min until plateau (cycle #6)	100 → 0	

Table 3. Ingredients for each of the three experiments involving blood. SL is SMOFlipid.

Container	PBS (water) after step P2	SL after step P5	Blood after step S1	Yeast after steps S2 and S4	Total (excluding yeast)
Deep	3366 g	180 g	54 g	5.4 g	3600 g
Superficial	1683 g	90 g	27 g	2.7 g	1800g
Percentage	93.5%	5%	1.5%	0.1%	100%

   The three experiments were conducted on different days. The first experiment (Exp. #1, $L = 12$ mm) and third experiment (Exp. #3, $L = 17$ mm) used blood from the same blood transfusion bag. The second experiment (Exp. #2, $L = 15$ mm) used another blood transfusion bag.

3. Results

3.1. Method for determining $\Delta\mu_a$ in two layers

Here we examine the proposed method for determining $\Delta\mu_a$ in two layers. We calculated the values of ΔA, Δm_1, and ΔV for all combinations of $\Delta\mu_{a,Sup}$ and $\Delta\mu_{a,Deep}$, and the results are presented in Fig. 2 (a), where the changes in each statistical moment are shown using contour lines. The lines of all pairs of two moments intersect only once, which confirms that there is a unique solution of $\Delta\mu_{a,Sup}$ and $\Delta\mu_{a,Deep}$ when changes of any two moments are analyzed. The slopes of such lines (changes in moments versus $\Delta\mu_{a,Sup}$ and $\Delta\mu_{a,Deep}$) are related to depth selectivity [48,88], which is a metric that reflects the sensitivity of a measurand to $\Delta\mu_{a,Deep}$ in relation to $\Delta\mu_{a,Sup}$. The lines for ΔA are more vertical, indicating that ΔA is more sensitive to $\Delta\mu_{a,Sup}$ compared to $\Delta\mu_{a,Deep}$, i.e. ΔA has low depth selectivity. The lines become more horizontal for higher-order moments, corresponding to increased depth selectivity, which is a well-known property of moments [48,88]. For small values of $\Delta\mu_a$, the lines for all moments be approximated as linear functions. However, for larger values of $\Delta\mu_a$, the lines become increasingly nonlinear, confirming the need for using the LMA, i.e. solving a nonlinear problem of determining $\Delta\mu_a$ in multiple layers using changes in moments.
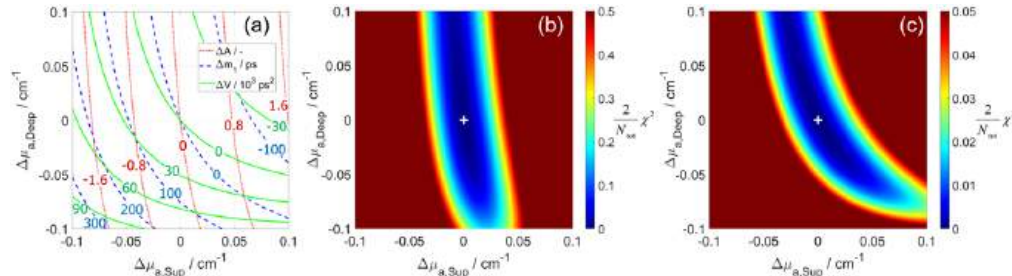

Fig. 2. Changes in moments (ΔA, Δm_1, and ΔV) for all combinations of $\Delta\mu_{a,Sup}$ and $\Delta\mu_{a,Deep}$ (a). Error norm (χ^2) for all combinations of $\Delta\mu_{a,Sup}$ and $\Delta\mu_{a,Deep}$ (white cross marks true values) when using changes in three moments (b) or using only Δm_1 and ΔV (c). Baseline parameters are $\mu_{a,Sup} = \mu_{a,Deep} = 0.13\,cm^{-1}$, $\mu'_s = 10\,cm^{-1}$, $L = 12\,mm$, and $n = 1.33$.

We calculated the error norm (χ^2) using Eq. (3) for all combinations of $\Delta\mu_{a,Sup}$ and $\Delta\mu_{a,Deep}$. The distribution of χ^2 is shown in Fig. 2 (b) when all three moments are considered and in Fig. 2 (c) when excluding the term with ΔA, i.e. using only the terms containing Δm_1 and ΔV in Eq. (3). The presented χ^2 distributions have a single minimum, i.e. no local minima, confirming the suitability of the LMA approach for finding this minimum. We verified that the LMA reaches the same solution (determined $\Delta\mu_a$ in two layers) regardless of the initial guess.

The shape of the χ^2 distribution depends on which moments are used and the weights assigned to them. When three moments are used (Fig. 2 (b)), the contribution from ΔA dominates, resulting in a χ^2 distribution that is more dependent on the superficial layer compared to the deep layer. This distribution resembles the line where $\Delta A = 0$ in Fig. 2 (a). When the term with ΔA is excluded (Fig. 2 (c)), the contribution from Δm_1 becomes dominant, and the shape of the resulting χ^2 distribution resembles the line where $\Delta m_1 = 0$ in Fig. 2 (a). These results are consistent with the differences in magnitudes of the contrast-to-noise ratio (CNR), e.g. reported in [88] where a 15% increase in $\mu_{a,Sup}$ resulted in a CNR of about 100 for ΔN_{tot}, 30 for Δm_1, and 10 for ΔV. Therefore, for a typical $\Delta\mu_a$, the term with ΔA in Eq. (3) contributes much more to the value of χ^2 than the term with Δm_1, which is consistent with the one-order magnitude difference in the colorbars for χ^2 in Fig. 2 (b) and (c). If only a single moment is considered in Eq. (3), the

shape of the χ^2 distribution would follow the moment's zero contour line shown in Fig. 2 (a) and the value of χ^2 would be zero along this line, resulting in a lack of a single minimum.

We examined the impact of an error in the value of a baseline parameter on the determined $\Delta\mu_a$ and the results are presented in Fig. 3. We simulated two DTOFs (at baseline and after $\Delta\mu_{a,Deep} = 0.05\,\text{cm}^{-1}$) and retrieved $\Delta\mu_{a,Sup}$ and $\Delta\mu_{a,Deep}$ but using different assumed values for one of the baseline parameters: μ_a, μ'_s, and n in the superficial or the deep compartment, as well as L. The findings depend on the chosen ground truth values of all parameters (for both simulated DTOFs), but the results in Fig. 3 are a representative example. Figure 3 (b) shows that $\mu'_{s,Deep}$ has little effect on TD-NIRS signals, which was also found in previous studies [89]. Figure 3 (a, b) demonstrates that an error in the assumed value of $\mu_{a,Sup}$ has an opposite effect on the determined values of $\Delta\mu_a$, compared to an error in the assumed value of $\mu'_{s,Sup}$. This agrees with the general understanding that these parameters (μ_a and μ'_s) have contrasting impacts on the shape of the DTOF [74]. Errors in $\mu'_{s,Sup}$ and n_{Sup} have similar effects (Fig. 3 (b, c)), which is expected as both impact how quickly light passes through a medium. The determined $\Delta\mu_{a,Sup}$ is minimally affected by L (Fig. 3 (d)). However, when L is underestimated (or overestimated), then the determined $\Delta\mu_{a,Deep}$ approaches (or moves away from) the true value of $\Delta\mu_{a,Sup}$. This dependence on L remained consistent when using ground truth values of $\Delta\mu_{a,Sup} = 0.05\,\text{cm}^{-1}$ and $\Delta\mu_{a,Deep} = 0$.
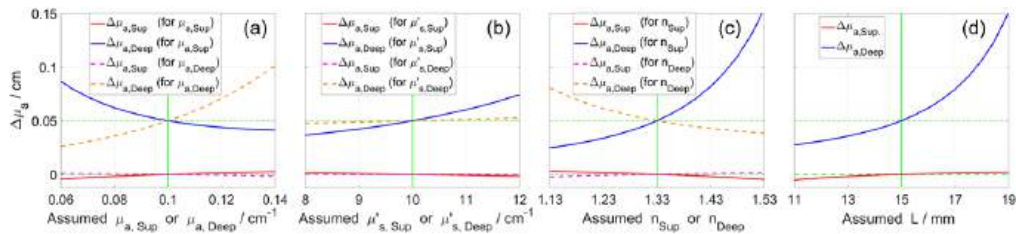

Fig. 3. Determined $\Delta\mu_{a,Sup}$ and $\Delta\mu_{a,Deep}$ for different assumed values of baseline parameters: μ_a (a), μ'_s (b), n (c), and L (d). Green lines mark true values: $\Delta\mu_{a,Sup} = 0$ and $\Delta\mu_{a,Deep} = 0.05\,\text{cm}^{-1}$, $\mu_a = 0.1\,\text{cm}^{-1}$, $\mu'_s = 10\,\text{cm}^{-1}$, $L = 15$ mm, and $n = 1.33$.

3.2. Experiments involving ink

Figure 4 (a) shows the determined μ_a for two experiments involving ink, for all wavelengths, for both compartments, for three $\Delta\mu_a$ steps. The μ_a values for both experiments are similar and consistent with the targeted μ_a values in Table 1, which demonstrates good control and repeatability of experiments. The spectral shape of μ_a for the smallest nominal μ_a resembles the shape of the μ_a of water. For the spectral shape of μ'_s, please refer to Fig. 8 (b).

Figure 4 (b) shows the determined μ'_s values for 20 $\Delta\mu_a$ steps in the deep compartment in Exp. #1, at different wavelengths. For both experiments, the μ'_s sometimes slightly increase with μ_a, especially for the first few (about four) $\Delta\mu_a$ steps. However, for most wavelengths, the values of μ'_s changed by less than approximately $0.3\,\text{cm}^{-1}$ (less than 3%), following a $0.20\,\text{cm}^{-1}$ (500%) increase in μ_a. One cause may be the coupling of $\Delta\mu_a$ to $\Delta\mu'_s$, which we previously reported for our system [70] by measuring on a well-characterized array of solid homogeneous phantoms that have the same μ'_s (either 5, 10, 15, or $20\,\text{cm}^{-1}$) and different μ_a values (ranging from 0 to $0.35\,\text{cm}^{-1}$) [55], as part of the BitMap campaign [52]. For a comparison of the coupling with other systems, see [52]. Other causes for changes in μ'_s could be, e.g. possible timing drifts in the laser output. Increasing the concentration of ink should not have influenced the μ'_s because we used Mixture #2 (containing water, SMOFlipid, and ink) that had the same μ'_s as the phantom but much higher μ_a (refer to section 2.3.3).
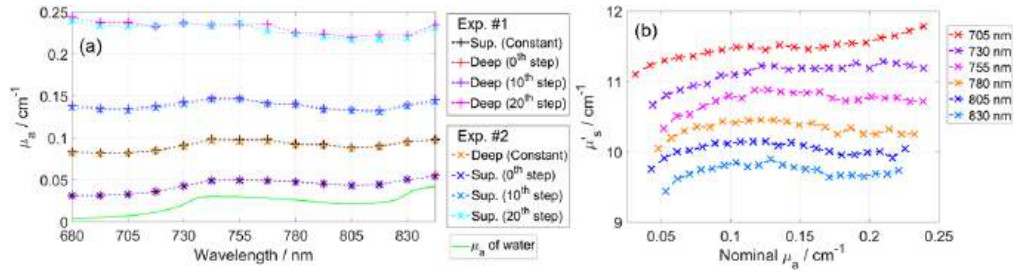
Fig. 4. (a) Determined μ_a for two experiments involving ink, for three nominal μ_a (0.05, 0.15, and 0.25 cm^{-1} at 750 nm). (b) Determined μ'_s for 20 $\Delta\mu_a$ steps for Exp. #1. Results were obtained using measurements on each compartment (Pos. #1 or #3 in Fig. 1), analyzed using the curve-fitting method with a homogeneous model.

Figures 5 and 6 present results at 768 nm (8th spectral channel) and similar results were obtained at other wavelengths. Figure 5 (a) shows the normalized IRFs and DTOFs for the two source-detector pairs located on Pos. #1 and #2, when the targeted μ_a was 0.10 cm^{-1} at 750 nm in both compartments. The two source-detector pairs had similar IRFs and hence similar DTOFs. The total number of photons in the DTOF (N_{tot}) was between approximately 5.4 to 0.5 million photons at 768 nm for different $\Delta\mu_a$ steps, with lower values of N_{tot} at higher μ_a.
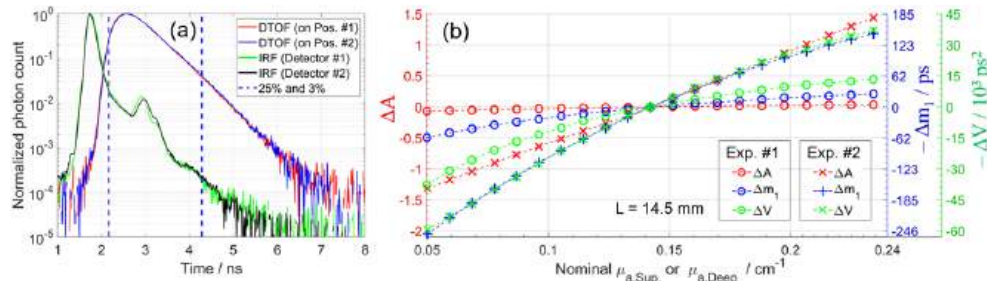

Fig. 5. (a) Normalized IRFs and DTOFs (when targeted $\mu_a = 0.10$ cm^{-1} at 750 nm in both compartments), for two source-detector pairs on Pos. #1 and #2, at 768 nm. (b) Changes in moments (ΔA, Δm_1, and ΔV) for 20 $\Delta\mu_a$ steps, measured on Pos. #2 (two-layered), at 768 nm.

Figure 5 (b) shows the changes in moments (ΔA, Δm_1, and ΔV) resulting from 20 $\Delta\mu_a$ steps. The baseline was selected as the middle measurement (10th $\Delta\mu_a$ step, when the targeted $\mu_a = 0.15$ cm^{-1} at 750 nm). All moments show high contrast to $\Delta\mu_{a,Sup}$ and much lower contrast to $\Delta\mu_{a,Deep}$, which is related to the large L (14.5 mm). The contrast to $\Delta\mu_{a,Deep}$ (and hence depth selectivity) increases for higher-order moments, consistent with the results in Fig. 2 (a). Notably, ΔA appears to be close to zero even for the largest $\Delta\mu_{a,Deep}$. However, to assess a measurand's capabilities of detecting $\Delta\mu_a$, it is essential to consider also the contrast-to-noise ratio (CNR) [48,88].

Figure 6 presents the determined μ_a for 20 $\Delta\mu_a$ steps for the two experiments involving ink. One source-detector pair was used to measure on the compartment in which μ_a was changed: the deep compartment for Exp. #1 and the superficial compartment for Exp. #2. These measurements were analyzed with the curve-fitting method (homogeneous model) to determine μ_a and μ'_s. The determined μ_a values (black crosses in Fig. 6) are close to the nominal μ_a values (the identity line) for all 20 $\Delta\mu_a$ steps and for both experiments. The signal level (i.e. N_{tot}) decreased for higher μ_a, leading to increased noise, which could be the reason for the slight discrepancies for higher μ_a. For measurements on a two-layered medium (Pos. #2), the curve-fitting method
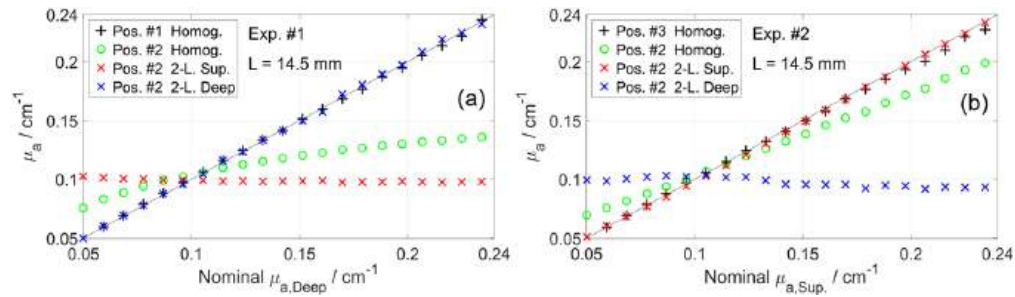
Fig. 6. Determined μ_a for 20 $\Delta\mu_a$ steps in first (a) and second (b) experiments involving ink, at 768 nm. Measurements on a compartment with increasing μ_a (Pos. #1 or Pos. #3) were analyzed using the curve-fitting method with a homogeneous model (black crosses). Measurements on two-layered medium (Pos. #2) were analyzed using the same method (green circles) and the method based on changes in moments with a two-layered model (red and blue crosses).

(homogeneous model) provided μ_a values (green circles in Fig. 6) that were between the μ_a values of the two compartments and closer to the superficial compartment's μ_a. This highlights the need for a two-layered model when measuring on a two-layered medium. We applied the proposed method based on the changes in moments to determine $\Delta\mu_{a,Sup}$ and $\Delta\mu_{a,Deep}$, and added to them the baseline μ_a values. The resulting values of $\mu_{a,Sup}$ and $\mu_{a,Deep}$ (red and blue crosses in Fig. 6) are close to the nominal values for all 20 $\Delta\mu_a$ steps. These results are comparable to the results of similar experiments that were reported in e.g. [33,36,43]. Possible drifts in the laser output could affect the moments, which may account for the slight deviations from a horizontal line for the determined $\mu_{a,Deep}$ in Exp. #2 (blue crosses in Fig. 6 (b)). Another cause could be the μ'_s changes shown in Fig. 4 (b), which can affect only the results for the deep layer in Exp. 2, based on the findings in Fig. 3 (b).

3.3. Experiments involving blood

In this section we present the results of the three experiments involving blood. The results are presented in the order according to the data analysis: the measured DTOFs and the calculated changes in moments (Fig. 7), the determined μ_a and μ'_s (Figs. 8 to 10), the determined concentrations of HbO$_2$ and Hb (Fig. 11), and finally the determined StO$_2$ (Figs. 12 and 13).
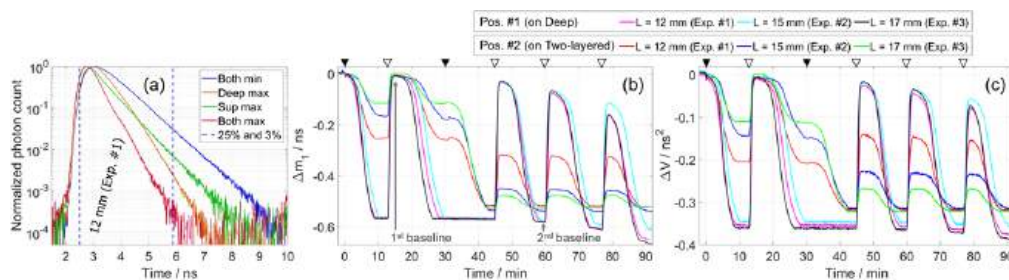

Fig. 7. (a) DTOFs measured on Pos. #2 at different μ_a in two compartments, at 705 nm. Changes in moments, Δm_1 (b) and ΔV (c), measured on Pos. #1 and #2, for three experiments involving blood. Filled triangles indicate when yeast was added, separately in deep and superficial compartments, and hollow triangles denote the start of bubbling oxygen in the deep compartment (these triangles are also shown in Figs. 9 to 12).

Figure 7 (a) shows DTOFs measured on Pos. #2, at different StO_2 values in the two compartments, at 705 nm for which $\Delta\mu_a$ is high. The $\Delta\mu_a$ due to changes in StO_2 depends on the difference of the molar absorption coefficients (shown in Fig. 8 (a)). For example, close to the isosbestic point, e.g. at 808 nm, $\Delta\mu_a$ is close to zero. An increase in μ_a in any layer results in a narrower DTOF, i.e. the curve after the peak decreases at a faster rate. Sato et al. [90] used the slopes of the segments along the time axis to selectively determine the μ_a of different layers. The four DTOFs in Fig. 7 (a) support and demonstrate this concept. When only $\mu_{a,Sup}$ is increased (green curve), the slope of the curve at earlier time-channels changes, while the slope at the later time-channels (from about 4 ns) appears unchanged. When only $\mu_{a,deep}$ is increased (orange curve), the slope of the curve at later time-channels (from about 4 ns) is affected more compared to earlier time channels. The arrival time of photons is related to the mean penetration depth, and this leads to a relationship between μ_a at different depths and the slope of the DTOF at different times, as explained in [90]. When μ_a of both compartments is maximum (red curve), the curve has a small bump at about 4 ns (about 1 ns after the DTOF's maximum). This bump is caused by the after-pulse peak in the IRF, which occurs about 1 ns after the IRF's maximum and has a magnitude of about 1% of the IRF's maximum, as shown in Fig. 5 (a).

Figure 7 (b, c) shows the time traces of changes in moments (Δm_1 and ΔV) relative to time zero, for measurements on Pos. #1 and Pos. #2, at 705 nm for which $\Delta\mu_a$ is high. We found that the shape of the IRF did not vary between different experiments (on different days) and the IRF shifted by less than half of a time-channel (one time-channel was 12.22 ps). Therefore, we used the same time-channels for calculating moments for all three experiments, from 25% to 3% of the maximum as shown in Fig. 7 (a). The time trace of ΔA is not shown as it was not used in data analysis and it required correction for changes in the ND filter, which we changed to obtain good signals at high μ_a and avoid oversaturating detectors at low μ_a.

The measurements on the deep compartment demonstrate the repeatability of the experiment, as they are independent of L. Noticeably, the rate of desaturation was slightly different in each experiment. For smaller L, the changes measured on the two-layered medium approach those measured on the deep compartment, as expected. By comparing the relative magnitudes of Δm_1 and ΔV for the two measurement positions, we can confirm that ΔV has a higher depth selectivity [48,88]. When both compartments were desaturated (e.g. at around 43 min), we expect the same changes in moments for measurements on both windows. The observed differences may be due to different μ'_s in the two compartments (shown in Fig. 10), which was caused by the addition of yeast as visible at 0 and 31 min in Fig. 7 (b, c) and Fig. 10. The values of m_1 and V remained stable until the fourth deoxygenation cycle, after which they gradually decreased following a drift in μ'_s (Fig. 10).

Figure 8 shows the determined μ_a and μ'_s spectra for the deep compartment at maximum and minimum StO_2, i.e. at first and second baselines, respectively, which are indicated in Fig. 7 (b).
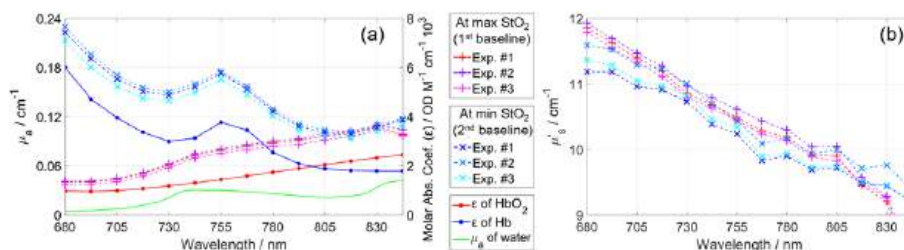

Fig. 8. Determined μ_a (a) and μ'_s (b) at maximum and minimum StO_2 for three experiments involving blood, measured on the deep compartment. The molar absorption coefficients (ε) [78] and the μ_a of water [79] were used for calculating the concentrations of HbO_2 and Hb.

We chose two baseline regions, relative to which the changes in moments will later be calculated for determining $\Delta\mu_a$, so that changes in StO_2 occurred in only one compartment at a time. The first chosen baseline region is from 14.6 to 15.6 min, when StO_2 was close to 100% in both compartments. The second region is from 58.8 to 59.8 min, which is after both compartments were fully deoxygenated. We used the second baseline for analyzing measurements after 31 min, which is after yeast was added to the superficial compartment. The μ_a spectra (Fig. 8 (a)) resemble the shapes of the molar absorption spectra (ε) of HbO_2 and Hb. The differences are mainly due to the contribution of water's μ_a, which should be subtracted from the determined μ_a values for calculating concentrations. The μ'_s values (Fig. 8 (b)) decrease with wavelength, similar to the trend observed for Intralipid [81,84] and tissues [85,86]. The values of μ_a and μ'_s were well-repeatable for the three experiments.

Figure 9 shows the time traces of the determined μ_a, which were obtained for two measurement positions and two methods of data analysis. The μ_a of the deep compartment (black curve) demonstrate five repeatable deoxygenation cycles, with no significant differences between the three experiments. However, after the fourth deoxygenation cycle (after 45 min), the μ_a slightly drifts upwards over time, as evidenced by the increasing minimum μ_a of different deoxygenation cycles, while μ'_s drifts downwards (Fig. 10). The maximum μ_a values (e.g. at around 30 min) differ for each experiment, with values of approximately 0.167, 0.173, and 0.158 cm^{-1} for Exp. #1, #2, and #3, respectively. The noise level expectedly increases for higher μ_a values, due to the lower count rate.
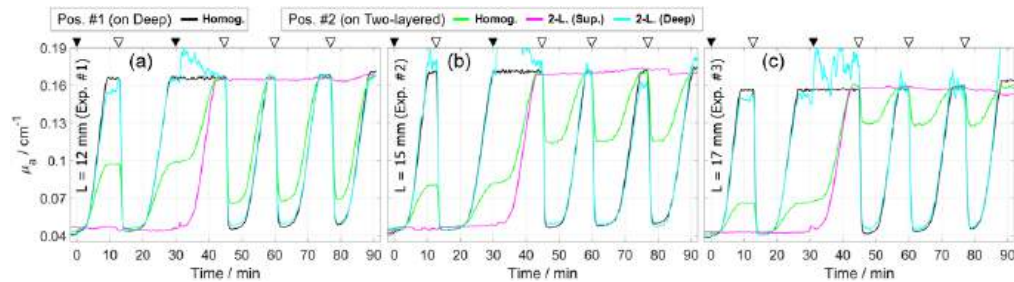

Fig. 9. Determined μ_a at 705 nm in first (a), second (b), and third (c) experiments involving blood. Measurements were analyzed using the curve-fitting method with a homogeneous model (Homog.) and using the changes in moments with a two-layered model (2-L). For visualization, a moving average window (10 data points) was applied to all curves. Triangles at the top are explained in caption of Fig. 7.

The comparison between the results obtained using the two methods (shown in Fig. 9) is consistent with the findings from the experiments involving ink (shown in Fig. 6). Analyzing the measurements on Pos. #2 using the curve-fitting method with a homogeneous model (green curves), produced μ_a values that are between the μ_a of the two compartments, and closer to the μ_a of the superficial compartment for larger L. The method based on moments accurately determined $\Delta\mu_{a,Sup}$ and $\Delta\mu_{a,Deep}$ (magenta and cyan curves) in all cycles except the third cycle (between 31 and 45 min). The accuracy of determined $\Delta\mu_{a,Deep}$ (cyan curve) can be evaluated by comparing to the measurements on the deep compartment (black curve), and the accuracy of $\Delta\mu_{a,Sup}$ (magenta curve) can be assessed based on the protocol, i.e. it was constant except during the third cycle. In the third cycle, the method does not account for $\Delta\mu'_{s,Sup}$ caused by the yeast added at 31 min, which resulted in inaccurately determined $\Delta\mu_{a,Sup}$ and especially $\Delta\mu_{a,Deep}$. The method is insensitive to small changes in $\mu'_{s,Deep}$, but sensitive to $\mu'_{s,Sup}$, as demonstrated in Fig. 3 (b).

Figure 10 shows the time traces of the μ'_s, which were determined together with μ_a (black and green curves in Fig. 9) using the curve-fitting method with a homogeneous model. The μ'_s

measured on the deep compartment were stable up to the fourth cycle (45 min) and then began to decrease. This trend was observed for all wavelengths and in all three experiments. The trend is more similar between Exp. #1 and #3. Adding yeast at 0 min increased μ'_s by approximately $0.3\,\text{cm}^{-1}$ in all three experiments.
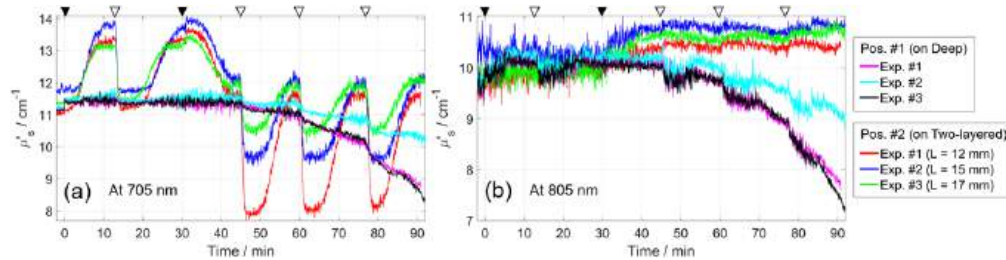

Fig. 10. Reduced scattering coefficient μ'_s in three experiments involving blood, at 705 nm (a) and 805 nm (b). Measurements were analyzed using the curve-fitting method with a homogeneous model and the corresponding determined μ_a values are black and green curves in Fig. 9. Triangles at the top are explained in caption of Fig. 7.

The μ'_s values obtained from measurements on the two-layered medium (analyzed with a homogeneous model, which is suitable only when $\mu_{a,\text{Sup}} = \mu_{a,\text{Deep}}$) are overestimated in the first three deoxygenation cycles (until 45 min, when $\mu_{a,\text{Sup}} \le \mu_{a,\text{Deep}}$ as shown in Fig. 9) and then underestimated in the last three cycles (after 45 min, when $\mu_{a,\text{Sup}} \ge \mu_{a,\text{Deep}}$). This is a consequence of utilizing a homogeneous model for the analysis of measurements on a two-layered medium. Adding yeast at 31 min increased μ'_s by approximately $0.2\,\text{cm}^{-1}$.

Figure 11 shows the time traces of the concentrations of HbO_2 and Hb in the deep compartment (left column) and in the superficial compartment (right column), which were calculated using the determined μ_a at multiple wavelengths (shown in Fig. 9 for one wavelength). The results for measurements on Pos. #1, analyzed using the curve-fitting method with a homogeneous model (red and blue curves in the left panels), are consistent with the expected time traces of the concentrations based on the protocol used. In particular, during each deoxygenation cycle, all (or most) of HbO_2 loses oxygen and becomes Hb (due to yeast consuming oxygen), while the total hemoglobin remains constant (traces of total hemoglobin are not shown). Then, bubbling oxygen results in all (or most) of Hb gaining oxygen and becoming HbO_2 again. The total concentrations differ slightly for the three experiments, following the differences in the maximum of μ_a shown in Fig. 9. In the case of Pos. #2, analyzing the measurements using the curve-fitting method with a homogeneous model (red and blue curves in the right panels), provided concentrations of HbO_2 and Hb that are between those of the two compartments and closer to the superficial compartment for larger L.

The concentrations obtained for the method based on moments with a two-layered model are consistent with the expected time traces based on the protocol. The concentrations for the deep compartment (magenta and cyan curves in the left panels) are similar to those obtained using measurements on Pos. #1 (red and blue curves). The concentrations for the superficial compartment (magenta and cyan curves in the right panels) are relatively constant during five cycles and change during the third cycle, as expected based on the protocol. The addition of yeast to the superficial compartment at 31 min had a clear influence on the determined concentrations. Negative values were obtained for HbO_2 in the deep compartment when the determined $\mu_{a,\text{Deep}}$ had the highest error during the third cycle. Larger L lead to noisier results for the deep compartment and less noisy results for the superficial compartment.
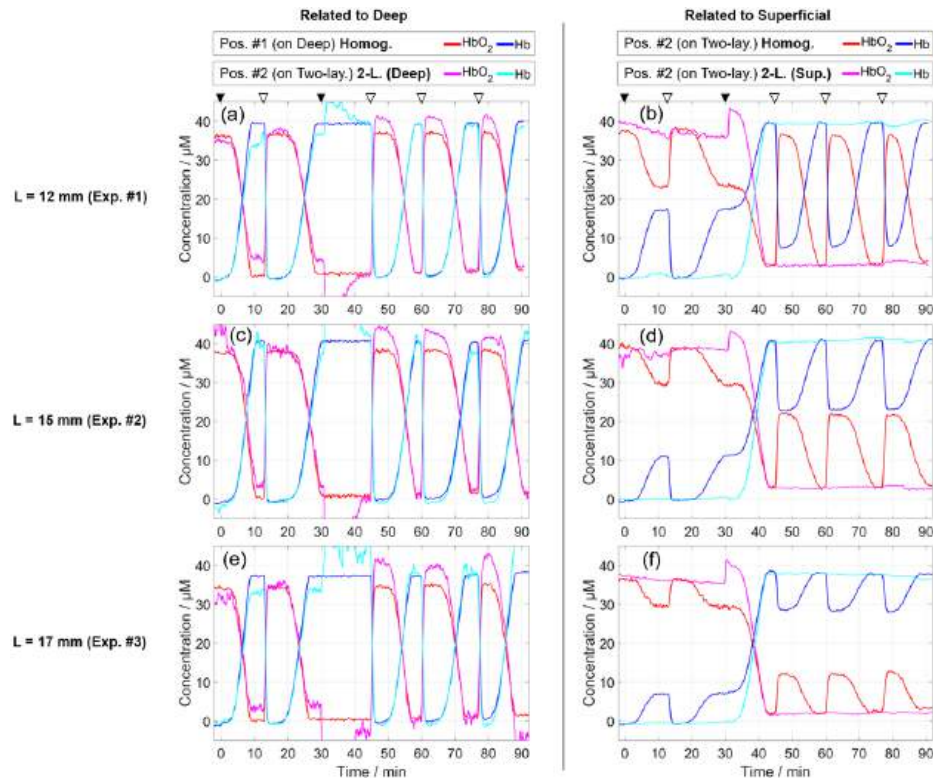
Fig. 11. Concentrations of HbO_2 and Hb in three experiments (three rows) involving blood. Curve-fitting method (Homog.) was used for measurements on Pos. #1 and on Pos. #2, and the latter was also analyzed with method based on moments (2-L. Deep and 2-L. Sup). For visualization, a moving average window (10 data points) was applied to all curves. Triangles at the top are explained in caption of Fig. 7.

The obtained results for HbO_2 are noisier than for Hb for both data analysis methods. The reason is the higher values of ε of Hb compared to ε of HbO_2 at most of the used wavelengths, visible in Fig. 8 (a). A change in Hb has a larger effect on μ_a than an equivalent change in HbO_2.

Figure 12 shows the time traces of StO_2, which were calculated using the concentrations in Fig. 11 and the formula $StO_2 = C_{HbO2} / (C_{HbO2} + C_{Hb})$, where C stands for concentration. Most StO_2 values are between 0 and 100%, except in the third cycle where negative values of C_{HbO2} were obtained resulting in negative values of StO_2. The StO_2 in the deep compartment (black curve) follows five deoxygenation cycles from about 100% to 0%, as expected, but the maximum StO_2 slightly reduces with each deoxygenation cycle in all three experiments. The StO_2 values obtained from Pos. #2, analyzed with a homogeneous model (green curve), are between the StO_2 values of the two compartments and approach the StO_2 of superficial compartment for larger L.

The StO_2 for the superficial compartment obtained from the two-layered measurements (magenta curve) is maximum for the first two cycles and minimum after the third cycle, which follows the protocol. The StO_2 for the deep compartment (cyan curve) closely resembles the results of measurements on the deep compartment (black curve). However, the values deviate for some of the larger changes in StO_2 relative to the baseline and more so for larger L.

The curves of StO_2 in Fig. 12 resemble the curves of μ_a in Fig. 9, which is expected since StO_2 calculation was based on these μ_a values along with the μ_a values at other wavelengths.
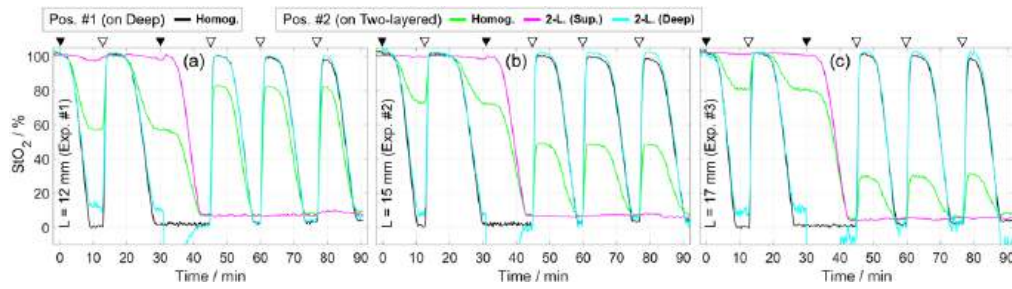
Fig. 12. Determined StO$_2$ in first (a), second (b), and third (c) experiments involving blood for two measurements and two methods of data analysis. The concentrations corresponding to the four StO$_2$ curves are shown in Fig. 11. A moving average window (10 data points) was applied to all curves. Triangles at the top are explained in caption of Fig. 7.

Figure 13 shows a comparison of the determined StO$_2$ values for measurements on the deep compartment and on the two-layered medium. The StO$_2$ curves (shown in Fig. 12) were smoothed using a moving average window (10 data points), which facilitated plotting curves in Fig. 13 rather than scattered data points. We compared the determined StO$_2$ values during five deoxygenation cycles, between the maximum StO$_2$ (after bubbling oxygen) and the minimum StO$_2$ (plateau at the end of desaturation). The third cycle was excluded from this comparison because the StO$_2$ in the deep compartment was constant throughout the cycle. This method of comparing simultaneous NIRS measurements was previously applied by Kleiser et al. [63,64] and in other studies [70]. The results show that the two methods produced agreeing values of StO$_2$ throughout all cycles, as the curves are close to the identity line. However, in the first two cycles, the results obtained at low StO$_2$ (i.e. furthest away from the baseline StO$_2$ of approximately 100%) are noisiest and in part deviate from the identity line. In the last three cycles, the agreement is good at all StO$_2$ values. The results for the deep compartment for measurements on the two-layered medium are noisier for larger L (as expected) and at lower StO$_2$ (which corresponds to higher μ_a for most of the used wavelengths).
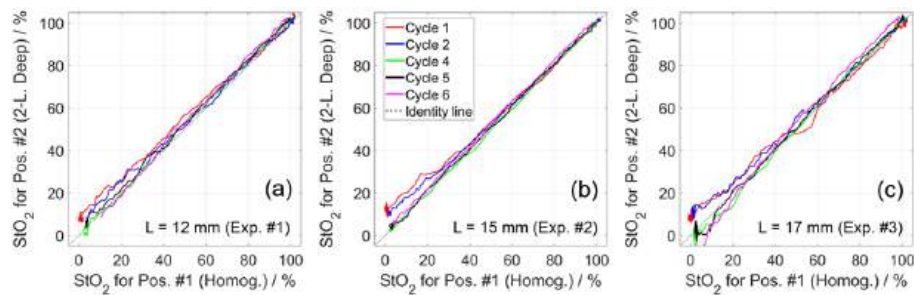

Fig. 13. Comparison of StO$_2$ time traces (from Fig. 12) for first (a), second (b), and third (c) experiments involving blood. Measurements on deep compartment were analyzed using curve-fitting method with homogeneous model (plotted along x-axis). Measurements on two-layered medium were analyzed using method based on moments with two-layered model (along y-axis).

4. Discussion

This work has three main parts: (i) a new method for determining even large $\Delta\mu_a$ in multiple layers, (ii) a new two-layered blood-lipid phantom, and (iii) the published MATLAB codes together with

the measured TD-NIRS data for two experiments involving ink and three experiments involving blood.

4.1.　New method

Previous implementations of analysis based on changes in moments for determining $\Delta\mu_a$ were limited to a range of $\Delta\mu_a$ within which the linearity assumption is valid. Therefore, they were suitable only for fNIRS applications, where small $\Delta\mu_a$ are measured. Figures 2 (a) and 5 (b) show the changes in moments for a range of $\Delta\mu_a$ values, demonstrating the progressive deviation from linearity as the magnitude of $\Delta\mu_a$ increases. In this study, we have experimentally tested the proposed method's capability to accurately determine also large $\Delta\mu_a$ in two layers, i.e. in two compartments of the phantom. The method can now be applied also to NIRS applications that require obtaining absolute μ_a, e.g. for determining StO$_2$. In well-controlled experiments involving ink, we tested the method's accuracy in determining 20 $\Delta\mu_a$ steps (up to $\pm 0.10\,\mathrm{cm}^{-1}$) in the deep or the superficial compartment. The experiments involving blood demonstrated the ability to determine StO$_2$ in two layers during dynamic StO$_2$ changes. For methods that are capable of determining only small $\Delta\mu_a$, the baseline optical properties had to be updated after a $\Delta\mu_a$ step to satisfy the linearity assumption for determining the next $\Delta\mu_a$ [43]. However, the new method removes the restriction on the range of $\Delta\mu_a$ values that can be accurately determined. Another advantageous feature of the method is its low sensitivity to the selected range of time channels used in the calculations. This is a consequence of using the same range for computing the moments of both the measured DTOF and the simulated DTOF convolved with IRF. In contrast, other methods that utilize moments [75] or changes in moments [41] suffer from errors caused by the limited integration range. These errors are sensitive to the selected range of time channels, as explained by Jelzow et al. [43].

The proposed method requires knowing the baseline optical properties, which we obtained by measuring on each compartment of the phantom separately and using the curve-fitting method with the homogeneous model. However, for analyzing *in-vivo* measurements, it remains a challenge to develop an accurate and robust approach for estimating the baseline optical properties of two layers as well as thickness *L*, e.g. [28,33–36]. It can be particularly challenging to estimate *L* using a single DTOF, e.g. if the optical properties of both layers are the same, then any value of *L* will fit the data, i.e. the DTOF. We demonstrated in Fig. 2 (a) that for obtained changes in two moments, there is a unique solution of $\Delta\mu_a$ in two layers. In fNIRS applications (small $\Delta\mu_a$), it is sufficient to know approximate values of the baseline parameters (supported by Fig. 3). This is consistent with the established method based on moments, which requires estimates of the values of all baseline parameters for generating sensitivity factors [41]. However, the estimation of *L* and baseline optical properties is an important and needed topic for further research.

The accuracy of generating the theoretical DTOFs governs the accuracy of the recovered optical properties. One way to enhance the accuracy of theoretical DTOFs is by using Monte Carlo simulations, which is considered as the gold-standard method for simulating NIRS data [30]. The accuracy can be further improved by using a more realistic geometrical model, e.g. an anatomical head model from MRI data [91].

Sassaroli et al. [92] derived formulas for light propagation to obtain moments directly, eliminating the need to generate DTOFs and thereby reducing computational time. This approach can be particularly advantageous when incorporating changes in moments at multiple source-detector distances, as the computational time for the LMA may grow exponentially with the number of source-detector distances used.

The current implementation of the method based on moments uses only two DTOFs (at baseline and after $\Delta\mu_a$). To further enhance the method, more DTOFs could be incorporated in data analysis. For example, Jelzow et al. [43] fitted a third-order polynomial to the measured changes in moments before using them to determine $\Delta\mu_a$, which can improve the signal-to-noise

ratio. Yang et al. [74,76] proposed a new approach that exploits measurements at multiple source-detector distances, and demonstrated the benefits of incorporating spatial information in addition to time-domain measurements, which improved reliability and reduced uncertainty in determining the absolute optical properties of multiple layers. While the present study used measurements at a single source-detector distance, it is important to note that the proposed method can be extended to use changes in moments at multiple source-detector distances.

We did not use the intensity information (ΔA) for determining $\Delta \mu_a$ because it required careful data processing to account for potential drifts and changes in the output of the laser. Incorporating ΔA information could greatly improve data analysis. We weighted changes in moments by their uncertainty due to photon noise (Poisson statistics) in Eq. (3), to account for the different units and varying levels of uncertainty. A more accurate estimate of the uncertainty could incorporate also the instrumental noise for each moment, which can be measured once for a system [43].

We did not report the uncertainties of the determined optical properties in this study, as it is dependent on several factors including the selected laser power and the acquisition time. The uncertainty of the fitted parameters (for the LMA method) due to photon statistics can be obtained using the method described in [93].

When calculating concentrations of oxy- and deoxyhemoglobin, we used the determined μ_a values at multiple wavelengths, but without accounting for the differences in their uncertainties. The determined μ_a at different wavelengths have varying levels of uncertainty, which relates to the μ_a spectrum of the medium (higher uncertainty for higher μ_a) and to the system used (e.g. if different wavelengths have different power or detection sensitivity). Future studies should aim to incorporate information about uncertainties to improve the determination of hemoglobin concentrations and hence StO_2, e.g. as in [35].

4.2. Measured data and MATLAB codes

The measured TD-NIRS data and the MATLAB codes used in this study were made publicly available [68]. The data is suitable for testing new data analysis methods for tissue oximeters.

The LMA is a search-based algorithm that allows entering the values of known parameters and then determining the unknown parameters. We implemented two LMA algorithms, both of which have the feature of allowing the user to choose which parameters to determine. The first algorithm uses the DTOF as an input and determines any of the eight parameters: μ_a, μ'_s, and/or L (layer's thickness), for up to three layers (the deepest layer is assumed semi-infinite). We used it to determine μ_a and μ'_s assuming a homogeneous medium. The second algorithm uses changes in moments as an input and determines any of the following: $\Delta \mu_a$, $\Delta \mu'_s$, and/or L, for up to three layers. We used it to determine $\Delta \mu_{a,Sup}$ and $\Delta \mu_{a,Deep}$ of a two-layered medium. Future studies may be interested in using this code to determine $\Delta \mu_a$ in two layers (superficial and deep) of a three-layered medium, with the assumption that the μ_a of the middle layer is constant (mimicking the skull). Additionally, the codes can be modified to use DTOFs (in the first algorithm) or changes in moments (in the second algorithm) at multiple source-detector distances.

4.3. Phantom

The phantom allows repeatedly deoxygenating and oxygenating blood in two compartments individually (the results for oxygenating the superficial compartment were not presented), and carrying out simultaneous NIRS measurements on any of the compartments: the two-layered medium (variable superficial layer thickness), the deep (semi-infinite medium), and/or the superficial (semi-infinite medium). The measurements on individual compartments can be analyzed employing a homogeneous model, providing a reference for the optical properties within each compartment, as was done in this study (Fig. 6). The repeatability within and between experiments was demonstrated by carrying out six deoxygenation cycles in three experiments (18 cycles in total). The constructed phantom enables carrying out reproducible experiments,

and has good durability and ease of use. The hemoglobin concentrations and the corresponding StO_2 levels in each compartment followed the expected desaturation trends (StO_2 decreased from 100% to 0%) during all deoxygenation cycles.

The rate of desaturation varied slightly across the three experiments, as seen from the changes in moments in Fig. 7. One potential cause could be a slight difference in the amount of yeast that was added to the phantom. After pouring the mixture containing yeast into the phantom, a small amount of yeast may have adhered to the walls of the beaker, leading to an uncertainty in the amount of yeast added. The temperature of the phantom affects the rate of desaturation, but the temperature was stable as measured with two thermometers.

We found that adding yeast to the solution resulted in an increase in μ'_s (Fig. 10). After the start of the fourth cycle (after 45 min), the μ'_s in the deep compartment began to steadily decrease (visible in Figs. 7 and 10). This decrease had more similar trends in the first and third experiments, in which the same blood bag was used. The decrease in $\mu'_{s,Deep}$ may be related to either the yeast, which was mixing for over 45 minutes, or the blood, which was kept in a desaturated state for an extended period of time (during the third cycle). Ostojic et al. [94] studied the gradual decrease of μ'_s over time in phantoms with blood and proposed possible explanations.

The large size of the phantom requires large amounts of ingredients, which increases the cost of conducting experiments, but more importantly, it makes the phantom easier to control. Due to the large volume, the temperature of the phantom changes at a slow rate, making it easier to maintain it at approximately 37 °C. Additionally, the experiments can be carried out with higher accuracy when handling larger amounts of ingredients, improving the reproducibility of experiments. For example, we added about 3.5 g of Mixture #2 for each step of $\Delta\mu_a$, whereas in another two-layered phantom, the authors needed to add only about 0.7 g to achieve similar $\Delta\mu_a$ [43].

The measurement windows and/or the separating window of the phantom (shown in Fig. 1) could be covered with a layer of material that has tissue-mimicking optical properties for mimicking the skin and/or the skull. This could be achieved using the silicone-based layers presented by Kleiser et al. [63,64] and/or the solid layers presented by Izzetoglu et al. [58], which can be created with variable tissue-mimicking optical properties and thicknesses.

One of the limitations of the study is the absence of an independent reference measurement of StO_2, which limits the assessment of the accuracy of the determined StO_2 values since the true values are unknown. In this study, we compared two measurements of StO_2 (on the deep compartment and on the two-layered medium), both of which were measured by the same system. Kleiser et al. [63,64] showed that different NIRS tissue oximeters can produce different StO_2 values, even when they simultaneously measure on the same phantom. Furthermore, the StO_2 values also depend on the used method of data analysis. The partial pressure of oxygen (pO_2) was proposed as a reference measure in previous studies, but it has major challenges [63,67]. Obtaining reliable reference values of StO_2 would be a significant advancement in the assessment of accuracy, and for calibrating different systems and methods of data analysis.

5. Conclusions

We introduced and experimentally tested a new method for accurately determining even large $\Delta\mu_a$ in multiple layers, which utilizes (i) changes in moments (making use of two DTOFs, at baseline and after $\Delta\mu_a$ in two layers, and the knowledge of the optical properties at baseline), (ii) an analytical solution of the diffusion equation for a multi-layered medium, and (iii) the Levenberg–Marquardt algorithm. We applied the method for tissue oximetry for determining StO_2 in two layers (the absolute μ_a was obtained by summing the baseline μ_a and the determined $\Delta\mu_a$).

We used the established concept of a blood-lipid phantom and constructed a phantom with two such compartments (mimicking superficial and deep layers, with a variable superficial layer

thickness), allowing for the first time, independent control of StO_2 of blood in two compartments. The phantom may be used for performance assessment, such as testing NIRS tissue oximeters or new methods of data analysis, as well as for studying the influence of the superficial compartment on the estimation of StO_2 in the deep compartment.

The results of five experiments, two of which varied the concentration of ink and three of which varied the StO_2 of blood, demonstrated a precise control of the phantom and a high reproducibility of deoxygenation cycles within and between experiments. Also, the accurate determination of μ_a and/or StO_2 in both compartments, using time-domain NIRS data measured on two-layered medium, was confirmed experimentally.

Disclosures. The authors declare no conflicts of interest. MW declares that he is president of the board and founder of OxyPrem AG. AL declares that he is shareholder of Brain Optics.

Data availability. Data and MATLAB codes used in this study were made available under the GNU General Public License v3.0 [68].

References

1. Z. Z. Wong, X. H. Chiong, S. H. Chaw, N. H. B. M. Hashim, M. F. B. Z. Abidin, S. N. B. Yunus, T. Subramaniam, and K. T. Ng, "The Use of Cerebral Oximetry in Surgery: A Systematic Review and Meta-analysis of Randomized Controlled Trials," J. Cardiothorac. Vasc. Anesth. **36**(7), 2002–2011 (2022).
2. F. Sanfilippo, P. Murabito, A. Messina, V. Dezio, D. Busalacchi, G. Ristagno, M. Cecconi, and M. Astuto, "Cerebral regional oxygen saturation during cardiopulmonary resuscitation and return of spontaneous circulation: A systematic review and meta-analysis," Resuscitation **159**, 19–27 (2021).
3. D. Viderman and Y. G. Abdildin, "Near-Infrared Spectroscopy in Neurocritical Care: A Review of Recent Updates," World Neurosurgery **151**, 23–28 (2021).
4. M. Roldán, T. Y. Abay, and P. A. Kyriacou, "Non-Invasive Techniques for Multimodal Monitoring in Traumatic Brain Injury: Systematic Review and Meta-Analysis," Journal of neurotrauma **37**(23), 2445–2453 (2020).
5. W.-L. Chen, J. Wagner, N. Heugel, J. Sugar, Y.-W. Lee, L. Conant, M. Malloy, J. Heffernan, B. Quirk, A. Zinos, S. A. Beardsley, R. Prost, and H. T. Whelan, "Functional Near-Infrared Spectroscopy and Its Clinical Application in the Field of Neuroscience: Advances and Future Directions," Front. Neurosci. **14**, 724 (2020).
6. Y. Chen, Z. Shen, Z. Shao, P. Yu, and J. Wu, "Free Flap Monitoring Using Near-Infrared Spectroscopy: A Systemic Review," Ann. Plast. Surg. **76**(5), 590–597 (2016).
7. H. Sørensen, "Near infrared spectroscopy evaluated cerebral oxygenation during anesthesia," Danish Medical Journal **63**(12), B5318 (2016), PhD Thesis.
8. M. S. Green, S. Sehgal, and R. Tariq, "Near-Infrared Spectroscopy: The New Must Have Tool in the Intensive Care Unit?" Semin Cardiothorac Vasc Anesth **20**(3), 213–224 (2016).
9. R. P. Boezeman, F. L. Moll, Ç. Ünlü, and J. P. de Vries, "Systematic review of clinical applications of monitoring muscle tissue oxygenation with near-infrared spectroscopy in vascular disease," Microvasc. Res. **104**, 11–22 (2016).
10. G. Bale, S. Mitra, and I. Tachtsidis, "Metabolic brain measurements in the newborn: Advances in optical technologies," Physiol. Rep. **8**(17), e1458 (2020).
11. F. Lange, L. Giannoni, and I. Tachtsidis, "The Use of Supercontinuum Laser Sources in Biomedical Diffuse Optics: Unlocking the Power of Multispectral Imaging," Appl. Sci. **11**(10), 4616 (2021).
12. H. Ban, G. Barrett, and A. Borisevich, *et al.*, "Kernel flow: a high channel count scalable time-domain functional near-infrared spectroscopy system," J. Biomed. Opt. **27**, 074710 (2022).
13. K. Harvey-Jones, F. Lange, I. Tachtsidis, N. J. Robertson, and S. Mitra, "Role of optical neuromonitoring in neonatal encephalopathy—current state and recent advances," Front. Pediatr. **9**, 1 (2021).
14. M. Althobaiti and I. Al-Naib, "Recent Developments in Instrumentation of Functional Near-Infrared Spectroscopy Systems," Appl. Sci. **10**(18), 6522 (2020).
15. S. Konugolu Venkata Sekar, P. Lanka, A. Farina, A. Dalla Mora, S. Andersson-Engels, P. Taroni, and A. Pifferi, "Broadband Time Domain Diffuse Optical Reflectance Spectroscopy: A Review of Systems, Methods, and Applications," Appl. Sci. **9**(24), 5465 (2019).
16. F. Lange and I. Tachtsidis, "Clinical Brain Monitoring with Time Domain NIRS: A Review and Future Perspectives," Appl. Sci. **9**(8), 1612 (2019).
17. G. Bale, C. Elwell, and I. Tachtsidis, "From Jöbsis to the present day: a review of clinical near-infrared spectroscopy measurements of cerebral cytochrome-c-oxidase," J. Biomed. Opt. **21**(9), 091307 (2016).
18. I. Tachtsidis and F. Scholkmann, "False positives and false negatives in functional near-infrared spectroscopy: issues, challenges, and the way forward," Neurophotonics **3**(3), 031405 (2016).
19. B. Giles, F. Cristianne, S. Angelo, and F. Sergio, "Dual-slope imaging of cerebral hemodynamics with frequency-domain near-infrared spectroscopy," Neurophotonics **10**(01), 013508 (2023).

20. T. J. Farrell, M. S. Patterson, and M. Essenpreis, "Influence of layered tissue architecture on estimates of tissue optical properties obtained from spatially resolved diffuse reflectometry," Appl. Opt. **37**(10), 1958–1972 (1998).

21. Sophie N. Davie and Hilary P. Grocott, "Impact of Extracranial Contamination on Regional Cerebral Oxygen Saturation: A Comparison of Three Cerebral Oximetry Technologies," Anesthesiology **116**(4), 834–840 (2012).

22. N. Nasseri, S. Kleiser, D. Ostojic, T. Karen, and M. Wolf, "Quantifying the effect of adipose tissue in muscle oximetry by near infrared spectroscopy," Biomed. Opt. Express **7**(11), 4605–4619 (2016).

23. T. B. Fabrizio Martelli, Samuele Del Bianco, André Liemert, and Alwin Kienle, *Light Propagation through Biological Tissue and Other Diffusive Media: Theory, Solutions, and Validations*, Second Edition (SPIE, 2022).

24. M. S. Patterson, B. Chance, and B. C. Wilson, "Time resolved reflectance and transmittance for the noninvasive measurement of tissue optical properties," Appl. Opt. **28**(12), 2331–2336 (1989).

25. R. C. Haskell, L. O. Svaasand, T.-T. Tsay, T.-C. Feng, M. S. McAdams, and B. J. Tromberg, "Boundary conditions for the diffusion equation in radiative transfer," J. Opt. Soc. Am. A **11**(10), 2727–2741 (1994).

26. S. R. Arridge, M. Cope, and D. T. Delpy, "The theoretical basis for the determination of optical pathlengths in tissue: temporal and frequency analysis," Phys. Med. Biol. **37**(7), 1531–1560 (1992).

27. M. Helton, S. Zerafa, K. Vishwanath, and M.-A. Mycek, "Efficient computation of the steady-state and time-domain solutions of the photon diffusion equation in layered turbid media," Sci. Rep. **12**, 18979 (2022). .

28. S. Geiger, D. Reitzle, A. Liemert, and A. Kienle, "Determination of the optical properties of three-layered turbid media in the time domain using the P3 approximation," OSA Continuum **2**(6), 1889–1899 (2019).

29. H. Dehghani, M. E. Eames, P. K. Yalavarthy, S. C. Davis, S. Srinivasan, C. M. Carpenter, B. W. Pogue, and K. D. Paulsen, "Near infrared optical tomography using NIRFAST: Algorithm for numerical model and image reconstruction," Commun Numer Methods Eng **25**, 711–732 (2008).

30. S. Wojtkiewicz and A. Liebert, "Parallel, multi-purpose Monte Carlo code for simulation of light propagation in segmented tissues," Biocybernetics and Biomedical Engineering **41**(4), 1303–1321 (2021).

31. A. Liebert, H. Wabnitz, N. Zolek, and R. Macdonald, "Monte Carlo algorithm for efficient simulation of time-resolved fluorescence in layered turbid media," Opt. Express **16**(17), 13188–13202 (2008).

32. A. Liemert and A. Kienle, "Application of the Laplace transform in time-domain optical spectroscopy and imaging," J. Biomed. Opt. **20**(11), 110502 (2015).

33. M. Fabrizio, B. Samuele Del, S. Lorenzo, C. Stefano, N. Paola Di, B. Tiziano, J. Alexander, M. Rainer, and W. Heidrun, "Optimal estimation reconstruction of the optical properties of a two-layered tissue phantom from time-resolved single-distance measurements," J. Biomed. Opt. **20**(11), 115001 (2015).

34. H. A. García, D. I. Iriarte, J. A. Pomarico, D. Grosenick, and R. Macdonald, "Retrieval of the optical properties of a semiinfinite compartment in a layered scattering medium by single-distance, time-resolved diffuse reflectance measurements," J. Quant. Spectrosc. Radiat. Transfer **189**, 66–74 (2017).

35. H. García, G. Baez, and J. Pomarico, "Simultaneous retrieval of optical and geometrical parameters of multilayered turbid media via state-estimation algorithms," Biomed. Opt. Express **9**(8), 3953–3973 (2018).

36. G. R. Baez, H. García, D. Grosenick, and H. Wabnitz, "Implementation of the extended Kalman filter for determining the optical and geometrical properties of turbid layered media by time-resolved single distance measurements," Biomed. Opt. Express **11**(1), 251–266 (2020).

37. S. Mosca, P. Lanka, N. Stone, S. Konugolu Venkata Sekar, P. Matousek, G. Valentini, and A. Pifferi, "Optical characterisation of porcine tissues from various organs in the 650–1100 nm range using time-domain diffuse spectroscopy," Biomed. Opt. Express **11**(3), 1697–1706 (2020).

38. S. Konugolu Venkata Sekar, A. Farina, A. Dalla Mora, C. Lindner, M. Pagliazzi, M. Mora, G. Aranda, H. Dehghani, T. Durduran, P. Taroni, and A. Pifferi, "Broadband (550–1350 nm) diffuse optical characterization of thyroid chromophores," Sci. Rep. **8**(1), 10015 (2018).

39. B. Hallacoglu, A. Sassaroli, and S. Fantini, "Optical characterization of two-layered turbid media for non-invasive, absolute oximetry in cerebral and extracerebral tissue," PLoS One **8**(5), e64095 (2013).

40. J. Steinbrink, H. Wabnitz, H. Obrig, A. Villringer, and H. Rinneberg, "Determining changes in NIR absorption using a layered model of the human head," Phys. Med. Biol. **46**(3), 879–896 (2001).

41. A. Liebert, H. Wabnitz, J. Steinbrink, H. Obrig, M. Möller, R. Macdonald, A. Villringer, and H. Rinneberg, "Time-Resolved Multidistance Near-Infrared Spectroscopy of the Adult Head: Intracerebral and Extracerebral Absorption Changes from Moments of Distribution of Times of Flight of Photons," Appl. Opt. **43**(15), 3037–3047 (2004).

42. A. Liebert, H. Wabnitz, and C. Elster, "Determination of absorption changes from moments of distributions of times of flight of photons: optimization of measurement conditions for a two-layered tissue model," J. Biomed. Opt. **17**(5), 057005 (2012).

43. A. Jelzow, H. Wabnitz, I. Tachtsidis, E. Kirilina, R. Brühl, and R. Macdonald, "Separation of superficial and cerebral hemodynamics using a single distance time-domain NIRS measurement," Biomed. Opt. Express **5**(5), 1465–1482 (2014).

44. D. Milej, A. Abdalmalak, P. McLachlan, M. Diop, A. Liebert, and K. St Lawrence, "Subtraction-based approach for enhancing the depth sensitivity of time-resolved NIRS," Biomed. Opt. Express **7**(11), 4514–4526 (2016).

45. M. Kacprzak, A. Liebert, W. Staszkiewicz, A. Gabrusiewicz, P. Sawosz, G. Madycki, and R. Maniewski, "Application of a time-resolved optical brain imager for monitoring cerebral oxygenation during carotid surgery," J. Biomed. Opt. **17**(1), 016002 (2012).

46. A. Jelzow, "In vivo quantification of absorption changes in the human brain by time-domain diffuse near-infrared spectroscopy," PhD Thesis (2013).
47. O.-M. Antonio, R. De'Ja, A. Jessica, F. Parya, G. Yuanyuan, Z. Bernhard, A. Y. Meryem, and A. B. David, "How much do time-domain functional near-infrared spectroscopy (fNIRS) moments improve estimation of brain activity over traditional fNIRS?" Neurophotonics **10**(01), 013504 (2022).
48. H. Wabnitz, D. Contini, L. Spinelli, A. Torricelli, and A. Liebert, "Depth-selective analysis in time-domain optical brain imaging: moments vs time windows," Biomed. Opt. Express **11**(8), 4224–4243 (2020).
49. A. Sudakou, H. Wabnitz, L. Yang, D. Contini, L. Spinelli, A. Torricelli, and A. Liebert, *Depth selectivity in time-domain fNIRS by analyzing moments and time windows* (SPIE, 2021).
50. A. Gerega, D. Milej, W. Weigl, M. Kacprzak, and A. Liebert, "Multiwavelength time-resolved near-infrared spectroscopy of the adult head: Assessment of intracerebral and extracerebral absorption changes," Biomed. Opt. Express **9**(7), 2974 (2018).
51. C. Hornberger and H. Wabnitz, "Approaches for calibration and validation of near-infrared optical methods for oxygenation monitoring," Biomed. Tech. **63**(5), 537–546 (2018).
52. P. Lanka, L. Yang, and D. Orive-Miguel, *et al.*, "Multi-laboratory performance assessment of diffuse optics instruments: the BitMap exercise," J. Biomed. Opt. **27**(07), 074716 (2022).
53. H. Wabnitz, D. Taubert, and M. Mazurenka, *et al.*, "Performance assessment of time-domain optical brain imagers, part 1: basic instrumental performance protocol," J. Biomed. Opt. **19**(8), 086010 (2014).
54. H. Wabnitz, A. Jelzow, and M. Mazurenka, *et al.*, "Performance assessment of time-domain optical brain imagers, part 2: nEUROPt protocol," J. Biomed. Opt. **19**(8), 086012 (2014).
55. A. Pifferi, A. Torricelli, A. Bassi, P. Taroni, H. Wabnitz, D. Grosenick, M. Möller, R. Macdonald, J. Swartling, T. Svensson, S. Andersson-Engels, R. Veen, H. Sterenborg, J.-M. Tualle, N. Halien, S. Avrillier, M. Whelan, and H. Stamm, "Performance assessment of photon migration instruments: The MEDPHOT protocol," Appl. Opt. **44**(11), 2104–2114 (2005).
56. M. A. Yücel, A. V. Lühmann, and F. Scholkmann, *et al.*, "Best practices for fNIRS publications," Neurophotonics **8**(01), 012101 (2021).
57. J. Hwang, J. C. Ramella-Roman, and R. Nordstrom, "Introduction: Feature Issue on Phantoms for the Performance Evaluation and Validation of Optical Medical Imaging Devices," Biomed. Opt. Express **3**(6), 1399–1403 (2012).
58. M. Izzetoglu, J. Du, K. Izzetoglu, H. Ayaz, B. Onaral, and B. B. Dor, "Multilayer, dynamic, mixed solid/liquid human head models for the evaluation of near infrared spectroscopy systems," IEEE Trans. Instrum. Meas. **69**(10), 8441–8451 (2020).
59. A. Afshari, P. Ghassemi, J. Lin, M. Halprin, J. Wang, G. Mendoza, S. Weininger, and T. J. Pfefer, "Cerebral oximetry performance testing with a 3D-printed vascular array phantom," Biomed. Opt. Express **10**(8), 3731–3746 (2019).
60. S. K. V. Sekar, A. Pacheco, P. Martella, H. Li, P. Lanka, A. Pifferi, and S. Andersson-Engels, "Solid phantom recipe for diffuse optics in biophotonics applications: a step towards anatomically correct 3D tissue phantoms," Biomed. Opt. Express **10**(4), 2090–2100 (2019).
61. A. Pacheco, H. Li, M. Chakravarty, S. Sekar, and S. Andersson-Engels, "Anthropomorphic optical phantom of the neonatal thorax: a key tool for pulmonary studies in preterm infants," J. Biomed. Opt. **25**, 115001 (2020).
62. G. Liu, K. Huang, Q. Jia, S. Liu, S. Shen, J. Li, E. Dong, P. Lemaillet, D. W. Allen, and R. X. Xu, "Fabrication of a multilayer tissue-mimicking phantom with tunable optical properties to simulate vascular oxygenation and perfusion for optical imaging technology," Appl. Opt. **57**(23), 6772–6780 (2018).
63. S. Kleiser, N. Nasseri, B. Andresen, G. Greisen, and M. Wolf, "Comparison of tissue oximeters on a liquid phantom with adjustable optical properties," Biomed. Opt. Express **7**(8), 2973–2992 (2016).
64. S. Kleiser, D. Ostojic, B. Andresen, N. Nasseri, H. Isler, F. Scholkmann, T. Karen, G. Greisen, and M. Wolf, "Comparison of tissue oximeters on a liquid phantom with adjustable optical properties: an extension," Biomed. Opt. Express **9**(1), 86–101 (2018).
65. F. Lange, L. Dunne, L. Hale, and I. Tachtsidis, "MAESTROS: A Multiwavelength Time-Domain NIRS System to Monitor Changes in Oxygenation and Oxidation State of Cytochrome-C-Oxidase," IEEE J. Sel. Top. Quantum Electron. **25**(1), 1–12 (2019).
66. M. Izzetoglu, K. Pourrezaei, J. Du, and P. A. Shewokis, "Evaluation of cerebral tissue oximeters using multilayered dynamic head models," IEEE Trans. Instrum. Meas. **70**, 1–12 (2021).
67. P. Rejmstad, J. D. Johansson, N. Haj-Hosseini, and K. Wårdell, "A method for monitoring of oxygen saturation changes in brain tissue using diffuse reflectance spectroscopy," J. Biophotonics **10**(3), 446–455 (2017).
68. A. Sudakou, H. Wabnitz, A. Liemert, M. Wolf, and A. Liebert, "TD-NIRS Data and MATLAB Codes used for this study," Github 2023, https://github.com/asudakou/Analyzing_TD-NIRS.
69. A. Gerega, D. Milej, W. Weigl, M. Botwicz, N. Zolek, M. Kacprzak, W. Wierzejski, B. Toczylowska, E. Mayzner-Zawadzka, R. Maniewski, and A. Liebert, "Multiwavelength time-resolved detection of fluorescence during the inflow of indocyanine green into the adult's brain," J. Biomed. Opt. **17**, 087001 (2012).
70. A. Sudakou, F. Lange, H. Isler, P. Lanka, S. Wojtkiewicz, P. Sawosz, D. Ostojic, M. Wolf, A. Pifferi, I. Tachtsidis, A. Liebert, and A. Gerega, "Time-domain NIRS system based on supercontinuum light source and multi-wavelength detection: validation for tissue oxygenation studies," Biomed. Opt. Express **12**(10), 6629–6650 (2021).
71. V. Ntziachristos and B. Chance, "Accuracy limits in the determination of absolute optical properties using time-resolved NIR spectroscopy," Med. Phys. **28**(6), 1115–1124 (2001).

72. A. Liebert, H. Wabnitz, D. Grosenick, and R. Macdonald, "Fiber dispersion in time domain measurements compromising the accuracy of determination of optical properties of strongly scattering media," J. Biomed. Opt. **8**(3), 512 (2003).

73. I. Pirovano, R. Re, A. Candeo, D. Contini, A. Torricelli, and L. Spinelli, "Instrument response function acquisition in reflectance geometry for time-resolved diffuse optical measurements," Biomed. Opt. Express **11**(1), 240–250 (2020).

74. L. Yang, H. Wabnitz, T. Gladytz, R. Macdonald, and D. Grosenick, "Spatially-enhanced time-domain NIRS for accurate determination of tissue optical properties," Opt. Express **27**(19), 26415 (2019).

75. A. Liebert, H. Wabnitz, D. Grosenick, M. Moller, R. Macdonald, and H. Rinneberg, "Evaluation of optical properties of highly scattering media by moments of distributions of times of flight of photons," Appl. Opt. **42**(28), 5785–5792 (2003).

76. L. Yang, H. Wabnitz, T. Gladytz, A. Sudakou, R. Macdonald, and D. Grosenick, "Space-enhanced time-domain diffuse optics for determination of tissue optical properties in two-layered structures," Biomed. Opt. Express **11**(11), 6570–6589 (2020).

77. M. Helton, M.-A. Mycek, and K. Vishwanath, "Reconstruction of optical coefficients in turbid media using time-resolved reflectance and calibration-free instrument response functions," Biomed. Opt. Express **13**(3), 1595–1608 (2022).

78. N. Kollias and W. B. Gratzer, "Tabulated molar extinction coefficient for hemoglobin in water," Wellman Laboratories, Harvard Medical School, Boston **5**, 150–161 (1999).

79. S. J. Matcher, M. Cope, and D. T. Delpy, "Use of the water absorption spectrum to quantify tissue chromophore concentration changes in near-infrared spectroscopy," Phys. Med. Biol. **39**(1), 177–196 (1994).

80. S. D. Bianco, F. Martelli, F. Cignini, G. Zaccanti, A. Pifferi, A. Torricelli, A. Bassi, P. Taroni, and R. Cubeddu, "Liquid phantom for investigating light propagation through layered diffusive media," Opt. Express **12**(10), 2102–2111 (2004).

81. P. D. Ninni, F. Martelli, and G. Zaccanti, "Intralipid: towards a diffusive reference standard for optical tissue phantoms," Phys. Med. Biol. **56**(2), N21–28 (2011).

82. P. D. Ninni, F. Martelli, and G. Zaccanti, "The use of India ink in tissue-simulating phantoms," Opt. Express **18**(26), 26854–26865 (2010).

83. L. Spinelli, F. Martelli, A. Farina, A. Pifferi, A. Torricelli, R. Cubeddu, and G. Zaccanti, "Calibration of scattering and absorption properties of a liquid diffusive medium at NIR wavelengths. Time-resolved method," Opt. Express **15**(11), 6589–6604 (2007).

84. L. Spinelli, M. Botwicz, and N. Zolek, *et al.*, "Determination of reference values for optical properties of liquid phantoms based on Intralipid and India ink," Biomed. Opt. Express **5**(7), 2037–2053 (2014).

85. S. L. Jacques, "Optical properties of biological tissues: a review," Phys. Med. Biol. **58**(11), R37–R61 (2013).

86. L. Tom, A. W. Philip, and H. C. Paul, "Optical properties of human skin," J. Biomed. Opt. **17**(9), 0909011 (2012).

87. A. Farina, A. Torricelli, I. Bargigia, L. Spinelli, R. Cubeddu, F. Foschum, M. Jäger, E. Simon, O. Fugger, A. Kienle, F. Martelli, P. Di Ninni, G. Zaccanti, D. Milej, P. Sawosz, M. Kacprzak, A. Liebert, and A. Pifferi, "In-vivo multilaboratory investigation of the optical properties of the human head," Biomed. Opt. Express **6**(7), 2609–2623 (2015).

88. A. Sudakou, L. Yang, H. Wabnitz, S. Wojtkiewicz, and A. Liebert, "Performance of measurands in time-domain optical brain imaging: depth selectivity versus contrast-to-noise ratio," Biomed. Opt. Express **11**(8), 4348–4365 (2020).

89. J. Selb, T. M. Ogden, J. Dubb, Q. Fang, and D. A. Boas, "Comparison of a layered slab and an atlas head model for Monte Carlo fitting of time-domain near-infrared spectroscopy data of the adult head," J. Biomed. Opt. **19**(1), 016010 (2014).

90. C. Sato, M. Shimada, Y. Tanikawa, and Y. Hoshi, "Estimating the absorption coefficient of the bottom layer in four-layered turbid mediums based on the time-domain depth sensitivity of near-infrared light reflectance," J. Biomed. Opt. **18**(9), 097005 (2013).

91. J. Feng, W. Zhang, Z. Li, K. Jia, S. Jiang, H. Dehghani, B. W. Pogue, and K. D. Paulsen, "Deep-learning based image reconstruction for MRI-guided near-infrared spectral tomography," Optica **9**(3), 264–267 (2022).

92. A. Sassaroli, F. Martelli, and S. Fantini, "Perturbation theory for the diffusion equation by use of the moments of the generalized temporal point-spread function. III. Frequency-domain and time-domain results," J. Opt. Soc. Am. A **27**(7), 1723–1742 (2010).

93. W. H. Press, S. A. Teukolsky, W. T. Vetterling, and B. P. Flannery, *Numerical Recipes 3rd Edition: The Art of Scientific Computing* (Cambridge University Press, 2007).

94. D. Ostojic, S. Kleiser, N. Nasseri, H. Isler, B. Andresen, H. Wabnitz, T. Karen, F. Scholkmann, and M. Wolf, "In vitro comparisons of near-infrared spectroscopy oximeters: impact of slow changes in scattering of liquid phantoms," Adv. Exp. Med. Biol. **1072**, 375–379 (2018).